Rheophysics of Concentrated Particle Suspensions in a Couette Cell using a Refractive Index Matching Technique

THÈSE N^O 4627 (2010)

PRÉSENTÉE LE 19 MARS 2010
À LA FACULTÉ ENVIRONNEMENT NATUREL, ARCHITECTURAL ET CONSTRUIT
LABORATOIRE D'HYDRAULIQUE ENVIRONNEMENTALE
PROGRAMME DOCTORAL EN MÉCANIQUE

ÉCOLE POLYTECHNIQUE FÉDÉRALE DE LAUSANNE

POUR L'OBTENTION DU GRADE DE DOCTEUR ÈS SCIENCES

PAR

Sébastien WIEDERSEINER

acceptée sur proposition du jury:

Dr M. Farhat, président du jury
Prof. C. Ancey, directeur de thèse
Dr P. Fischer, rapporteur
Prof. V. Michaud, rapporteur
Dr B. Pouligny, rapporteur

EPFL
ÉCOLE POLYTECHNIQUE
FÉDÉRALE DE LAUSANNE

Suisse
2010

Résumé

L'objectif principal de ce travail est de contribuer à une meilleure compréhension de la rhéométrie et de la rhéologie des suspensions granulaires non colloïdales hyperconcentrées. Parmi les nombreuses questions encore sans réponses, nous nous sommes tout spécialement intéressés, d'une part, aux problèmes de rhéométrie associés à ce type de fluides et, d'autre part, à leur rhéologie dans les régimes frictionnels et visqueux, ainsi que la transition entre les deux qui reste bien mal comprise.

Pour s'attaquer à ces questions, il a fallu dans un premier temps développer des techniques capables de mesurer de façon non invasive et locale l'écoulement de ces suspensions hyperconcentrées. Une partie de cette thèse est dédiée au développement et à la mise en œuvre de la technique de visualisation optique au cœur de suspensions hyperconcentrées, qui a été développée au Laboratoire d'Hydraulique Environnementale. Cette technique de mesure combine le développement de fluides iso-indice avec l'utilisation de technique de vélocimétrie par image de particules fluorescentes.

Sur cette base, nous avons pu nous attaquer aux véritables questions concernant, d'une part, les mesures rhéométriques de ce type de fluides et, d'autre part, les propriétés rhéologiques elles-mêmes.

Parmi les problèmes abordés, les questions suivantes furent les principales :

Est-il possible d'obtenir un rhéogramme pertinent pour les suspensions de particules concentrées à partir des mesures macroscopiques ? Ceci en tenant compte du large éventail de cisaillement au sein de l'entrefer, l'hétérogénéité du matériau et les problèmes de résolution du problème de Couette en raison du large entrefer ?

Quelles sont les propriétés rhéologiques principales des suspensions granulaires non colloïdales hyperconcentrées dans les régimes frictionnels et visqueux ? Qu'en est-il de la transition entre ces régimes ?

Mots-clés : mécanique des fluides expérimentale, suspensions de particules non colloïdales hyperconcentrées, matériau granulaire, rhéologie, rhéométrie, écoulement de Couette, vélocimétrie par image de particules fluorescentes, fluides iso-indice.

Abstract

The main objective of this work is to gain insight into the rheometry and rheology of concentrated non-colloidal particle suspensions. Among the many questions that have as yet received little answers, we are especially interested in the rheometric problems associated with this type of fluid and in their rheology in the frictional and viscous regimes, as well as the transition between both regimes—a topic that is particularly unclear.

To address these issues, we had initially to develop techniques capable of measuring non-invasively the velocity field within these concentrated suspensions. Part of this thesis is dedicated to the development and implementation of an optical visualization technique inside concentrated suspensions, which was developed at the Laboratory of Environmental Hydraulics. This measurement technique combines the development of iso-index fluids and the use of fluorescent particle image velocimetry.

On this basis, we could then tackle the real issues of this work, that is, on the one hand, rheometric measurement techniques of these fluids and, on the other hand, the rheologic properties.

Among the issues discussed, the following were the main:

Is it possible to obtain a reliable flow curve for concentrated particle suspensions from bulk measurement? And this by considering the wide shear range within the gap, the non-homogeneous material and the inversion-technique problems due to the wide gap?

What are the main rheological properties of concentrated non-colloidal particle suspensions in the frictional and viscous regimes? What about the transition between these two regimes?

Keywords: experimental fluid mechanics, non colloidal particle suspensions, granular matter, rheology, rheometry, Couette flow, fluorescent particle image velocimetry, index-matching fluids.

Remerciements

Je souhaite tout d'abord remercier mon directeur de thèse, Christophe Ancey, de m'avoir tout d'abord guidé dans mes premiers pas en rhéologie et rhéométrie des suspensions granulaires concentrées. Je le remercie aussi pour l'environnement qu'il a forgé petit à petit et dont nous avons pu jouir durant nos thèses. Je le remercie encore de son aide et de son recul sur les choses durant certains « pédalage tête dans le guidon ». Je le remercie pour la liberté, l'autonomie et la confiance qu'il m'a accordées. Je le remercie finalement pour le bon temps que nous avons pu passer ensemble à l'EPFL comme en montagne.

Je remercie ensuite tout les membres passés et présents du Laboratoire d'Hydraulique Environne-mentale. Je remercie tout spécialement mon cher ami et collègue Martin Rentscher. Nos thèses ont commencé presque simultanément ici et elles vont apparemment finir ainsi aussi. Je le remercie pour d'innombrables discussions passionnantes, nos travaux en commun, sa gentillesse, sa générosité, sa fa-mille, ses chaussures de ski et ses lunettes de soleil parfois oubliées et finalement tout spécialement pour son amitié. Je remercie ensuite Damien Bouffard pour les moments passés ensemble, les discussions liées à la mécanique des fluides en général et plus particulièrement celles du lac vues de l'intérieur et celle des bulles... Je remercie Steve Cochard pour son aide, sa rigueur et sa recherche du « swiss quality », ainsi que sa dévotion sans limite à Alinghi. Je remercie Nicolas Andreini sans qui la visualisation au cœur de suspensions concentrées resterait encore opaque comme l'eau du Léman certains jours. Je remercie aussi Gaël Epely Chauvin pour son franc parler, sa bonne humeur, sa motivation jour après jour, toutes ces sympathiques soirées durant la rédaction et finalement pour son « on essaie juste comme ça et on verra bien... ». Je remercie ensuite Claude Perrinjaquet pour son expérience, son aide pour tout ce qui touche à l'expérimental, sa jeunesse d'esprit et finalement ses « secouements » verbaux pour doctorants égarés. Je remercie ensuite Bob de Graffenried d'avoir repris le flambeau de notre instrumentaliste parti pour un repos bien mérité, tâche bien ardue à vrai dire. Un grand merci à Michel Teuscher et son équipe sans qui le moindre boulon aurait été la croix et la bannière. Un grand merci encore à Koen Blanckaert pour toutes ces intéressantes discussions, ces moments partagés à l'EPFL, sur le lac comme à la montagne.

Pour finir mon plus grand merci revient à ma chère et tendre Cécile qui m'a supporté (dans tous les sens du terme) pendant tout ce temps et même plus. Un merci tout particulier mes parents, mes frères Jean-Martin, Patrick et Christian, toute ma famille et mes amis. Un merci tout particulier à Étienne pour nos escapades alpines qui amènent un équilibre vital au travail dans les plaines lausannoises. Un grand merci finalement à tout ceux que j'aurais pu oublier par mégarde.

Contents

List of Figures

List of Tables

Notation

$\boldsymbol{b}$	Body force		n_{ij}	Refractive index of the two components
d	Diameter		P_d	Dissipated energie rate
d_{ij}	Strain rate tensor		p	Weight fraction, $p_i = \frac{\phi_i \rho_i}{\rho_{ij}}$
$\boldsymbol{g}$	Gravity		$\underline{q}$	Fluctuation kinetic energy flux
h	height		r	Radius
I	Intensity of transmitted light		T	Light transmittance
I_0	Intensity of incident light		T	Total torque on the geometry
K	Scattering coefficient		T	Temperature
M	Torque per unit of height		t	Time
m_i	Mass fraction of the ith component		$\boldsymbol{u}, \boldsymbol{v}$	Velocity
N	Normal stress		x	Distance
n	Refractive index			

Greek letter

γ	Strain		μ	Dynamic viscosity
$\dot{\gamma}$	Strain rate		ν	Kinematic viscosity
$\delta(\mathbf{x})$	Dirac function		ρ	Density
ϵ	Particle roughness		ρ'	Buoyant density
η	Dynamic viscosity		ϕ	Volume fraction
η_r	Relative viscosity (η/η_f)		Σ	Stress tensor
κ	Bolzmann constant		τ	Turbidity
λ	Light wavelength		τ	Shear stress

Dimensionless number

Ba	Bagnold number
Co	Coulomb number
Le	Leighton number
Re	Reynolds number
St	Stokes number

Subscript

i	ith component
ij	Mixture of the two components i and j
f	Fluid
p	Particle
s	Solid
l	Liquid
r	Relative

Abbreviation

CW	Continous wave
CCD	Charge-coupled device
DBH	1,6 Dibromohexane
FFT	Fast fourier transform
FPP	Flat parallel plate
FPIV	Fluorescent particle image velocimetry
HB	Herschel-Bulkley
in	Inner
MRI	Magnetic resonance imaging
max	Maximum
min	Minimum
out	Outer
PC	Polycarbonate
PCTFE	Polychlorotrlfluoroethylene
PEEK	Polyetheretherketone
PET	Polyethyleneterephthalate
PIV	Particle image velocimetry
PMMA	Polymethylmethacrylate
PMMA EA	Polymethylmethacrylate ethylacrylate
POM	Polyformaldehyde
PS	Polystyrene
PTFE	Polytetrafluoroethylene
PTV	Particle tracking velocimetry
PVA	Polyvinylacetate
PVC	Polyvinylchloride
RI	Refractive index
SAN	Styrene/acrylonitrile copolymer
SNR	Signal-to-noise ratio
TFE	Tetrafluoroethylene
tot	Total
TRPIV	Time-resolved PIV
Trimix	Ternary fluid mixture

Introduction

A large number of gravity-driven geophysical flows involve suspensions of particles in a fluid. Typical examples include snow avalanches, debris flows, turbidity currents, pyroclastic flows, etc. A long-standing practice is to consider these suspensions as one-phase or two-phase continua on the bulk scale, which makes it possible to use a fluid-mechanics treatment to compute the motion features (velocity, flow-depth, spreading, etc.). Usually the computations are made by using depth-averaged equations of motion. These equations rely on a number of assumptions such as the long-wave approximation (that involves assuming that flow-depth scales are far smaller than length scales, which leads to simplifying a great deal the resulting equations). Primarily developed for water floods (shallow-water equations), depth-averaged equations of motion provide results in good agreement with experimental and field measurements for various flow conditions (gradually varied flow or transient flows like in the dam-break problem) involving Newtonian or inviscid fluids.

Materials involved in geophysical flows exhibit non-Newtonian rheological properties and, over the last few years, a great deal of work has been expended to adapt the shallow-water equations to non-Newtonian fluids. Comparison between theoretical and experimental results has revealed a few shortcomings in this approach, but it is still unclear whether they result from an improper account for nonlinear rheological behavior and/or breakdown of basic assumptions such as the long-wave approximation. Given the growing role played by numerical simulations based on depth-averaged equations in engineering applications, it is of great interest to take a closer look at this issue.

The objective of this work is to gain insight into the rheological behavior of concentrated non-colloidal particle suspensions. This objective can be subdivided into three tasks. The first one aims at developing measurement techniques, which provide reliable velocity profiles inside a concentrated particle suspension. Task 2 addresses the question of how to make meaningful rheologic measurements in concentrated particle suspensions. Task 3 tackles the delicate issue of the rheologic interpretation of experimental data, i.e. how to derive the flow curve from viscometric data. There are many impediments to this derivation:

1. Because of the particle size, which is of the order of the gap for classic rheometers, wide-gap geometries have to be used and most of the common geometries (i.e. cone and plate, parallel plates) cannot be used for different reasons. We therefore focused our experiments on wide-gap Couette geometries. Wide-gap cells involve solving the Couette inversion problem properly. To date, there is no consensus about the best inversion technique. To try to answer, at least partially, that question, performing simultaneously local and bulk flow measurements allow for comparisons with two different inferring methods:

   - a direct derivation of the flow curve by differentiation of the velocity profiles, hereafter referred to as the *rheophysical approach*;

- a classic rheometric treatment, which consists in inferring the $\dot{\gamma} - \tau$ flow curve from the raw angular velocity and torque measurements (Ω_i, T_i) using a given inversion technique.

A schematic view is given by table 1.1.

Table 1.1: Classic rheometry vs rheophysical approach

Continuum mechanics approach	Rheophysical approach
⇓	⇓
Classical rheometry	Velocity profile measurement
⇓	
Angular velocity and torque (Ω_i, T_i)	⇓
⇓	
Solving the Couette inverse problem	Direct differentiation of the velocity profile
⇓	⇓
$(\tau, \dot{\gamma})$ flow curve	$(\tau, \dot{\gamma})$ flow curve

2. Looking carefully at the rheology of non-colloidal particle suspensions, we are facing many open questions. Several of their features are still poorly understood. As we will see in § 2, concentrated non-colloidal particle suspensions undergo different flow regimes, which depend on the prevailing type of contact between the particles. These flow regimes give rise to different flow behaviors, for which the transition from one to the other remains only partially understood. The present work will focus on the frictional and viscous regimes and the transition.

This manuscript will begin by presenting a review of the current knowledge on the rheology and rheometry of non-colloidal particle suspensions since the beginning of the 20th century (§ 2). In § 3, we will present the experimental techniques used to infer the rheological properties of concentrated particle suspensions using classic rheometry techniques (§ 3.1 to § 3.2) and local measurements techniques, which rely on refractive-index-matching techniques and PIV techniques (§ 3.3 to § 3.5). Our experimental facility and the experimental procedure will be described in § 4. Experimental results concerning the vane geometry and the associated wall slip effects will be presented and discussed in § 5. Transient and steady-state measurements will provide insight into the induced particle diffusion process. Bulk and locally inferred flow curves will be also outlined and compared.

2 Literature Review

The rheological behavior of particle suspensions is a longstanding problem in fluid mechanics, which has attracted considerable attention since the seminal work of Einstein in 1906 on viscosity of dilute suspensions [95, 96]. A large body of work has been done in this field, with substantial theoretical, numerical, and experimental developments. A short and recent summary of the state of art can be found in Mewis and Wagner, 2009 [198], but given the wide spectrum of topics covered by the rheology of suspensions, there is no complete review of this growing field. Here I will set the scene by giving a brief overview of the various problems encountered in studying concentrated suspensions of non-colloidal particles. I will refer the reader to authoritative papers covering this domain for further information.

This chapter starts with a classification of dilute, semi-dilute and concentrated suspensions based dimensional analysis (§ 2.1). I will briefly outlined the theoretical work on non-colloidal particle suspension rheology (§ 2.2). I will take a closer look at experiments conducted on coarse-particle suspensions (§ 2.3), with emphasis given to bulk viscosity. In (§ 2.4), I will review much of the early work done on the Couette cell in the study of concentrated suspensions.

2.1 Classification of particle suspensions: dimensional analysis

2.1.1 Dilute and semi-dilute suspensions

Particle suspensions are considered complex fluids because their rheological behavior exhibit an incredible wealth of properties depending on particle size, concentration, density, etc. In this respect, dimensional analysis is an efficient tool to get a better physical picture by delineating various flow regimes. The presentation here closely follows that of Krieger [161, 164], Jomha *et al.* [143], and Ancey and his coworkers [14, 16, 72].

The key idea is that although the material involves two phases on the particle scale, it behaves as a continuum on the bulk scale, which makes it possible to describe its rheological properties through a constitutive equation. On most occasions, we are interested not in the entire constitutive equation, but in the bulk viscosity η, which is the ratio of the shear stress to the shear rate. We assume that the bulk viscosity of the suspension can be expressed as a function of many variables

$$\eta = f(r, \rho_p, n, \eta_f, \rho_f, kT, \dot{\gamma}, t)$$

which account for

- particles characteristics: particle radius r, density ρ_p, and number density n (number of particles per unit volume);

- suspending medium properties: viscosity η_f and density ρ_f;

• flow parameters: temperature T (or thermal energy kT), shear rate $\dot{\gamma}$, and time t.

All terms in the previous equation can be expressed in units of mass, length, and time. By forming dimensionless groups we can cast this equation into a dimensionless form

$$\eta_r = f(\phi, \Delta\rho, Pe_p, Re_p, t_r) \tag{2.1}$$

where

$$\eta_r = \frac{\eta}{\eta_f} \qquad\qquad\qquad \phi = \frac{4}{3}\pi n r^3$$

$$\Delta\rho = \frac{\rho_p}{\rho_f} \qquad\qquad\qquad Pe_p = \frac{6\pi\eta_f r^3 \dot{\gamma}}{kT}$$

$$Re_p = \frac{\rho_f r^2 \dot{\gamma}}{\eta_f} \qquad\qquad\qquad t_r = \frac{tkT}{\eta_f r^3}$$

When particle and fluid densities are different ($\Delta\rho \neq 1$), sedimentation occurs as a result of gravity, which may lead to phase separation. In this case, the material behaves like a two-phase material on the bulk scale rather a single-phase continuum and Equation (2.1) makes no longer sense.

An interesting end-member of the family of rheological behaviors represented by Eq. (2.1) is constituted by neutrally buoyant systems, i.e. taking the limit of $Pe_p \to \infty$ and $Re_p \to 0$ [55, 248, 267]. In other words, we consider the class of fluid for which Brownian motion, physical interactions (attractive and repulsive forces such as van der Waals forces) as well as particle inertia are negligible contributions to the bulk stress tensor. Since there is no density mismatch between the continuous and disperse phases ($\Delta\rho = 1$), the bulk-viscosity function reduces to:

$$\eta_r = f(\phi) \tag{2.2}$$

This implies that the viscosity is a one-to-one function of concentration and hence the suspensions could be Newtonian (the true story is more complicated since non-Newtonian effects may arise as a result of particle arrangement, normal-stress effects, etc., as shown later in this chapter).

2.1.2 Concentrated suspensions

As shown in § 2.1, the particle volume fraction ϕ remains the key parameter that controls the effective viscosity of buoyant-coarse-particle suspensions. The simplicity of this relation has made it possible to fit many empirical curves on experimental data (see Table 2.2), but it is somewhat misleading in that it reflects many different physical processes that cannot be merely encoded through a scalar relation. Among the many issues, hidden or obvious, that arise in the study of particle suspension, there are two major difficulties:

• **Asymptotic behavior of the viscosity in the high-concentration limit**: experiments have shown that viscosity increases relatively slowly with particle volume fraction as long as the suspension is dilute to moderately concentrated. In contrast, when approaching the maximum volume fraction ϕ_{max}, the viscosity function tends to infinity, which an asymptotic behavior often described by an exponential or power-law function (see Table 2.2). Physically, this limit is no possible. In fact, the system *jams* when $\phi \to \phi_{max}$ (see figure 2.1).

- **Definition of the maximum particle volume fraction**: ϕ_{max} is often defined as the fluidity limit of a suspension of solid particles. It is the volume fraction of the solid below which the suspension behaves like a liquid in that an applied shear stress induces velocity gradients in the mixture. Above the fluidity limit the suspension can support a finite shear stress and hence exhibits the properties of a solid. How ϕ_{max} is precisely defined from both theoretical and experimental standpoints is fundamental to computing bulk-viscosity dependence on ϕ. Indeed, in the dilute and semi-dilute regime, a small change in the particle volume fraction has almost no influence on the apparent viscosity, which is almost independent of the maximum particle volume fraction ϕ_{max}. In contrast, for highly concentrated suspensions, whose viscosity function diverges for $\phi \rightarrow \phi_{max}$, a small change in the value of the maximum particle volume fraction has a strong impact on bulk viscosity. Unfortunately, there is no consensus on how to define the maximum particle volume fraction ϕ_{max} [291, 251] and several expressions can be found in the literature. They physically depend on several parameters such as particle shape, size distribution [54, 81, 103, 321] or particle arrangement (due to the flow or not). Even for a monodisperse suspension, there is no consensus on the maximum random particle volume fraction value [291]. Values usually range from about 0.60 to 0.68. In the case of a face-centered cubic lattice of a monodisperse suspension, the value can be as high as 0.74.

Particle arrangement, shape, size, and size distribution has a strong effect on the rheology of particle suspension, especially at high particle volume fraction.
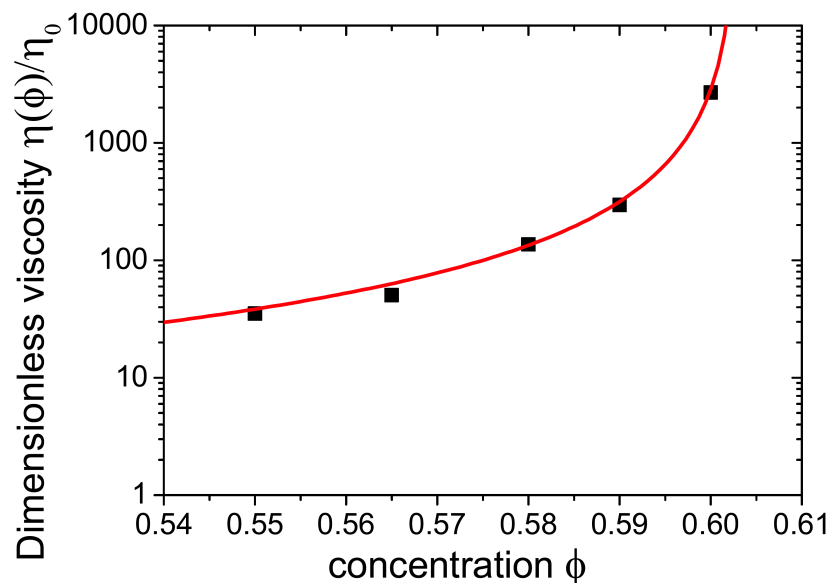
Figure 2.1: Relative viscosity increase with particle volume fraction near the maximum volume fraction. (after [229])

Another critical value of the particle concentration plays a significant role: this is the concentration ϕ_c above which particles start interacting through contacts (here *contact* is taken in a loose meaning, it merely describes the cases where two neighboring particles are so close that they can physically touch). According to Coussot and Ancey [72], as long as the solid concentration is low to moderate, particle contacts (direct or lubricated contact) are almost impossible because of strong repulsive forces in the squeezing flow between two approaching particles. External action is necessary to overcome these forces

and result in particle contact. For particle volume fractions in excess of a critical volume fraction ϕ_c, the particle are so closely packed that they undergo lubricated contacts, which may degenerate into frictional or collisional contacts when the contact forces exceed the resisting viscous forces. Ancey [16] and Coussot and Ancey [14, 72] suggested using dimensionless numbers to determine the prevailing type of contact. They considered that contacts can be classified into three main categories: frictional, lubricated, and collisional contacts. They introduced the following dimensionless numbers:

- Leighton number Le (lubricational vs frictional effects). The number is defined as the ratio of lubrication forces to normal forces:

$$Le = \frac{\eta_f \dot{\gamma} b}{N \epsilon}$$

where η_f is the fluid viscosity, $\dot{\gamma}$ the shear rate, b a characteristic mean distance between the center of mass of two neighboring particles, N the normal stress and ϵ the particle roughness;

- Coulomb number Co (collisional vs frictional effects). The number is defined as the ratio of particle inertia to normal forces:

$$Co = \frac{\rho_p r^2 \dot{\gamma}^2}{N}$$

where ρ_p is the particle density, r the particle radius, $\dot{\gamma}$ the shear rate and N the normal stress. Note that this number is also called the Savage number or the inertial number

- Bagnold number Ba (collisional vs lubricational effects). The number is defined as the ratio of particle inertia to lubrication forces:

$$Ba = \frac{\rho_p \dot{\gamma} r \epsilon}{\eta_f}$$

where ρ_p is the particle density, $\dot{\gamma}$ the shear rate, r the particle radius, ϵ the particle roughness and η_f is the fluid viscosity.

2.2   Theoretical outline

Paralleling the different approaches to defining the bulk stress tensor in continuum mechanics, the methods used in rheology to compute the bulk viscosity can be categorized into two approaches

- **Energy-based approach**: the stress tensor is inferred from the dissipated energy rate P_d and the strain-rate tensor d_{ij} [95, 96]

$$\tau_{ij} = \frac{\partial P_d}{\partial d_{ij}},$$

which gives in the case of simple shear flow: $\tau = P_d / \dot{\gamma}$.

- **Kinetic theory approach**: the suspension stress tensor is inferred from ensemble averages of local stress tensors [28, 75, 175, 176, 249, 318, 319]

$$\tau = < \tau_l >$$

where $< \cdot >$ denotes ensemble average.
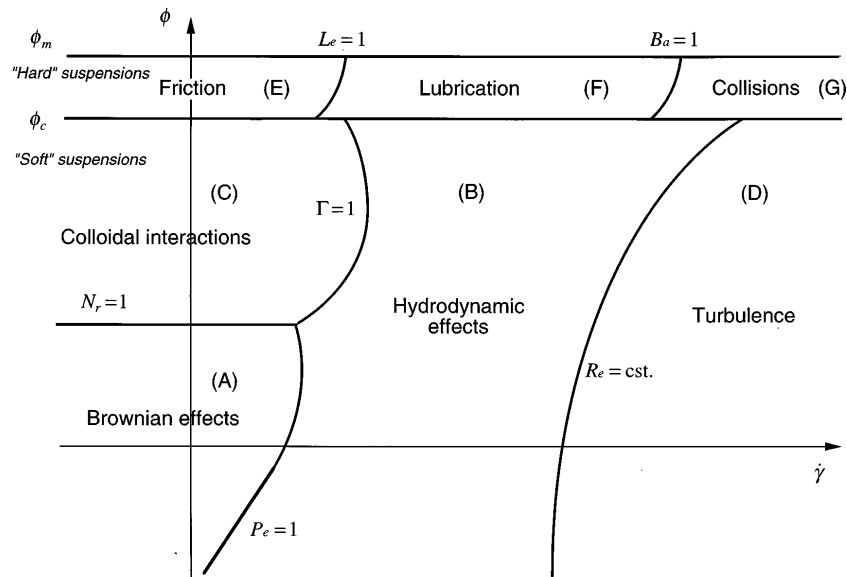
Figure 2.2: Conceptual classification of flow regimes of particle suspensions as function of shear rate $\dot{\gamma}$ and solid fraction. (after [72])

A homogeneous and monodisperse suspension of non-colloidal spherical particles in a Newtonian liquid has a viscosity that varies with the bulk particle concentration. The viscosity increases with particle concentration has been attributed to high dissipation rates in the squeezing flow in the narrow gaps between approaching particles [104]. Marrucci [188] proposed for the viscosity increase with concentration, large-scale coordination motion instead.

Ever since the work of Einstein in 1906 [95, 96] on very dilute suspensions (rigid uniform sphere moving without slip in a medium of equal density at concentration below $\phi = 0.01$, people have related the viscosity of a suspension to the viscosity of the suspending fluid and the particle concentration. For dilute and semi-dilute suspensions of spheres, all models and measurements have assumed that the viscosity of suspensions is independent of shear rate and increases with particle content.

In addition to theoretical derivations of the bulk stress tensor, there have been many attempts to compute bulk viscosity on the basis of heuristical arguments and experimental observations. One of the ideas pursued so far has been to expand the bulk viscosity into a power series of ϕ [97, 98, 99, 112, 113, 114, 157, 274]. The first-order contribution is given by Einstein's expression, which holds for very dilute suspensions. The Einstein equation has been extended by several authors by adding a second-order term with coefficient values ranging from 2.5 to 14.1.

$$\eta_r = 1 + k_1 \cdot \phi + k_2 \cdot \phi^2 \text{ with } k_1 = \frac{5}{2} \text{ and } 2.5 < k_2 < 14.1$$

Experiments provided evidence that this equation is valid for concentrations as high as $0.15 - 0.20$ [29, 30, 32, 93, 94, 301]. The expansion also received theoretical support. Taking into account first-order effects between particles, Batchelor [29] calculated the second order coefficient being 7.6 for a pure strain flow and 5.2 for shear flow.

For higher concentrations, several empirical equations have been proposed. Table 2.2 summarizes the main equations available to date. Instead of reviewing all equations and approaches, I just give some indications on how these equations were obtained. Using shear-rate and particle-size effect considera-

tions, Thomas successfully collapsed viscosity data on a single mastercurve [287]. Batchelor [29, 32] developed the first theoretical treatment of suspension rheology beyond the dilute regime. He used explicitly a pair distribution function to take into account particle microstructure. In addition, in one of his review papers [31], Batchelor concluded that it is almost hopeless to try to find a single constitutive relation between mean stress and mean rate of strain, which is accurate to order $O(\phi^2)$ and which applies to all flow fields. He stated that one should add one (or more) parameter to take into account the microstructure generated by the flow. Brady and Morris [37] showed that in the $Pe_p \rightarrow \infty$ limit surface roughness or non-hydrodynamic effects result in an asymmetric pair distribution function and therefore in non-Newtonian normal stresses. Phan-Thien [240, 241, 242] proposed a model by considering suspensions composed of doublets of particles. More recently Zarraga [316] proposed a new equation that describes the increase in viscosity with particle concentration.

Particle migration has also attracted special attention. Using the approach initially taken by Leighton and Acrivos [170], Phillips *et al.* [243] developed a model that includes a particle flux term proportional to the shear gradient. This model assumes suspensions to be collections of discrete particles moving in an incompressible fluid; it does not say anything about particles' interactions with the interstitial fluid since in the highly concentrated regime, the only significant interactions in the material are assumed to be binary particle interactions. Leighton and Acrivos proposed a mechanism for particle migration in a shear flow, representing migration as a balance between competing particle fluxes that arise in response to gradients in macroscopic quantities in the flow system (gradients in inter-particle collision frequency, gradients in viscosity). As a result, gradients in particle concentration and shear rate drive particle diffusion, often in opposite directions, so that a steady state is reached when the collisional and viscosity driven fluxes balance. This model provides satisfactory results for Couette and Poiseuille flow, but is inadequate for other viscometric flows, specifically the parallel-plate and cone-and-plate geometries. Another approach was proposed by Nott and Brady [222]. In their model the particle flux arises directly from the particle stress. They incorporated the granular temperature and energy fluctuation of McTigue and Jenkins [140, 193] into a two-phase model. Comparison was made with the measurement of Lyon and Leal [181, 182]. The Morris and Brady model [37, 209, 210] is identical to the Nott and Brady model, but with different particle volume fractions as coefficients in the equations. Buyevich [49] proposed a very similar model to the temperature models. A new and unique feature of Buyevich's model is that it allows the suspension temperature to be an anisotropic tensor. Finally, Mills and Snabre [202] presented a model based on lubrication forces between colliding particles and Morris and Boulay [208] proposed a normal stresses shear-induced model. All these models are summarized on table 2.1.

Table 2.1: Shear induced particle diffusion model

Model	Reference	Equations	Notes
Diffusive flux model	- Leighton and Acrivos [170] - Phillips et al. [243]	$\nabla \cdot \boldsymbol{u} = 0$ $\boldsymbol{0} = -\nabla p + \nabla \cdot \boldsymbol{\tau}$ $\boldsymbol{\tau} = \eta_f \eta_r(\phi)\dot{\boldsymbol{\gamma}}$ $\eta_r = (1 - \phi/\phi_{max})^{-1.82}$ $\frac{D\phi}{Dt} = r^2 K_c \nabla \cdot (\phi^2 \nabla\dot{\gamma} + \phi\dot{\gamma}\nabla\phi)$ $\qquad + r^2 K_\eta \nabla \cdot (\dot{\gamma}\eta^2\frac{1}{\eta}\frac{d\eta}{d\phi}\nabla\phi)$ $N_\eta = -K_\eta\dot{\gamma}\phi^2\frac{r^2}{\eta}\nabla\eta$ $N_c = -K_c r^2\phi\nabla(\phi\dot{\gamma})$	Conservation of mass Inertial terms are neglected $\eta_f\eta_r(\phi)$ is the empirical fonction obtained by Krieger [164] (refer to table 2.2) K_c and K_η are phenomenological constants Particle flux due to viscosity gradients Particle flux due to inter-particle collision frequency gradients
Suspension temperature model	- McTigue and Jenkins [140, 193] - Nott and Brady [222] - Morris and Brady [37, 209, 210] - Buyevich [49]	$\frac{\partial\phi}{\partial t} + \nabla \cdot (\phi\boldsymbol{u}) = \boldsymbol{0}$ $\rho_p\phi\frac{D\boldsymbol{u}_p}{Dt} = \boldsymbol{b}_p + \boldsymbol{F}_p + \nabla \cdot \boldsymbol{\Sigma}_p$ $c(\phi)\frac{D<1/2(\rho\boldsymbol{u}^2)'>}{Dt} = \beta(\phi) < \boldsymbol{b}' \cdot \boldsymbol{u}' >$ $\qquad + \boldsymbol{\Sigma}_p : \dot{\boldsymbol{\gamma}} - \eta\alpha(\phi)r^{-2}\boldsymbol{T} - \nabla \cdot \boldsymbol{q}$ $\nabla \cdot \boldsymbol{u} = 0$ $\frac{D(\rho\boldsymbol{u})}{Dt} = \boldsymbol{b} + \nabla \cdot \boldsymbol{\Sigma}$ $\alpha(\phi), \beta(\phi)$ and $c(\phi)$	Conservation of mass for the particle phase Conservation of momentum for the particle phase Conservation of fluctuation kinetic energy Conservation of mass of the fluid phase Conservation of momentum for the fluid phase Functions of particle volume fraction

Table 2.2: Shear induced particle diffusion model

Model	Reference	Equations	Notes
Lubrication forces based model	- Mills and Snabre [202]	$\boldsymbol{u} = \phi\boldsymbol{u}_p + (1-\phi)\boldsymbol{u}_f$ $\nabla \cdot \boldsymbol{u} = 0$ $0 = -\nabla p + \nabla \cdot \boldsymbol{\tau}$ $0 = -\phi\nabla p + \nabla \cdot \boldsymbol{\sigma}_p - \phi\eta_f\eta^* \frac{\boldsymbol{u}_p - \boldsymbol{u}}{r^2}$ $\boldsymbol{\sigma}_p \approx \boldsymbol{\tau}\left(\frac{\eta}{\eta_f}\right)^{1/2} \frac{\phi}{(1-\phi)^{1/2}}$ $\frac{\partial \phi}{\partial t} + \nabla \cdot \left(-\frac{r^2}{\eta_f\eta^*}\frac{\partial}{\partial y}\left[\frac{\phi\eta_r^{1/2}\tau}{(1-\phi)^{1/2}}\right]\right) = 0$	Conservation of mass Conservation of momentum for the fluid phase Conservation of momentum for the particle phase Particle mean stress tensor
Normal stress shear -induced model	- Morris and Boulay [208]	$\frac{\partial \phi}{\partial t} + \nabla \cdot (\phi\boldsymbol{u}) = 0$ $\rho_p\phi\frac{D\boldsymbol{u}_p}{Dt} = \boldsymbol{b}_p + \boldsymbol{F}_p + \nabla \cdot \boldsymbol{\Sigma}_p$ $\frac{\partial \phi}{\partial t} + <\boldsymbol{u}> \nabla \phi = -\frac{2r^2}{9\eta_f}\nabla \cdot [f(\phi\nabla \cdot \Sigma_p)]$ $\Sigma_p = -\eta_f\dot{\gamma}\eta_n\hat{\boldsymbol{Q}}(\phi) + 2\eta_f\eta_r(\phi)\boldsymbol{E}$	Conservation of mass for the particle phase Conservation of momentum for the particle phase $\hat{\boldsymbol{Q}}(\phi)$ is a material property tensor $\boldsymbol{E}$ is the local bulk suspension rate of strain η_n is the "normal stress viscosity"

2.3 Experimental observation

2.3.1 Phenomenological law for the relative viscosity of concentrated particle suspension

A large body of experimental work has been devoted to the dependence of bulk viscosity on particle fraction. Experimental data served to fit new empirical models or test existing equations. Table 2.2 summarizes empirical relations together with experimental investigations. Good agreement is usually found between data and models for dilute to moderately concentrated suspensions. At higher concentration the differences between experiments, empirically and theoretically derived viscosity functions increase substantially. Non-Newtonian behavior has been reported for solid concentration above 0.4: concentrated suspensions are generally shear-thinning and shear-thickening occurs at high shear rate [143]. Beyond the shear-thickening region, the rheological behavior is still unclear. In the zero shear rate limit, the suspension are often Newtonian except for very concentrated suspensions where yield stress behavior has been reported (see below).

2.3.2 Non-Newtonian effects

As already mentioned in § 2.1, whereas for dilute and moderately concentrated particle suspensions, the Newtonian viscosity law is a correct approximation to the rheological behavior, it is no longer valid at high concentrations as a result of several effects: Normal stresses, particle migration and jamming events have been reported.

Normal stress

Bagnold [23] observed that normal stresses scaled linearly with shear rate in steady-shear flows of suspensions, but most of his measurements were in the collisional regime. In addition, the experimental setup used by Bagnold was unlikely to be adapted to this kind of measurements [133]. Gadala-Maria [106] found that the normal stress difference $N_1 - N_2$ was positive and scaled linearly with shear rate in steady shear flow. Prasad and Kytoma [246] also measured the axial normal stress in a parallel-plate device. However they equilibrated fluid pressure with quiescent fluid through a perforated plate, thereby they measured only the stress arising from particle contacts. Bagnold [23], Leighton [171] and Phan-Thien [240] attributed the normal stresses to anisotropic local microstructure, i.e. to the spatial arrangement of the particles. More recently Zarraga *et al.* [316] performed normal stress experiments on highly concentrated suspensions using three different techniques. They showed that both N_1 and N_2 are negative and proportional to the shear stress and with $|N_2| > |N_1|$. The most recent work by Singh and Nott [276] based on Couette and parallel-plate geometries with constant shear and superimposed sinusoidally varied shear rate. They also obtained a linearly varying normal stress with shear rate in the particle volume fraction ranging from 0.3 to 0.45. Their result agrees with Zarraga's experiments.

Shear induced particle diffusion

Leighton and Acrivos [170] performed experiments that provided evidence of a diffusion-like process in which particles migrate from regions of high shear rate to regions of low shear rate, even with a system of non-Brownian and non-inertial suspensions. This migration process results in a non-homogeneous particle concentration. In rotational rheometry, migration can be observed by taking a well-stirred sample and shearing it continuously. The torque decreases continuously with time. Because of the absence of Brownian motion, the time of rest has no effect on migration. Even after a long rest, the suspension retains the same apparent viscosity as it had at the time of flow cessation. This phenomenon is

observed in coaxial cylinder [106, 170], cone-and-plate [250, 281] and parallel-plate geometries. No transient behavior is apparent at low concentration. Particle migration becomes difficult to measure at very high concentrations because the inner cylinder cuts a hole in the suspension and looses contact with the material.

A few constitutive equations, which include particle migration, have been tested against experimental data. First comparisons with the NMR measurement have been carried out by Phillips *et al.* [243] using Abbott and Graham's data [4]. A comprehensive description and comparison with LDV (Laser doppler velocimetry) measurement has been carried out by Shapley [268] and Shapley *et al.* (2002, 2004) [269, 270] with the five previous models (Nott and Brady, Morris and Brady, Buyevich, Phillips, McTigue and Jenkins). Recently, Lenoble *et al.* [172] also did some comparisons with optical measurements.

Yield stress and jamming

For some fluids, the flow curve when plotted in the $\dot{\gamma} - \tau$ plane exhibits a *yield stress*: when the rate is decreased towards zero, the shear stress tends towards a constant value. For colloidal systems, a simple phenomenological model can explain this behavior: competition between re-structuration (aggregation of colloids, which is mainly dependent on the material) and de-structuration (resulting from flow, i.e., mainly dependent on the instantaneous shear rate) leads to a continuously increasing viscosity for low applied stresses. If restructuration overwhelms destruction caused by the flow, the system eventually jams and stops flowing. For granular systems, another explanation has been proposed: change in the spatial arrangement of particles induce viscosity variations. Liu and Nagel [177] stated that glassy, pasty, or granular materials show similar mechanical behavior in that these materials are jammed at rest, but start flowing when the load to which they are submitted increases beyond a critical value.

At very low shear rates, highly concentrated suspensions exhibit a yield stress [74, 78, 139, 253, 229]. The apparent macroscopic stress plateau in the frictional regime [15] was shown (using MRI techniques) to result from shear localization near the inner cylinder [229]. This is in agreement with the viscosity bifurcation experiments of Huang *et al.*, Da Cruz *et al.* and Jarny *et al.* [78, 132, 139]. These experiments provided evidence of the existence of a critical shear rate below which no steady flow is possible. Localization maintains the true shear rate above that critical value. We should not confuse this shear localization with the one that arises when increasing the local particle concentration near the close-packing limit. As already discussed in section 2.1.2, this jamming phenomenon is related to the viscosity divergence when $\phi \to \phi_{max}$. At the microscale, the velocity profiles seem to be self-similar; in particular, a mastercurve on which all velocity collapse can be obtained using the inner cylinder velocity and the sheared layer thickness [229].

Other effects

- Shape
  As shown by Tsai *et al.* [293] and Kitano [152], quasi-monodisperse irregularly shaped sand particles exhibited significantly greater relative viscosity and substantially smaller maximum packing fraction compared to spherical glass beads despite a broader size distribution of the irregularly shaped sand.

- Size
  The effect of particle size on the relative viscosity appears to be controlled by diffusion and it and correlates almost linearly with the particle Péclet number Pe_p [295].

- Size distribution
  For dense packings for polydisperse suspensions, the maximum concentration is shifted to higher values (compared to monodisperse systems),which means that the relative viscosity at a given value of ϕ is lower for a polydisperse system than for a monodisperse suspension. Therefore for polydisperse systems lower relative viscosities are found generally [259]. The size ratio and the type of distribution is of importance [102]. Rheological experiments with bimodal, multimodal, and polydisperse systems emphasize the relation between ϕ_{max} and suspension viscosity.

- Liquid polarity
  For a moderate shear-rate range, Tsai [294] showed that for concentrated suspensions (ϕ up to 0.58), liquid polarity has a significant effect on the pseudoplastic behavior of the suspension in presence of strong interparticular van der Waals forces. Pseudoplasticity increases as liquid polarity decreases. At high shear rate, the hydrodynamic force dominates over such interparticular force and the suspensions become Newtonian.

- Particle ordering
  Depending on the particle size distribution and the shear rate, particles can rearrange in various ways, therefore influencing the suspension rheology. Light scattering experiments [129, 250] have shown that at low shear rate, particles are ordered, but beyond a critical shear rate, particle arrangement is destroyed. Another related effect is the liquefaction observed for non-buoyant-particle suspensions: at higher shear rates, the suspension becomes viscous (not Newtonian because of the presence of normal stress differences apparently due to an anisotropic particle microstructure [171]). Visual observation by Abbott *et al.* [4] and Völtz *et al.* [303] showed particle ordering in two-dimensional hexagonal structures at the outer wall. At higher shear rate, the suspension exhibits shear thickening (for a review, see Barnes [26] or Stickel [280]). This behavior probably stems from a transition from the viscous regime to a collisional regime where dissipation due to grain-grain collisions replaces the interstitial fluid viscous dissipation. Furthermore the ordered structure in the viscous regime disappears and gives way to a random three-dimensional distribution [130, 250].

2.4 Rheophysics of concentrated particle suspensions in a wide-gap Couette cell

Despite many attempts using classical rheometry to get a better insight into the rheology of noncolloidal concentrated particle suspension, many questions have as yet received little answers. As we will see in more details in chapter 3, experimental studies of these materials are faced with measurement problems which make the results tough to process, interpret, and to understand. All usual difficulties encountered in rheometry such as bottom-end effects, sample rupture (especially at high particle fraction), free surface deformation and flow instabilities are amplified, with little ways of alleviating their disturbing effects. It is worth recalling that these effects include wall slip (due mainly to particle depletion at the wall [24, 138], for a more detailed discussion, please refer to section 4.4.2), shear localization [15, 71], particle migration/segregation, and the finite-size limit if one wants to use classical narrow-gap Couette cells. These difficulties have promoted the use of wide-gap geometries, but the associated Couette inverse problem (i.e., deriving the flow curve $\tau(\dot{\gamma})$ from torque measurements) calls for more sophisticated techniques than those used classically for narrow gaps. This point remains an open field of research

when studying complex fluids such as concentrated suspensions (for a more detailed discussion, please refer to section 3.2 and 4.5.1).

As a typical result of investigations into the behavior of coarse-particle suspension, we report the experimental results obtained by Ancey *et al.* [11, 15] on glass beads immersed in various interstitial fluids and sheared by a vane. Figure 2.3 shows the variation in the dimensionless shear stress $S = \tau/(\rho g h)$ (h is the thickness of material sheared by the vane, ρ its density) as a function of a dimensionless number $\Gamma = \mu\Omega/(\rho' g h)$ (where Ω is the rotational speed of the vane, ρ' the buoyant density, μ the interstitial fluid viscosity). This experiment shows the transition from a frictional (Coulomb) regime to a viscous-like regime:

- At low shear velocities ($\Gamma \ll 1$), S is independent of Γ, which implies that: (i) $\tau \propto \sigma_{zz}$ (where σ_{zz} denotes the vertical normal stress) and (ii) τ does not depend on the shear rate.

- At high rotational speed, all the material was sheared in the gap. We observed that $S \propto \Gamma$, that is, in terms of dimensional variables, $\tau \propto \dot\gamma$.
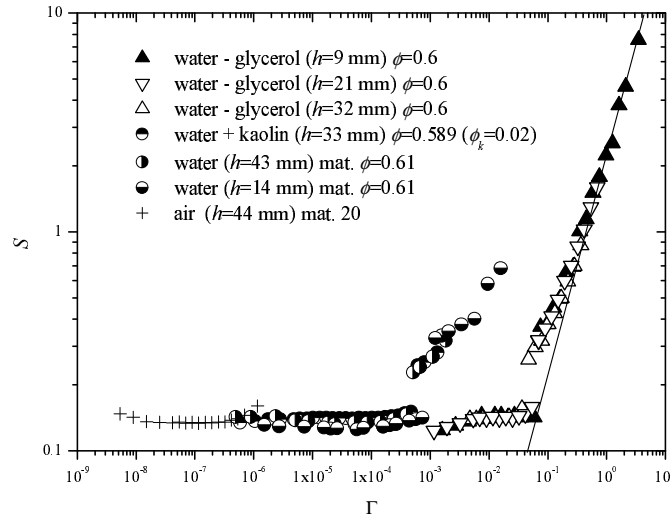
Figure 2.3: Variation in the dimensionless shear stress as a function of the dimensionless number Γ. The line slope is unity and indicates a linear variation of S with Γ. Suspensions made up of glass beads and various interstitial fluids: air ($\mu = 1.8 \times 10^{-5}$ Pa.s), water ($\mu = 10^{-3}$ Pa.s), water-glycerol solution ($\mu = 0.96$ Pa.s, $\rho_f = 1260$ kg/m^3), and water-kaolin dispersion. The particle diameter was either 0.3 mm, 0.8 mm, 1 mm, 2 mm, or 3 mm. After [11].

If this transition is well understood qualitatively from the theoretical viewpoint, certain points remain unclear. For instance, the point of transition between the frictional and viscous regimes was found to be particle-size dependent, which remains unexplained.

There has been a significant change of perception in rheometry over the last two decades. Until the late 1980s, most of the knowledge in concentrated particle suspensions stemmed from macroscopic measurements. In the last 20 years, a new trend has emerged, where flow behavior is investigated locally using visualization techniques. Recently sophisticated tools such as Magnetic Resonance Imaging (MRI) [34, 73, 229] have been used to visualize flow behavior inside a rheometer. Good reviews on the use MRI in fluid mechanics can be found in Callaghan [50] and Fukushima [105]. Making use of this technique,

experimentalists are faced with severe constraints that limit their interest for studying complex, time-dependent rheological behavior.

Table 2.2: Relative viscosity η_r functions of concentrated particle suspensions

$\eta_r = 1 + 2.50 \cdot \phi$ [95, 96]

$\eta_r = 1 + k_1 \cdot \phi + k_2 \cdot \phi^2$ [29, 32, 93, 94, 167, 301]

$\eta_r = \dfrac{25}{16} \left(\dfrac{\phi^2}{(1 - \phi/\phi_{max})^2} \right)$ [94]

$\eta_r = \exp \left[C \dfrac{h\phi}{(1 - h\phi)} \right]$ [19]

$\eta_r = \exp \left[\dfrac{5}{2} \left(\dfrac{\phi}{(1 - K\phi)} \right) \right]$ $1.35 < K < 1.91$ [205]

$\eta_r = \exp(1 + k_1 \cdot \phi + k_2 \cdot \phi^2)$ [258]

$\eta_r = \dfrac{54}{4f^3} \left(\dfrac{\phi^2}{(1 - \phi/\phi_{max})^3} \right)$ $1 < f < 2$ [275]

$\eta_r = \dfrac{1}{(1 - \phi)^{5/2}}$ [43, 256]

$\eta_r = 1 + \dfrac{2}{\sqrt{(\phi/\phi_{max})^2 - 1}} \ \tan^{-1} \left(\sqrt{\dfrac{\phi/\phi_{max} + 1}{\phi/\phi_{max} - 1}} \right)$ [5]

$\eta_r = (1 - \phi/\phi_{max})^n$ [52, 164, 165, 197, 244, 245]

$\eta_r = \left(1 - \dfrac{\phi}{\phi_{max}} \right)^{-2}$ [152, 187]

$\eta_r = \dfrac{9}{8} \left(\dfrac{(\phi/\phi_{max})^{1/3}}{1 - (\phi/\phi_{max})^{1/3}} \right)$ [104]

$\left. \begin{array}{l} \eta_{r\infty} = (1 - 1.47\phi)^{-1.82} \\ \eta_{r0} = (1 - 1.75\phi)^{-1.50} \end{array} \right\}$ [230, 310]

$\eta_r = \left[1 + 0.75 \left(\dfrac{(\phi/\phi_{max})}{1 - \phi/\phi_{max}} \right) \right]^2$ [62]

$\eta_r = \left(1 - 1.033 \dfrac{\phi}{\phi_{max}} \right)^{-1.8}$ [55]

$\eta_r = 1 + C\dfrac{3\pi}{8} \dfrac{\beta}{\beta + 1} \left[\dfrac{3 + 4.5\beta + \beta^2}{\beta + 1} - 3\left(1 + \dfrac{1}{\beta} \right) ln(\beta + 1) \right]$ [266]

$$\beta = \dfrac{(\phi/\phi_{max})^{1/3}}{1 - (\phi/\phi_{max})^{1/3}}, C \sim 1$$

$\eta_r = \dfrac{\exp(-2.34\phi)}{(1 - \phi/\phi_{max})^3}$ [316]

Measurement techniques

In rheometry, particle suspensions pose substantial difficulties of different nature:

- measurement problems: the idea underpinning rheometry is that by imposing a simple shear flow (viscometric flow in the parlance of rheologists), we should be able to take bulk measurements that can be interpreted in terms of stress and strain rate. Achieving viscometric flows in modern rheometers is rather simple for usual fluids, but remains a challenge for complex fluids because of the occurrence of several disturbing processes (slip, shear banding, size effect, etc.);

- inference problems: the flow curve $\tau(\dot{\gamma})$ from bulk measurements is usually derived within the framework of viscometric flow theory. This theory relies on a number of assumptions and approximations, which may be not be satisfied.

In this chapter devoted to experimental techniques, we will review the different difficulties encountered in the rheometry of coarse-particle suspensions. We first start in § 3.1 by recalling some basic problems when selecting an appropriate rheometrical geometry. On the basis of past experience, the Couette cell (also called coaxial-cylinder geometry) turns out to be the most efficient geometry for our purposes. In § 3.2, we will tackle the delicate problem of the flow-curve derivation, i.e. reconstructing the field $\tau(\dot{\gamma})$ from a discrete set of bulk measurements $M_i(\Omega_i)$ with M torque and Ω spindle's rotational velocity. This derivation involves solving an inverse problem (Fredholm equation) for which several methods are now available. We will test and compare the various techniques.

To get around experimental difficulties with classic rheometers, a growing number of scientists have been tempted to derive the flow curve by directly measuring the velocity field inside the cell. Indeed, if flow is viscometric, the shear stress distribution across the gap $\tau(r)$ (with r being the radial coordinate) is imposed and known (using the momentum balance equations for continua), which implies that if we are able to measure the fluid velocity v (orthoradial component) and differentiate it, we can obtain the local shear rate $\dot{\gamma}(r) = r^{-1}\partial_\theta v$ and thereby, the flow curve $\tau(\dot{\gamma})$. Nuclear Magnetic Resonance (NMR) and Magnetic Resonance Imaging (MRI) have been increasingly used to obtain velocity measurements inside sheared samples. Although these techniques are efficient, they involve expensive tools and heavy procedures. In this thesis, I took another approach: there are now several visualization techniques based on *particle image velocimetry* (PIV) and *particle tracking velocimetry* (PTV) that enable visualization inside concentrated suspensions. There are many advantages of this approach over MRI and NMR techniques: reasonable cost, robustness and versatility of the techniques, greater accuracy. There are also some drawbacks: we must work with transparent suspensions and experiments are highly sensitive to temperature and humidity, which imposes drastic temperature and humidity control. In § 3.3, I show how PIV techniques can be used to obtain the velocity profiles of highly concentrated particle suspensions. To obtain information on the disperse phase, we must be able to track tagged particles within the interstitial fluid. In § 3.4, I present techniques coupling fluorescent dyes and PIV, which are referred to

as fPIV techniques. Within this experimental framework, the crux lies in suspension transparency. Since particle suspensions are not transparent in the visible spectrum, we must select fluid and particles with the same refractive index. The principle is straightforward, the technique is heavy. In § 3.5, I present the procedures I followed to match refractive indices of continuous and disperse phases.

3.1   Rheometrical investigations

Coarse particle suspensions have been studied in rheometry using several different tools. These tools can be classified as follow:

- viscometric flow tools: concentric-cylinder, parallel-plate, cone-and-plate, cone-cone, capillary tubes, etc.

- non-viscometric flow tools: rotating ball rheometer [264], falling needle viscometer [232].

We restricted ourselves to viscosimetric flow tools where no empirical constant has to be used to derive the flow curve of a suspension. When studying rheological properties of particle suspensions, experimentalists are faced with a number of problems resulting from the presence of particles:

- For noncolloidal particle suspensions, the typical particle size is most often large relative to the gap of usual rheometers. This leads to developing large rheometers or adapting conventional geometries.

- Disturbing effects such as slipping and particle depletion at the shearing surface affect measurements. This motivates the development of specific procedures and new tools. For instance, the vane shear cell (imported from soil mechanics) is now increasingly used in rheometry [25] although it was vigorously criticized in the 1990s.

- Imposing a simple shear flow is a difficult task: ill-understood phenomena such as secondary flow (loss of stability induced by inertia), fracturation, shear localization, and particle migration can substantially influence rheological behavior.

- Rheometrical measurements can be affected by large stress (or shear-rate) fluctuations, which poses two problems:

  – Does it make sense to only measure mean properties? Let us use the analogy with turbulent flows: measuring turbulent viscosity with a rheometer is meaningless since this bulk viscosity is not an intrinsic property of the fluid, but depends on the boundary conditions and flow geometry.

  – The flow curve $\tau = f(\dot{\gamma})$ (namely the relationship between the shear rate $\dot{\gamma}$ and the shear stress τ) is obtained by solving an inverse problem. Usual methods are very sensitive to noise and can lead to inconsistent results [35].

- The principle of rheometry is to impose viscometric flow conditions, that is, ideal flow conditions where the stress and/or shear-rate distributions are known in advance. For particle suspensions, the only information that can be provided by a rheometer is the flow curve $\tau = f(\dot{\gamma})$ and, sometimes, one of the normal stresses. Contrary to a trixial cell used in soil mechanics, a rheometer cannot explore various "loading" paths and therefore, it is not experimentally possible to measure all the components of the stress tensor.

Because of the rheometrical difficulties described above and our particular interest in the rheophysics of concentrated non-colloidal particle suspension, we have developed an innovative experimental setup by combining classical concentric-cylinder rheometrical measurements and visualization techniques. We preferred the concentric-cylinder geometry over other geometries because it seems to be the most suitable geometry for the study of coarse-grain suspensions.

3.2 Wide-gap rheometry and the Couette inverse problem

A longstanding problem in rheometry is the so-called Couette inverse problem, in which one tries to derive the flow curve $\tau(\dot{\gamma})$ from the torque measurements $M(\Omega)$ in a coaxial cylinder (Couette) rheometer, where τ is the shear stress, $\dot{\gamma}$ denotes the shear rate, Ω is the rotational velocity of the inner cylinder, and M represents the torque per unit height (Coleman *et al.* [68], $T_{tot} = h \cdot M$, T_{tot} is the total torque and h is the immersed height of the rod). The shear stress τ_{in} exerted on the inner cylinder of radius R_{in} can be directly related to the measured torque M by $\tau_{in} = \alpha M$, with $\alpha = \frac{1}{2\pi R_{in}^2}$, independently of the form of the constitutive equation. The shear rate is related to the rotational velocity Ω by

$$\Omega = \int_{R_{in}}^{R_{out}} \frac{\dot{\gamma}(r)}{r} dr, \tag{3.1}$$

where R_{out} denotes the outer-cylinder radius and it is assumed that (i) the rotational velocity of the outer cylinder is zero and (ii) there is no slip between the inner cylinder and the sheared material. In order to recover the flow curve from measurements of the rotational velocity $\Omega(M)$, one must be able to

1. infer the shear stress τ from the torque measurements T_{tot},

2. find out a means of inverting the integral relationship 3.1 to obtain the shear rate $\dot{\gamma}$,

3. relate the function $\dot{\gamma}(r)$ to $\tau(r)$,

4. estimate the continuous function $\dot{\gamma}(r)$ from a set of discrete values (Ω_i, M_i).

For a broad class of fluids (called *simple fluids* in viscometry), the first and third steps are systematically achieved since there is a one-to-one relation between the shear stress and the shear rate for steady viscometric flows: $\dot{\gamma} = \dot{\gamma}(r)$. Using narrow-gap Couette cells and solving the Couette inverse problem with standard narrow-gap approximation formulas (FPP [68, 86, 183], Euler [66, 86], Mooney [204, 206]) or truncated infinite series [159] (see table 3.1) performs very well.

For more complex fluids (such as yield stress fluids, particle suspensions,...), inferring the flow curve $\tau = f(\dot{\gamma})$ from the torque and angular velocity (Ω_i, M_i) measurements is not obvious. It is not always straightforward to infer the shear stress from the total torque because the local shear stress may depend on flow height, i.e. on normal stresses as shown by Ancey and Coussot [15] for particle suspensions in the frictional regime. Furthermore inverting equation (3.1) requires an homogenous flow in the gap. Therefore the experimentalist has to check for shear localization and wall slip. Finally, the flowing material is supposed to be homogenous. Some of the existing techniques use an *a priori* known velocity profile in the gap, i.e. an *a priori* known fluid rheology (see Table 3.2 number 2a, 4, 5). Typical fluids are power law fluids, Casson fluids, Bingham fluid or Herschel-Bulkley fluids. Some of the techniques do not require a fluid rheology. An extensive review of the existing techniques for solving the Couette inverse problem can be found in Table 3.2.

As briefly mentioned in § 2.4, because of the particle size in concentrated non-colloidal particle suspensions and the resulting finite size effect in a narrow-gap rheometer, one has to use wide-gap geometries for experimental studies of coarse-particle suspensions. In this way, we get rid of the size

effects, but we have to face a delicate issue: we have to solve the Couette inverse problem to obtain the flow curve $\tau(\dot{\gamma}) = f(\dot{\gamma})$ from a set of measurements values (Ω_i, M_i).

Figure 3.1 shows the effect of increasing the gap, i.e.decreasing the radius ratio κ, with a given fluid (artificial Herschel-Bulkley (HB) fluid). The data shown in figures 3.1 to 3.7 were obtained using formula No. 8 in Table 3.2 and by generating numerically a set of "artificial measurement data" (Ω_i, M_i). Using then Couette solving methods, we calculated the flow curve $(\dot{\gamma}, \tau)$ from these data. The performance of each method can finally be evaluated by comparing it with the known true flow curve (thick blue line). In the case $\kappa = 0.9$ (fig. 3.1 (a)), one can use almost all methods (except infinite-gap methods) to retrieve the right flow curve. One can also see in Figure 3.1 (b), (c) and (d) the departure with decreasing κ of the different methods from the true flow curve.

Table 3.1: Couette inverse problem solving formulas for narrow-gap Couette cells

1) Very narrow-gap

$$\dot{\gamma} = \frac{\Omega R_{mean}}{R_{out} - R_{in}}, \qquad R_{mean} = \frac{R_{out} + R_{in}}{2}, \qquad \kappa = \frac{R_{in}}{R_{out}} > 0.99, \qquad [183]$$

2) Flat parallel plates (FPP)

$$\dot{\gamma} = \frac{\Omega}{1 - \kappa}, \qquad \kappa = \frac{R_{in}}{R_{out}}, \qquad [86]$$

3) Second flat parallel plates formula (FPP)

$$\dot{\gamma} = \frac{\Omega}{s - 1}, \qquad s = \frac{R_{out}}{R_{in}}, \qquad [68]$$

4) The Euler Formula

$$\dot{\gamma} = \frac{2\Omega}{(1 - s^2)}, \qquad s = \frac{R_{out}}{R_{in}}, \qquad [66, 86]$$

5) Mooney's solution (1931)

$$\dot{\gamma} = \frac{\Omega}{\epsilon} = \frac{R_{out}^2 + R_{in}^2}{R_{out}^2 - R_{in}^2}\,\Omega \qquad [204, 206, 263]$$

6) Hersey's method (1932)

$$\dot{\gamma} = \left(\frac{2\kappa^2}{1 - \kappa^4}\right) F(\tau_{in}) + \left(\frac{1}{1 + \kappa^2}\right) \tau_{in} F'(\tau_{in}) \qquad [128, 263]$$

$F(\tau_{in})$ is the functional relationship between Ω and τ_{in} : $\quad 2\Omega = \int_{\tau_{out}}^{\tau_{in}} \frac{\dot{\gamma}(\tau)}{\tau} d\tau$

and $F'(\tau_{in})$ his derivative with respect to τ_{in}

7) Two bob method, Krieger (1952)

$$\dot{\gamma} = -s\frac{\partial \Omega}{\partial s} \cong -s_m \frac{\Delta\Omega}{\Delta s}\bigg|_{C=cst}, \qquad s_m = \frac{s_a + s_b}{2}, \; s_a = \frac{R_{out}}{R_a}, \; s_b = \frac{R_{out}}{R_b} \qquad [159, 263]$$

$$\Delta\Omega = \Omega_b - \Omega_a, \; \Delta s = s_b - s_a$$

Table 3.2: Couette inverse problem solving formulas for wide- and infinite-gap Couette cells

Wide − gap

1) Bernoulli polynomial solution	$\dot\gamma(\tau_{in}) = \dfrac{\Omega(\tau s^{2\alpha})}{ln\,s} + \sum_{k\geq 0} B_k(1-\alpha)\dfrac{d^k\Omega(\tau s^{2\alpha})}{d\tau^k},$ $s = \dfrac{R_{out}}{R_{in}},\ B_k$ denote a Bernoulli polynomial of degre k, $0 < \alpha < 1,$	[84, 86]
1a) Bernoulli polynomial solution ($\alpha = 0$)	$\dot\gamma(\tau_{in}) = \dfrac{\Omega}{ln\,s}\left[1 + ln\,s\,\dfrac{d\,ln\,\Omega}{d\,ln\,\tau_{in}} + \dfrac{(ln\,s)^2}{3\Omega}\dfrac{d^2\Omega}{d(ln\,\tau_{in})^2} - \dfrac{(ln\,s)^4}{45\Omega}\dfrac{d^4\Omega}{d(ln\,\tau_{in})^4} + \cdots\right]$ $s = \dfrac{R_{out}}{R_{in}},$	[68, 84, 86, 158]
Krieger (1953)		[160, 234, 263]
1b) Bernoulli polynomial solution ($\alpha = 0.5$)	$\dot\gamma_{MP} = -\dfrac{\Omega(\tau_{in}\kappa^{-1})}{ln\,\kappa} = \dfrac{\Omega(\tau_{in}s)}{ln\,s}$ $s = \dfrac{R_{out}}{R_{in}},\ \kappa = \dfrac{R_{in}}{R_{out}}$	[84, 86]
Mid point approximation		
1c) Bernoulli polynomial solution ($\alpha = 0.5$)	$\dot\gamma_{MMP} = -\dfrac{2\kappa\Omega(\tau_{in}\kappa^{-1})}{1-\kappa^2} = \dfrac{2s\Omega(\tau_{in}s)}{s^2-1}$ $s = \dfrac{R_{out}}{R_{in}},\ \kappa = \dfrac{R_{in}}{R_{out}}$	[84, 86]
Modified mid point approximation		
1d) Bernoulli polynomial solution ($\alpha = 0.5$)	$\dot\gamma_{TTFD} = \dfrac{1}{-24ln\,\kappa}(-\Omega(\tau\kappa^{-3}) + 26\Omega(\tau\kappa^{-1}) - \Omega(\tau\kappa))$ $\kappa = \dfrac{R_{in}}{R_{out}}$	[84, 86]
3 term finite difference approximation		
1e) Bernoulli polynomial solution ($\alpha = 0.5$)	$\dot\gamma_{MTTFD} = \dfrac{2\kappa}{1-\kappa^2}\left(\dfrac{-\Omega(\tau\kappa^{-3}) + 26\Omega(\tau\kappa^{-1}) - \Omega(\tau\kappa)}{-\kappa^{-2} + 26 - \kappa^2}\right)$ $\kappa = \dfrac{R_{in}}{R_{out}}$	[84, 86]
Modified 3 term finite difference approximation		

Description	Equation	Ref.
$1f$) Bernoulli polynomial solution ($\alpha = 0.5$) 5 term finite difference approximation	$$\dot\gamma_{FTFD}(\tau_{in}) = \frac{9\Omega(\tau\kappa^{-5}) - 116\Omega(\tau\kappa^{-3}) + 2134\Omega(\tau\kappa^{-1}) - 116\Omega(\tau\kappa) + 9\Omega(\tau\kappa^3)}{-1920 ln\,\kappa}$$ $\kappa = \dfrac{R_{in}}{R_{out}}$	[84, 86]
$1g$) Bernoulli polynomial solution ($\alpha = 0.5$) Modified 5 term finite difference approximation	$$\dot\gamma_{MFTFD} = \frac{2\kappa}{1-\kappa^2}\left(\frac{9\Omega(\tau\kappa^{-5}) - 116\Omega(\tau\kappa^{-3}) + 2134\Omega(\tau\kappa^{-1}) - 116\Omega(\tau\kappa) + 9\Omega(\tau\kappa^3)}{9\kappa^{-4} - 116\kappa^{-2} + 2134 - 116\kappa^2 + 9\kappa^4}\right)$$ $\kappa = \dfrac{R_{in}}{R_{out}}$	[84, 86]
$1h$) Bernoulli polynomial solution Krieger (1968)	$$\dot\gamma(\tau_{in}) = \frac{2N\Omega_{in}}{1-s^{-2N}}\left[1 + \frac{\frac{dN}{d ln\tau_{in}}f(t)}{N^2}\right]$$ $s = \dfrac{R_{out}}{R_{in}}, t = 2N ln\,s, N = \dfrac{d ln\Omega}{d ln\tau_{in}}, f(t) = \dfrac{t^2}{12}\left[1 - \dfrac{t}{2} + \dfrac{t^2}{15} + ...\right]$	[163]
$1i$) Bernoulli polynomial solution Krieger (1969)	$$\dot\gamma(\tau_{in}) = \frac{2N\Omega_{in}}{1-s^{-2N}}\left\{1 + N^{-2}N^{(1)}f_1(t) + N^{-3}N^{(2)}f_2(t) + N^{-4}[3(N^{(1)})^2 + N^{(3)}]f_3(t) + ...\right\}$$ $s = \dfrac{R_{out}}{R_{in}}, t = 2N ln\,s, N = \dfrac{d ln\Omega}{d ln\tau_{in}}, N^{(r)} = \left(\dfrac{d}{d ln\tau_{in}}\right)^r N$ $f_1(t) = \dfrac{t^2}{12}\left[1 - \dfrac{t}{2} + \dfrac{t^2}{15} + ...\right], f_2(t) = \dfrac{-t^4}{120}(1 - 4t + ...), f_3(t) = \dfrac{-t^6}{720} + ...$	[162]
$2a$) Power-law formula ($\dot\gamma = \alpha\tau^m$)	$$\dot\gamma_{PL}(\tau_{in}) = \frac{2m\Omega_{in}}{1-\kappa^{2m}}$$ $m = \tau_{in}\dfrac{\Omega'(\tau_{in})}{\Omega\tau_{in}}$	[66]
$2b$) Modified power-law formula ($\dot\gamma = \alpha\tau^m$)	$$\dot\gamma_{MPL}(\tau_{in}) = 2\frac{\Omega(\sigma)m(\sigma)}{(1-s^2m(\sigma))}s^{2\alpha m(\sigma)},$$ $\sigma = \tau_{in}s^{-2\alpha}, m = \tau_{in}\dfrac{\Omega'(\tau_{in})}{\Omega\tau_{in}}$	[84]
3) Partially sheared fluid (yield stress fluid)	$$\dot\gamma(\tau_{in}) = 2\Omega\frac{d ln\Omega}{d ln\tau_{in}}$$ $\tau_{out} < \tau_y < \tau_{in}$	[101, 183, 213, 214]
4) Bingham fluid ($\tau = \tau_0 + \mu\dot\gamma$) Fully sheared gap	$$\dot\gamma = 2\frac{T(d\Omega/dT)}{1-\kappa^2} - \frac{\Omega - T(d\Omega/dT)}{ln\,\kappa}$$ $\kappa = \dfrac{R_{in}}{R_{out}}, \tau_{out} > \tau_y$	[101, 124]

5) Herschel-Bulkley fluid ($\tau = \tau_0 + K\dot{\gamma}^n$)	$\dot{\gamma}(r) = \frac{1}{2} K^{-1/n} (\tau(r) - \tau_0)^{1/n} \left(\frac{\tau_0}{\tau(r)}\right)^{1/n} \left(1 - \frac{\tau_0}{\tau(r)}\right)^{-1/n} \beta\left[\frac{\tau_0}{\tau(r)}, -\frac{1}{n}, 1+\frac{1}{n}\right]$ $\frac{1}{n} \neq 0, 1, 2, 3, ...$ the incomplete Euler Beta function $\beta[z,a,b] = \int_0^z t^{a-1}(1-t)^{b-1} dt$ $\frac{1}{n} = 2 : \dot{\gamma}(r) = \dfrac{-\frac{\tau^2(r)}{4} + \tau(r)\tau_0 + \tau_0^2 \, ln\, r}{K^2}$ $\frac{1}{n} = 3 : \dot{\gamma}(r) = -\dfrac{1}{K^3}\left[\frac{\tau^3(r)}{6} - \frac{3\tau(r)\tau_0}{4} + \frac{3\tau(r)\tau_0^2}{2} + \tau_0^3 \, ln\, r\right]$ $\frac{1}{n} = ...$	[never published]
6) Tanner and Williams (1970)	Iterative method	[285]
7) Macsporran (1987,1989)	Projection approach using cubic polynomial/spline	[184, 185]
8) Yeow (2000,2003)	Tikhonov regularization technique	[174, 312]
9) Ancey (2005)	Wavelet-vaguelette decomposition	[12]
Infinite − gap		
10) Infinite gap, Krieger (1952)	$\dot{\gamma}_\infty(\tau_{in}) = \dfrac{2d\Omega}{d\,ln\,(\tau_{in})}$	[137, 159]
11) Infinite gap 2, Thornton (1953)	Differentiation of an infinite series	[289]

(a)

(b)

Figure 3.1: Comparison of Couette solving methods with respect to the cylinder radius ratio for a Herschel-Bulkley fluid ($\tau_0 = 30$ [Pa], $K = 60$ [Pa s^{-n}] and $n = 0.7$ [-])$\kappa = \frac{R_{in}}{R_{out}}$: (a) $\kappa = 0.9$, (b) $\kappa = 0.75$, (c) $\kappa = 0.5$ and (d) $\kappa = 0.2$; the two black horizontal lines are where the yield stress τ_0 is equal to the inner and outer shear stress τ_{in} and τ_{out}.
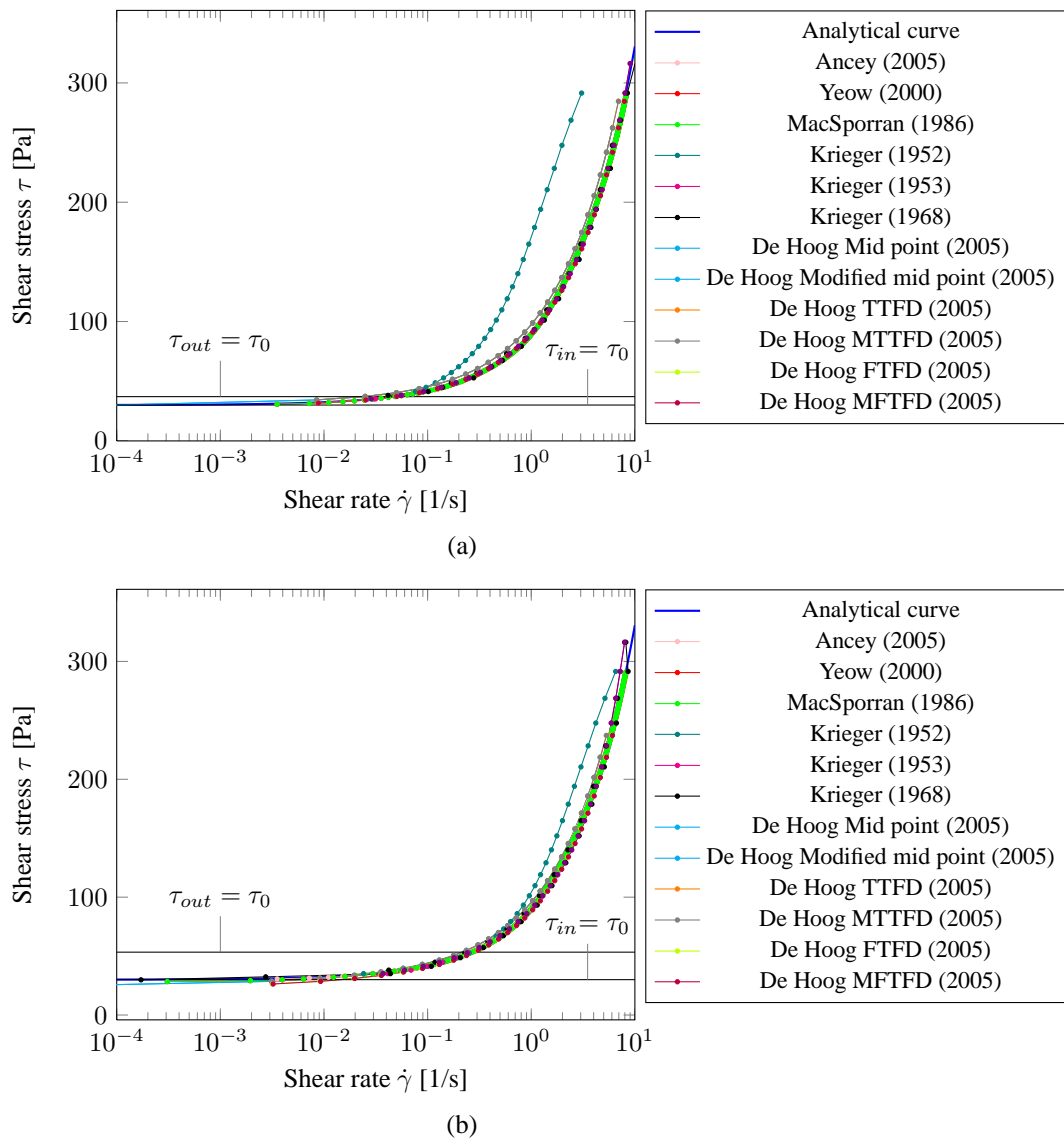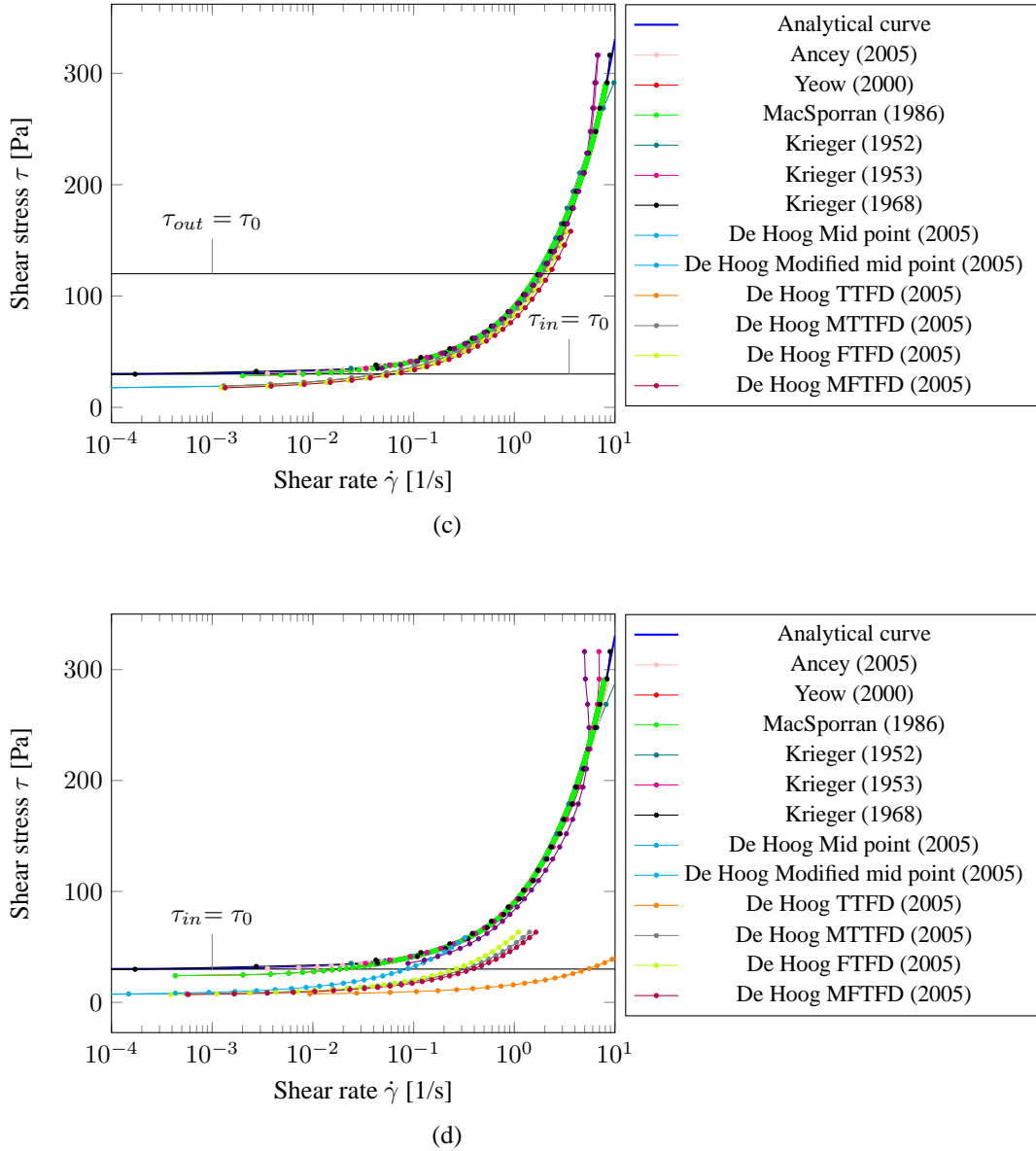
(c)

(d)

Figure 3.1: Comparison of Couette solving methods with respect to the cylinder radius ratio for a Herschel-Bulkley fluid ($\tau_0 = 30$ [Pa], $K = 60$ [Pa s^{-n}] and $n = 0.7$ [-]) $\kappa = \frac{R_{in}}{R_{out}}$: (a) $\kappa = 0.9$, (b) $\kappa = 0.75$, (c) $\kappa = 0.5$ and (d) $\kappa = 0.2$; the two black horizontal lines are where the yield stress τ_0 is equal to the inner and outer shear stress τ_{in} and τ_{out}.

One method that clearly performs better with increasing κ is the infinite-gap method proposed by Krieger (1952) [159]. With a yield stress fluid an infinite gap is equivalent to a partially sheared gap, i.e. when the outer shear stress τ_{out} is below the yield stress τ_0. Figure 3.2 and 3.3 show the almost exact recovery of the flow curve in a partially sheared state and the curve take-off at $\tau_{out} = \tau_0$.
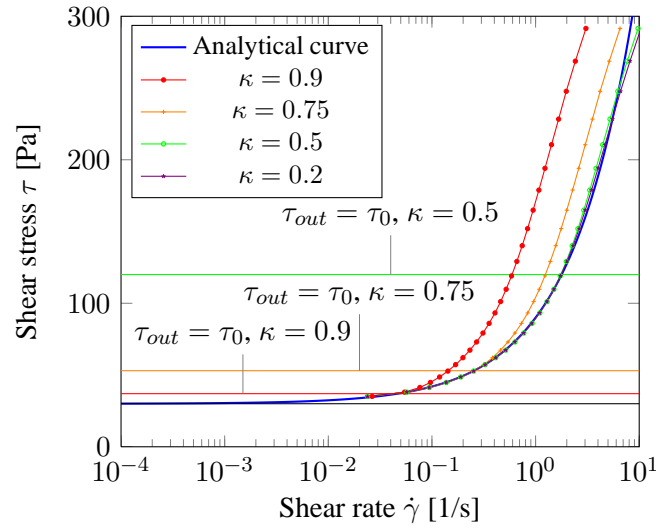
Figure 3.2: Comparison between the HB analytical flow curve ($\tau_0 = 30$ [Pa], $K = 60$ [Pa s^{-n}] and $n = 0.7$ [-]) and the data obtained with the infinite-gap exact equation proposed by Krieger (1952) [159], the horizontal lines are where the yield stress τ_0 is equal to the inner shear stress τ_{in} (lowest horizontal black line) and outer shear stress τ_{out} (colored lines) for various radius ratios.
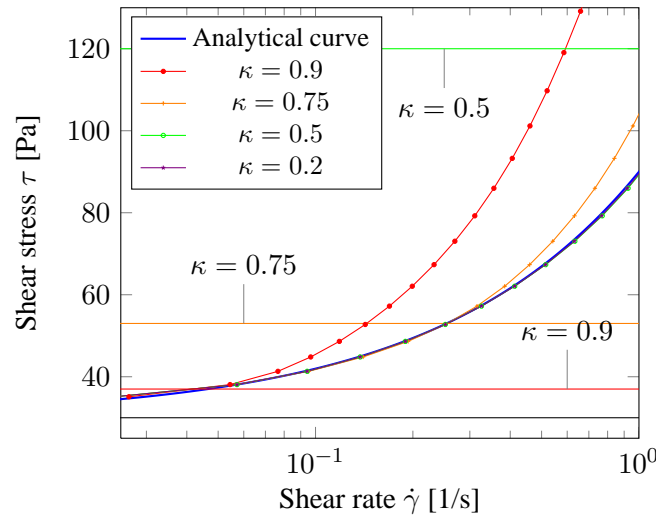

Figure 3.3: Zoom of the take-off at $\tau_{out} = \tau_0$ of the $\kappa = 0.9$ and $\kappa = 0.75$ flow curves of figure 3.2.

Using the exact infinite series formula proposed by Krieger and Elrod (1953) [158] gives accurate results, but one has to compute high-order derivatives, which remains a difficult task when data are noisy. Fgure 3.4 shows how well the method performs when increasing the number of terms. Krieger proposed also a method for Newtonian and power-law fluids (Krieger 1968,1969 [163, 162]). This method performs poorly with yield stress fluids, especially if it is partially sheared within the gap and also with noisy data (Borgia and Spera (1990) [35]). In this case, Nguyen and Boger (1992) [214] have proposed using the Krieger (1952) infinite-gap exact formula. Noise is also an important parameter for

more sophisticated techniques such as the discretized integral approach proposed by MacSporran (1987) [185]. The effect of various noise level on the (Ω_i, M_i) is shown in Fig. 3.5. To solve this problem, regularization techniques were used (MacSporran 1989 [184], Yeow *et al.* 2000 [312] and Leong *et al.* 2003 [174]). However, when the rheological behavior exhibits singularities such as a yield stress or rapid shear-thickening, the regularization procedure can lead to unrealistic results by smoothing out the singularities (see for example Fig. 3.6). For complex rheological responses, it becomes difficult to discern rheological properties, noise effects, and discretization errors.
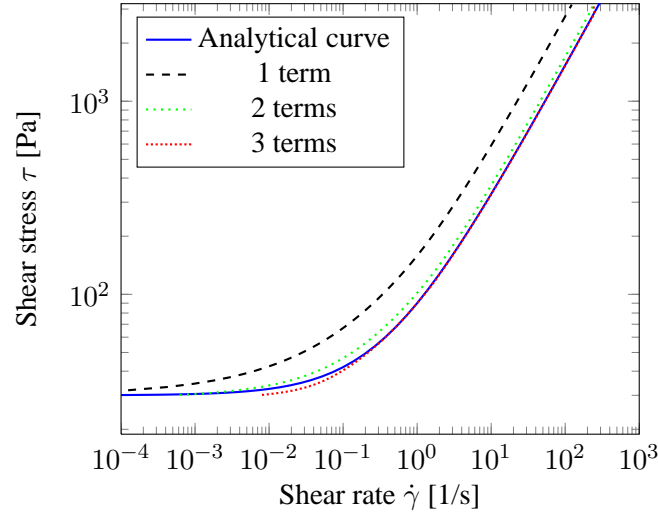
Figure 3.4: Comparison between the HB analytical flow curve and the data obtained with Krieger and Elrod infinite series [158] with 1, 2 and 3 terms of the series with $\kappa = 0.5$
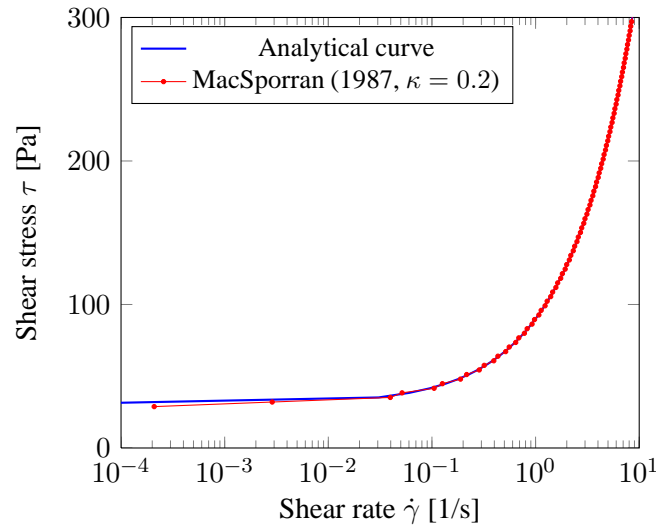
(a)

Figure 3.5: Effect of noise on the discretized integral approach of MacSporran (1987) [185]: (a) no noise, (b) and (c) increasing noise on the angular velocity / torque (Ω_i, M_i) data.
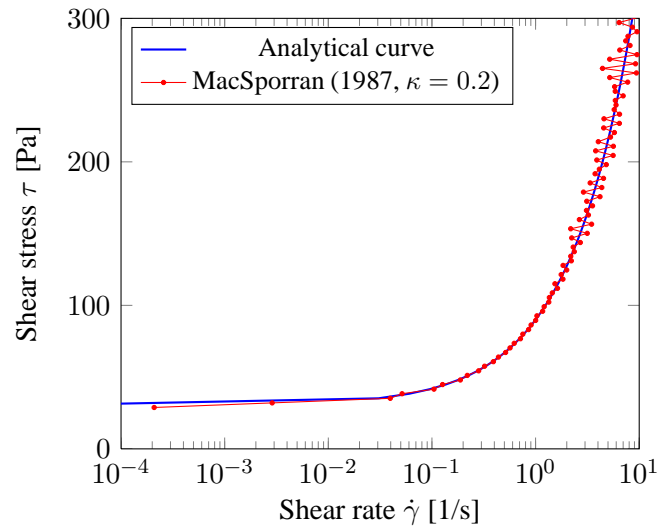
(b)
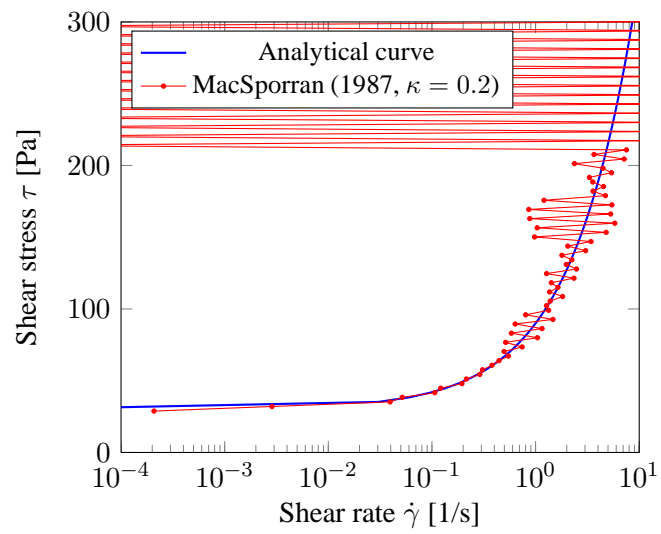
(c)

Figure 3.5: Effect of noise on the discretized integral approach of MacSporran (1987) [185]: (a) no noise, (b) and (c) increasing noise on the angular velocity / torque (Ω_i, M_i) data.
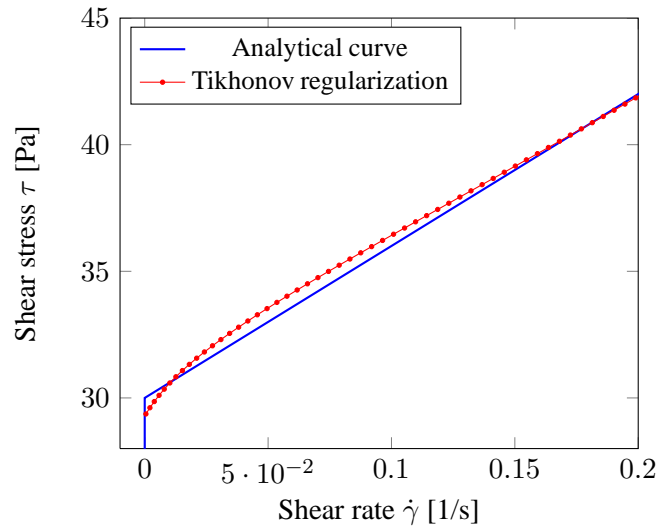
Figure 3.6: Smoothing effect of regularized least square techniques on singularities (Bingham fluid $\tau = \tau_0 + K\dot{\gamma}$, $\tau_0 = 30$ Pa and $K = 60$ Pa·s): Tikhonov regularization technique with the regularization parameter $\lambda = 7.6 \cdot 10^{-7}$ (Yeow *et al.* [312])
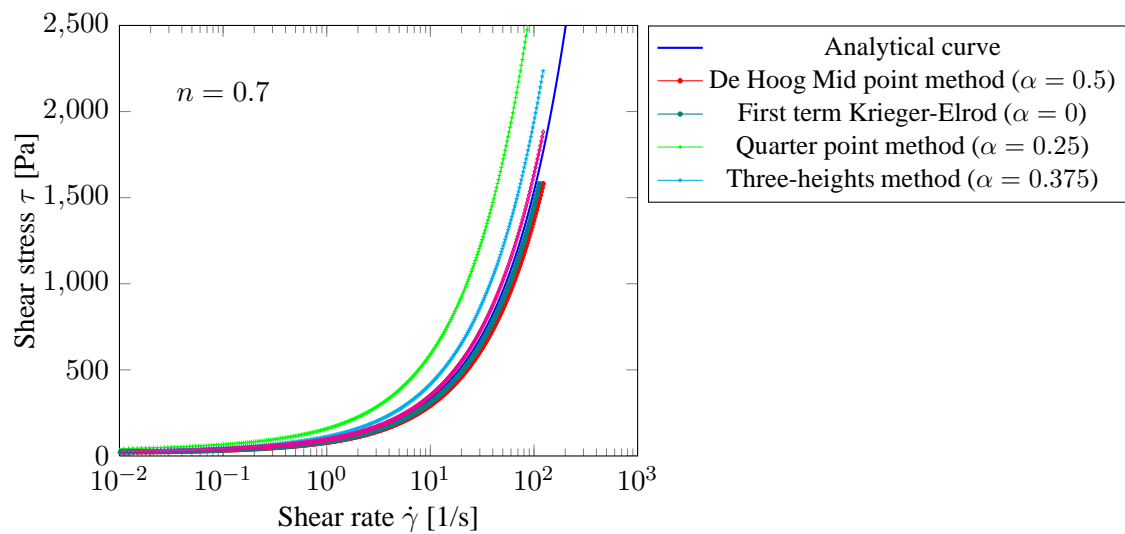
(a)

Figure 3.7: Comparison between the HB analytical flow curve ($\tau_0 = 30$ [Pa], $K = 60$ [Pa s^{-n}]) and the data obtained with the various Bernoulli polynomial solutions by varying α: (a) $n = 0.7$ and (b) $n = 0.3$.

Methods derived from a generalization of the Krieger and Elrod infinite series have recently been proposed by De Hoog and Anderssen [84, 86] (refer to table 3.2 for the detailed formula). When dealing with wide-gap geometries, the results obtained with this Bernoulli polynomial solution will vary between the Krieger-Elrod result ($\alpha = 0$) and the mid-point approximation proposed by De Hoog and Anderssen

($\alpha = 0.5$). The gap between both curves increases with decreasing radius ratio κ. Unfortunately as we can see in figure 3.7, the best method varies with the fluid rheology. In the case of a HB fluid, the most relevant parameter influencing to choice of the best α is the shear rate exponent n. For a fluid having a small exponent n, a method with a high α performs better; in contrast, with a fluid with a high exponent n, a method with a small α performs better.

(b)

Figure 3.7: Comparison between the HB analytical flow curve ($\tau_0 = 30$ [Pa], $K = 60$ [Pa s^{-n}]) and the data obtained with the various Bernoulli polynomial solutions by varying α: (a) $n = 0.7$ and (b) $n = 0.3$.
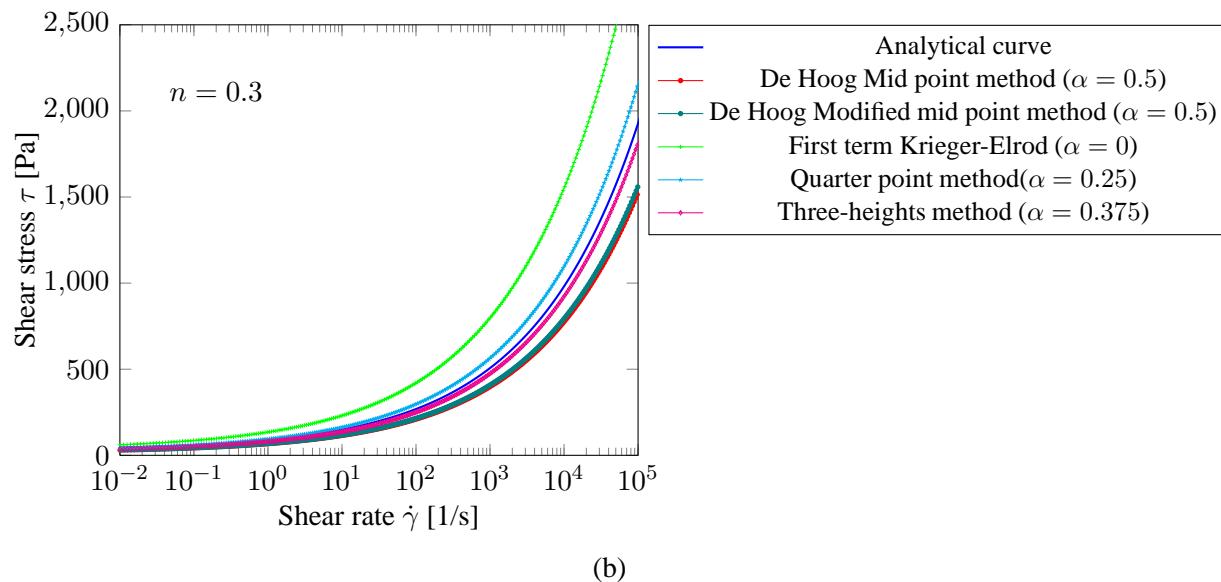
The wavelet-vaguelette decomposition proposed by Ancey (2005) [13] takes its roots in a recent extensions of the adjoint-operator method called wavelet-vaguelette decomposition (WVD). This theory was developed by Donoho (1995) [90] to solve certain classes of inverse problems. As shown by Ancey, it performs better on a Casson fluid than the Tikhonov regularization method and allows to get rid of the smoothing effect of the regularization term. This is of great importance for complex fluid exhibiting particular features in the flow curve such as rapid change, discontinuous shear rate distribution near the yield point. Main drawbacks of this technique are the mathematical complexity, computational cost and the need for denoising and interpolation techniques for the raw experimental data.

3.3 Particle Image Velocimetry

Particle image velocimetry (PIV) is an efficient method for measuring two-dimensional (and even three-dimensional) flow velocity fields. It is a non-invasive technique (i.e. it does not change the flow being measured) and possesses a fine spatial and temporal resolution. PIV is a technique based on image acquisition and pattern recognition within or between images to deduce the displacement field within the flow between these two (or more) instants. To gain quantitative knowledge of the flow motion, tracers are added to the (clear) fluid. These tracers are visible tiny particles that follow the fluid motion. By shining a laser sheet on the area of interest to enlighten the tracers, we can record the patterns produced by the random particle arrangement on successive images using a high-speed camera. Once image have

been captured, we can divide the images into sub-windows (typically 16×16 to 64×64 pixels). Auto- or cross-correlation is then used in the corresponding sub-windows to measure the pattern displacement (i.e. the fluid displacement) Δx between the images. Using advanced algorithms also allows for pattern distortion measurement. Knowing the time Δt between the exposures, we can compute the instantaneous velocity of the fluid in the sub-window. This can be done in all other sub-windows and images to end up with an instantaneous velocity map. Finally in a post-processing step, spurious vectors are removed as much as possible.

This section is divided into four parts, which are devoted to PIV in general: image acquisition in § 3.3.1 to § 3.3.4, PIV processing in § 3.3.5, PIV post-processing in § 3.3.7, and specific PIV techniques in § 3.3.8). Good reviews and books on PIV can be found in [8, 111, 252, 292].

3.3.1   Tracer particles and seeding for particle image velocimetry

Small particle motion in flow

In the limit of low Reynolds numbers, the equation of motion of a small spherical particle immersed in a fluid flow is given by

$$
\begin{aligned}
\frac{4}{3}\pi r_p^3 \rho_s \frac{d\mathbf{v}}{dt} = & \frac{4}{3}\pi r_p^3 \rho_f \frac{D\mathbf{u}}{Dt} & \text{non-inertial force} \\
& + \frac{4}{3}\pi r_p^3 (\rho_p - \rho_f)\mathbf{g} & \text{net body force} \\
& + 6\pi\mu r_p(\mathbf{u} - \mathbf{v}) & \text{quasi-steady drag force} \\
& + \mu\pi r^3 \nabla^2 \mathbf{u} & \text{Faxen force (see [121])} \\
& + \frac{2}{3}\pi r_p^3 \rho_f \left(\dot{\mathbf{u}} - \dot{\mathbf{v}} - \frac{r_p^3}{10}\frac{d}{dt}\nabla^2 \mathbf{u} \right) & \text{added mass force (see [189])} \\
& + 6r^2\sqrt{\pi\rho_f\mu}\left(\int_0^t \frac{\mathbf{u} - \mathbf{v}}{\sqrt{t - t'}}dt' + \frac{(\mathbf{u} - \mathbf{v})_0}{\sqrt{t}} \right) & \text{Basset force (see [255])} \\
& + L_{saff} & \text{Saffman lift force (see [82, 192, 260])} \\
& + L_{mag} & \text{Magnus force}
\end{aligned}
$$

where $\mathbf{u}$ is the velocity of the surrounding fluid, $\mathbf{v}$ the particle velocity. This equation is known as the Basset-Boussinesq-Oseen equation (details of its derivation can be found in Crowe *et al.* [76], see also [33, 67, 190]). For very small tracers as those used in PIV, the first part of the quasi-steady viscous term (Stokes drag) dominates the right-hand side of the equation. Assuming $D\mathbf{u}/Dt = d\mathbf{v}/dt$, we can estimate the difference between the particle and fluid velocities as

$$
\mathbf{v} - \mathbf{u} = \frac{2}{9}\frac{r^2(\rho_p - \rho_f)}{\mu}\frac{d\mathbf{v}}{dt} \tag{3.2}
$$

Clearly from 3.2 the choice of neutrally buoyant particles leads to tracers that closely follow the flow. This condition can be easily fulfilled for liquid flow. It cannot be achieved easily in gas flows.

Tracer "slavery" is quantified through the particle Stokes number St_k, defined as the ratio between, on the one hand, the product of particle relaxation time and, on the other hand, the fluid velocity to a characteristic dimension of the obstacle:
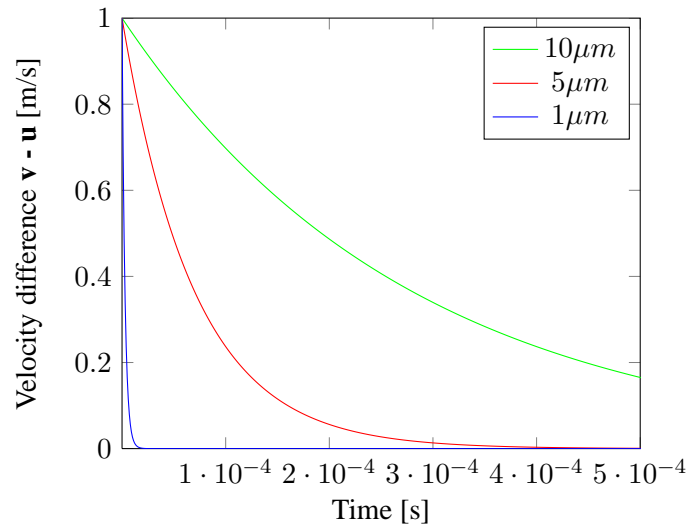
$$
St_k = \frac{\tau u_0}{l}
$$

Figure 3.8: Time response of tracers particle with different diameters in a decelerating air flow: $\mu = 1.8 \cdot 10^{-5}$ Pa·s, $\rho_p = 900$ kg/m^3.

where τ is the relaxation time of the particle, u_0 is the fluid velocity of the flow away from the obstacle and l is the characteristic dimension of the obstacle. As can be seen in figure 3.8, particles as small as possible have to be used to track fluid motion and not particle motion.

Small particle imaging

As show above, particles must be as small as possible to be tracers. However, at the same time, they have to scatter enough light to be visible. For that purpose, particle size must lie within the micrometer range (for gas flows) or tens of micrometers (for liquid flows). This implies that scattering is in the so-called *Mie scattering regime*. Another approach is to use particles containing a fluorescent dye; the light absorbed by the dye is emitted at a longer wavelength, which makes it possible to distinguish tracers form other objects.

Mie scattering of small particle

Particle scattering depends on the particle diameter, the wavelength, the refractive index of the particle relative to the surrounding fluid and the scattering angle. Most of the light is scattered in the forward direction, a substantial part is scattered backwards and at 90 ˚ (for standard 2D PIV), the scattered amount is usually very low. This is why PIV needs strong light. Because of the smaller refractive-index difference in liquid flows, bigger particles must be used to receive enough light. Fortunately in that case, it is much easier to find neutrally buoyant particle; using bigger particles (as large as tens of micrometers) can still fulfill the low-Stokes-number condition.

Fluorescent tracer particle

Particles can be tagged with a fluorescent dye (e.g. Rhodamine). The dye absorbs incident light, which is then re-emitted at a longer wavelength. This makes it possible to distinguish the tracers from other objects such as bubbles, droplets, other particles, walls, etc., by means of an appropriate optical

filter. The emission of fluorescence is isotropic, thus there is no intensity dependence on the viewing angle. Fluorescence intensity depends on the amount of fluorescent dye on the tracers; this is in general proportional to either the particle volume (d_p^3, in Mie scattering) or particle surface (d_p^2), depending on the particle tagging (bulk or surface tagging). The duration of fluorescence is typically of the order of 10 ns.

Particle generation

Some of the best suited particles for PIV measurements, such as polymers, hollow SiO2 microballoons or metallic-coated spheres, are quite complicated to fabricate (although they are today commercially available). Since these particles are quite expensive, they are better suited for closed loop systems. When larger quantities of particles are required, more economical solutions are sought and special particle generators offer a good solution, some of which are also commercially available. Particle generation can be divided into solid and liquid particles. Solid particles or powders are used to seed liquid flows and in applications such as combustion, where liquid droplets tend to evaporate. In either case, a monodispersed size distribution and a spherical particle shape are desirable, the latter condition being automatically fulfilled by small liquid droplets. Essentially, droplet can be generated by vapor condensation of highly saturated vapor stream or by liquid atomization in a gas flow. For solid particle seeding, the two main methods are constituted by dry powder and atomization as for liquid droplet. In the case of atomization, the idea is that after atomization the liquid or solvent evaporates, leaving solid particles behind.

Achieving optimum flow seeding is generally recognized as the most difficult part of PIV experiments. Once the flow is uniformly seeded at required concentration, the experiment has high chance of success. The seeding process will not be discussed in details here. For further information, the reader should refer to Melling 1997, Raffel or Tropea ([196, 252, 292], see figure 3.9).

3.3.2   Light source and light sheet optics

Lasers are routinely used for PIV measurements because they emit monochromatic light with high energy density, which can easily be bundled into a thin light sheet for illuminating and recording the tracer particles. There are two types of lasers: continuous wave (CW) lasers and pulsed lasers. In § 3.3.4, we will see how image acquisition depends on the laser type.

The light sheet can be obtained using commercially available sheet generators or by means of a set of spherical and cylindrical lenses (see for example [87, 238, 273]) and, in special cases, with an extra optic fiber [153].

The finite width of the laser sheet produces an uncertainty on the absolute position of the seeding particle in the direction perpendicular to the light sheet. This transversal motion is captured in stereoscopic PIV to get the third velocity component. Following the theory of Gaussian beam propagation (which is not absolutely valid for lasers used in PIV such as Nd:YAG lasers), the sheet thickness in the area of interest (AOI) can be calculated. Depending on laser, lenses, geometrical configuration of the experimental setup, and flow behavior, optimization of the sheet width, divergence and thickness (over the whole area of interest) can be achieved. A system of four lenses (one spherical and three cylindrical) allows to control the spreading (sheet width and divergence) and focusing of the light sheet (focusing distance and evolution of the sheet thickness) [89, 247].
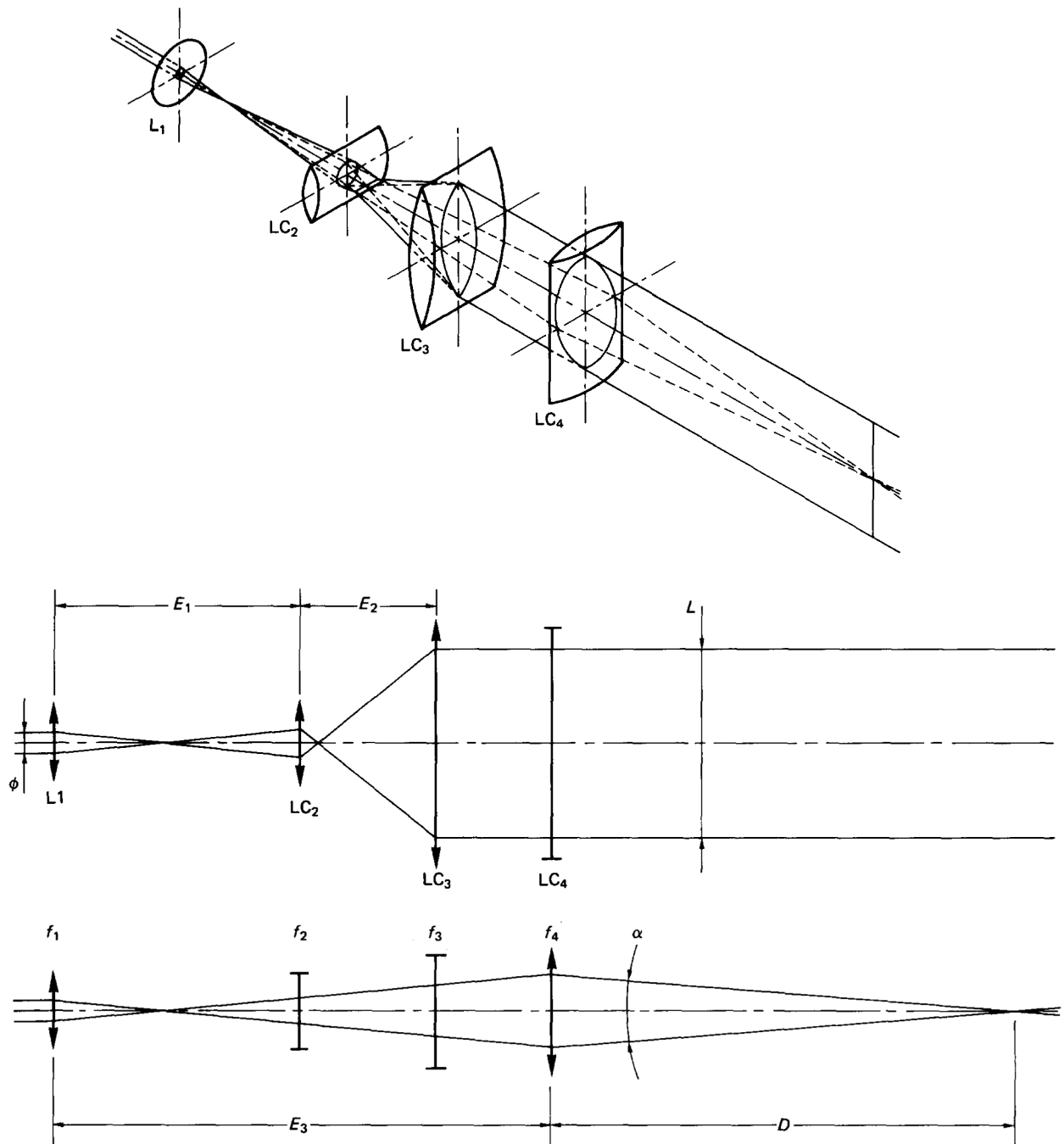
Figure 3.9: Light sheet generator (after [89]).

3.3.3   Digital camera

The present state-of-the-art in digital image allows to say that almost all PIV applications use digital cameras for recording. Immediate image availability and thus feedback during recording as well as a complete avoidance of photochemical process are some of the advantages brought by digital cameras. Even if the trend suggests that electronic recording pushes the photographic methods aside, photographic films still have higher spatial resolution than the digital cameras used in PIV and may be a better solution in some specific applications. As we will see in § 3.3.4, depending on the recording technique, two pictures have to be captured in a very short period of time. Actually there are commercially available cameras that allow time lapses as short as 100 ns. Furthermore, because cameras have their sensitivity peak in the visible green color, green laser are used for particle illumination.

3.3.4   Image recording

Recording techniques

There are several PIV recording techniques, which are listed below:

- Single frame / Single exposure

- Single frame / Two (multi) exposure

- Two (multi) frame / Single exposure

- Multi frame / Multi exposure

In single frame/single exposure PIV, a CW laser is used and the camera shutter remains open long enough so as to get strips produced by the particle motion on the images. The longer the stripes are, the higher the velocity is. An example is showed on figure 3.10. As there is no way to distinguish the beginning of a stripe to its end, a flow direction ambiguity remains with single frame techniques. This can be very problematic in complex flows. There are various methods to resolve that ambiguity such as image shifting, pulse tagging or color coding.

In single frame/single exposure, the achievement of quantitative measurement is quite difficult from an image-processing point of view.

In single frame/multiple exposure, the shutter is opened several times during the same frame acquisition. As in single frame/single exposure PIV, the directional ambiguity also exists here and the sub-window autocorrelation process gives rise to opposite correlation peaks (two peaks in single frame/double exposure).

In two or multi frame/single exposure techniques, the direction ambiguity disappears because the order in which the images were taken is known. This is the most convenient technique for image post-processing. Unfortunately in some experiments, for technical reasons, this technique cannot be used.

Most PIV experiments are actually done following a two frame /single exposure technique. Thereafter we will essentially focus on single exposure techniques.

Continous wave versus pulsed laser acquisition method

In CW-laser PIV, the laser continuously enlightens the measurement volume and the camera shutter is used to "freeze" the flow. The exposure time of each frame must be much shorter than the interframe time Δt and for technical reasons (shutter speed, data transfer and writing), it cannot be reduced as much as desired. For this reason, CW PIV can only be used for low velocity flows.
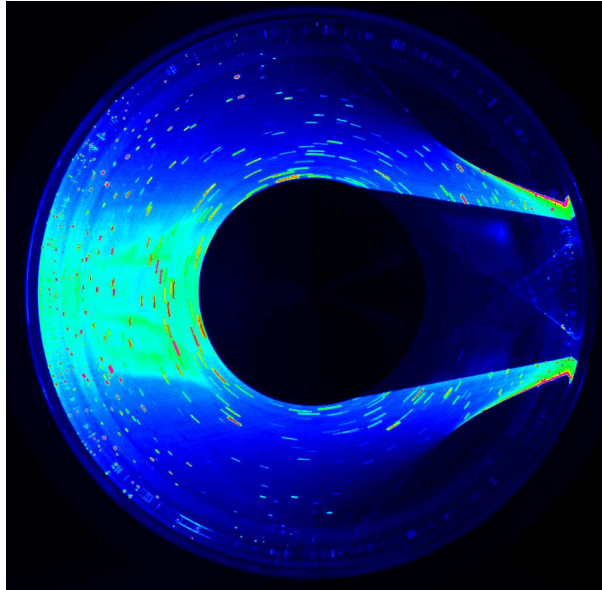
Figure 3.10: Single frame / Single exposure image in a Couette geometry.

Pulsed laser PIV is a way to extend the technique to high-speed flows. In that case, the effective exposure in images is conditioned by a light pulse fired by the laser. The rest of the time during exposure (hatched in figure 3.11) has no effect because there is no light entering the camera. The light pulses can be shifted to the end of the first image and to the beginning of the second to reduce Δt to a technical minimum, which is the camera interframe time between two images. This technique is called "frame straddling" acquisition technique. Specific cameras designed for PIV allows interframe times as short as 100 ns. Unfortunately it cannot be used for time-resolved PIV (TRPIV).

Tunable experimental parameters

In this final section on acquisition, the reader will find a short summary of the tunable parameter in PIV image acquisition:

- Particles

  – Concentration of seeding particles
  – Particle diameter
  – Particle type (material, coating, fluorescent dye, dye concentration, etc.)

- Laser and optics

  – Thickness and width of the light sheet
  – Light energy density
  – Time interval between exposure (in case of pulsed lasers)
  – light sheet overlap between the pulses (recombination optics of the two laser cavities)
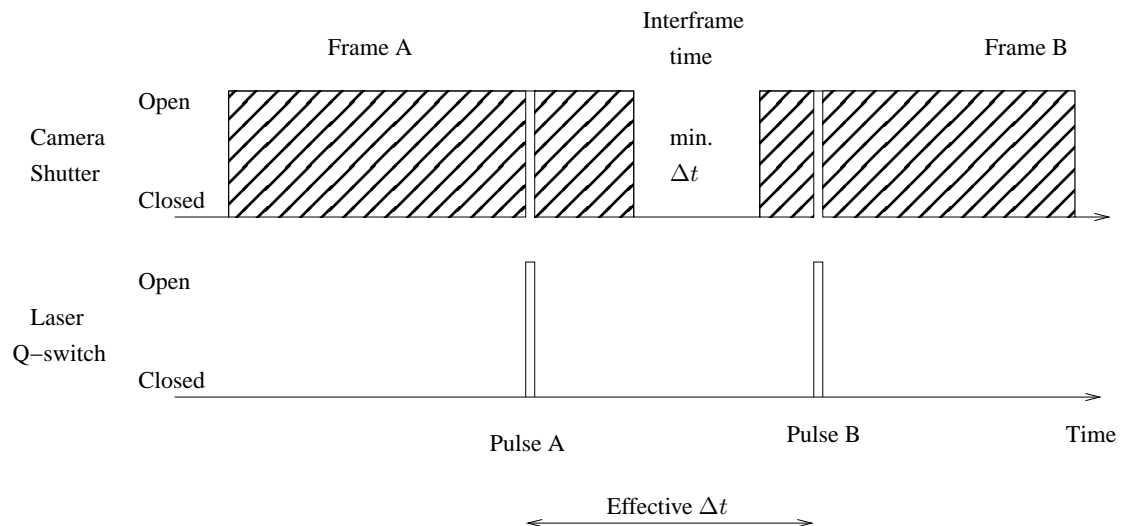
- Camera

Figure 3.11: Frame straddling technique used in pulsed PIV to follow high speed flows.

- – Time interval between exposure (in case of CW lasers)
- – Lens magnification **M**
- – f-number of the camera lens
- – Particle image diameter
- – Size and shape of the interrogation spots

3.3.5 PIV evaluation

Pre-processing: image restoration and enhancement

Image restoration attempts to "repair" undesirable effects due to imaging such as perspective distortion, image blur, etc. To optimize PIV, a dark uniform background is necessary. In some experiments, this is not trivial and sometimes impossible to achieve experimentally. A common way to deal with noisy background is to pre-process the images by subtracting a mean image calculated from several PIV images. Unfortunately, part of the information is lost in the process and it produces an increase in the discretization error (peak locking effect). For weak AOI enlightening, lots of particle are weakly visible. To enhance images, one can apply a nonlinear relation between intensity and pixel gray values. This is called as *histogram equalization*.

PIV image correlation

For the definition of image intensity field, auto- and cross-correlation and associated notation, please refer to Appendix B.

Autocorrelation technique for doubly exposed images   In the case of doubly exposed images, the image intensity I^+ is composed of the image intensity of two images I and I' separated by a time lapse

Δt:

$$I^+(\mathbf{X}, \boldsymbol{\Gamma}) = I(\mathbf{X}, \boldsymbol{\Gamma}) + I'(\mathbf{X}, \boldsymbol{\Gamma})$$
$$= \sum_{i=1}^{N} (V_0(\mathbf{X_i})\tau(\mathbf{X} - \mathbf{X_i}) + V_0(\mathbf{X_i} + \mathbf{D})\tau(\mathbf{X} - \mathbf{X_i} - \mathbf{D}))$$

It can be decomposed into five terms: $\qquad\qquad\qquad\qquad\qquad\qquad\qquad\qquad$ (3.3)

$$R_{I^+}(\mathbf{s}, \boldsymbol{\Gamma}, \mathbf{D}) = R_C(\mathbf{s}, \boldsymbol{\Gamma}) + R_F(\mathbf{s}, \boldsymbol{\Gamma}) + R_P(\mathbf{s}, \boldsymbol{\Gamma}, \mathbf{D})$$
$$+ R_{D+}(\mathbf{s}, \boldsymbol{\Gamma}, \mathbf{D})) + R_{D-}(\mathbf{s}, \boldsymbol{\Gamma}, \mathbf{D}) \qquad\qquad (3.4)$$

with $\mathbf{D}$ is the particle displacement, $\mathbf{s}$ the separation vector in the correlation plane, $\mathbf{X}_i$ is the i th particle position, $\boldsymbol{\Gamma}$ describes the state of the particle ensemble at a given time t, $V_0(\mathbf{X_i})$ is the transfer function giving the light energy of an individual particle i inside the interrogation volume V_I and its conversion into an electronic signal, $V_0(\mathbf{X_i}) = W_0(X, Y)I_0(Z)$, where I_0 is the intensity profile of the laser sheet (typically Gaussian or almost constant if the laser beam intensity profile is a top-hat beam) and $W_0(X, Y)$ is nonzero if the particle is inside of the laser sheet and zero otherwise and finally $\tau(\mathbf{X})$ is the intensity transmissivity point spread function of the photograph (commonly taken as Gaussian in the literature).

$R_C(\mathbf{s}, \boldsymbol{\Gamma})$ can be viewed as the convolution of the mean intensities, $R_F(\mathbf{s}, \boldsymbol{\Gamma})$ the fluctuating noise component, $R_P(\mathbf{s}, \boldsymbol{\Gamma})$ the self-correlating peak located at the origin of the correlation plane, $R_{D+}(\mathbf{s}, \boldsymbol{\Gamma})$ the displacement correlation peak, correlation of images of particles in exposure 1 with images of the same particles in exposure 2 and finally $R_{D-}(\mathbf{s}, \boldsymbol{\Gamma})$ the wrong displacement correlation peak, correlation of images of particles in exposure 2 with images of the same particles in exposure 1.

Cross-correlation of 2 singly exposed images In the case of several single exposed images, we have two image intensities I and I' separated by a time lapse Δt and hence by a displacement $\mathbf{D}$.

$$I(\mathbf{X}, \boldsymbol{\Gamma}) = \sum_{i=1}^{N} V_0(\mathbf{X_i})\tau(\mathbf{X} - \mathbf{X_i}) \text{ and } I'(\mathbf{X}, \boldsymbol{\Gamma}) = \sum_{j=1}^{N} V_0'(\mathbf{X_j})\tau(\mathbf{X} - \mathbf{X_j} - \mathbf{D})$$

$$R_I(\mathbf{s}, \boldsymbol{\Gamma}, \mathbf{D}) = \frac{1}{a_I} \sum_{i,j}^{N} V_0(\mathbf{X_i})V_0'(\mathbf{X_j} + \mathbf{D}) \underbrace{\int_{a_I} \tau(\mathbf{X} - \mathbf{X_i})\tau(\mathbf{X} - \mathbf{X_j} + \mathbf{s} - \mathbf{D})d\mathbf{X}}_{R_\tau(\mathbf{X_i} - \mathbf{X_j} + \mathbf{s} - \mathbf{D})}$$

$$= \underbrace{\frac{1}{a_I} \sum_{i \neq j}^{N} V_0(\mathbf{X_i})V_0'(\mathbf{X_j} + \mathbf{D})R_\tau(\mathbf{X_i} - \mathbf{X_j} + \mathbf{s} - \mathbf{D})}_{R_C(\mathbf{s}, \boldsymbol{\Gamma}) + R_F(\mathbf{s}, \boldsymbol{\Gamma})}$$

$$+ \underbrace{R_\tau(\mathbf{s} - \mathbf{D}) \sum_{i=1}^{N} V_0(\mathbf{X_i})V_0(\mathbf{X_i} + \mathbf{D})}_{R_D(\mathbf{s}, \boldsymbol{\Gamma})}$$

It can be decomposed into only three terms: $R_C(\mathbf{s}, \boldsymbol{\Gamma})$, $R_F(\mathbf{s}, \boldsymbol{\Gamma})$, and $R_D(\mathbf{s}, \boldsymbol{\Gamma})$. $R_C(\mathbf{s}, \boldsymbol{\Gamma})$ can be viewed as the convolution of the mean intensities, $R_F(\mathbf{s}, \boldsymbol{\Gamma})$ the fluctuating noise component from the $i \neq j$ terms, $R_D(\mathbf{s}, \boldsymbol{\Gamma})$ the displacement correlation peak, correlation of images of particles in exposure 1 with images of the same particles in exposure 2. It reaches a maximum for $\mathbf{s} = \mathbf{D}$.

3.3.6   Optimization of correlation

As we have seen in § 3.3.4, we can change several parameters in the acquisition step to enhance images for the correlation processing step.

- **Effect of time between two light pulses** Δt [7, 168]
  Increasing the time Δt between images reduce the relative error made on Δx (and also on Δt even if it is almost always assumed as free of error). In the same time it does reduce the signal-to-noise ratio (SNR) due to loss-of-pairs effects. On the other hand, with a vanishing pulse separation ($\Delta t \rightarrow 0$) there is no loss of pairs anymore but the small error made on the particle displacement becomes much more important. A trade off has to be found for the Δt because of the displacement range in the interesting part of the studied flow.

- **Effect of particle seeding**
  As shown by Keane *et al.* [149], if we want to have a valid detection probability of 90%, the sub-window particle density must be greater than 15 particles. Depending on the size of AOI and the laser sheet thickness, seeding concentration has to be adapted to get enough particles in the sub-windows.

- **Duration of the signal acquisition**
  In CW-laser PIV the camera shutter controls the duration of an image acquisition. If the flow motion is somewhere too fast compared to the shutter opening time, part of the image will be blurred. Finally the correlation peak in the fast flow region will be stretched in the flow direction, leading to worse SNR. As shown in figure 3.11 for pulsed laser PIV, the image is frozen by the laser pulse which is usually short enough to avoid any problems.

- **Effect of particle image diameter**
  An optimal particle image diameter exists in range of 1.5 to 3 pixel per particle depending on the recording technique.

- **Effect of laser power**
  By changing the laser light power, the effective laser sheet thickness and therefore the interrogation volume is accordingly modified. If both laser pulses have the same power, the same volume will be illuminated. Otherwise this leads to an increase of the out-of-plane loss-of-pairs and therefore to a worse SNR.

- **Misalignment of the two lasers combining optics**
  In most cases if the optics are misaligned, the out-of-plane loss of particles will increase and the signal to noise ratio (SNR) too. In some cases, if the velocity component orthogonal to the laser sheet is significant and relatively constant, we can misalign the combining optics voluntarily to reduce the out-of-plane loss of particle.

- **Effect of displacement gradient**
  As in PIV, the velocity measurement is based on the correlation of the displacement of a pattern in a sub-window, if the velocity gradient across the sub-window is significant, it results in a biased measured displacement.

- Correlation calculations
  PIV correlation maps can be either calculated directly in the spatial domain or through the frequency domain using FFTs. Direct calculation is computationally very expensive ($O[N^4]$, N

being the length of a sub-window). Using the frequency domain reduces the cost to $O[N^2 \log_2 N]$ operations. However care must be taken with aliasing effects, bias errors that arise with FFT techniques.

Advanced digital interrogation techniques

Over the years various, techniques were developed to enhance PIV correlation algorithms. We just mention here some of them: multi-pass schemes, offset schemes, multi-grid schemes, desampling, sub-pixel estimator (peak centroid, parabolic fit, gaussian peak fit).

3.3.7   Post-processing

The post-processing step in PIV consists of the validation of raw data, replacement or removal of spurious vectors, data reduction, and analysis of the data to have a physical insight into the flow motion.

3.3.8   Specific PIV techniques

Some derived techniques from PIV are listed in Table 3.3. Some of the techniques can be used simultaneously.

Table 3.3: Specific PIV techniques.

Defocusing PIV	It uses a mask with two or more apertures shifted away from the optical axis to obtain multiple images from each scattering source and allows to infer the third velocity component [141, 235, 236, 237]
Dual plane PIV	By using an additional light sheet parallel to the first one, one can estimate the out-of-plane velocity component by using three images at t, $t + \Delta t$, and $t + 2\Delta t$,
FPIV	This is a PIV technique that uses fluorescent particle instead of light scattering
μ-PIV	PIV in some micrometer scale flows where measurement volume is not defined by the laser sheet thickness but by the focal depth of the objective,
Stereo PIV	PIV using two cameras to measure the third velocity component perpendicular to the laser sheet
Super resolution PIV	This is a technique that combines successively PIV techniques for an estimate of the velocity as an input to particle tracking velocimetry (PTV) to measure the velocity of each individual particle
Time resolved PIV	In Time resolved PIV, all successive images can be used to measure an instantaneous velocity profile
Tomographic PIV	This is a PIV technique that uses four cameras to obtain the three velocity components in a volume.

3.4   Fluorescent particle image velocimetry

Contrary to classical PIV techniques, where tracers are added to the flow without disturbing fluid motion, it is not obvious that in concentrated particle suspensions adding a given amount of particles, even small compared to the coarse particles, does not disturb motion and, thereby, does not affect mixture rheology [17, 56, 186]. In this context, classic PIV techniques may become invasive and can be no longer suitable to studying concentrated suspensions.

To overcome this potential problem (which is a field of research in its own right), a strategy is to track the solid (disperse) phase directly. As we will see in § 4.2.7, fluid and particles are *refractive-index-matched* (RIM) so that the mixture becomes clear, which makes it possible to use optical visualization at the heart of fluid flow. In this way, particles in RIM fluid hardly scatter laser light, as can be seen in Fig. 3.12. To get a better idea of the difference between the techniques, let us compare the RIM-fluid technique with a classic PIV setup. With a viewing angle of $90\,°$, standard polystyrene tracers of $20\,\mu m$ in diameter in water (see Fig. 3.12 (a)) scatter at least $10'000$ times more (see Fig. 3.12 (d)) than particles in the refractive-index-matched (RIM) fluid (see Fig. 3.12 (c)). Note that for the RIM-fluid experiments used in this comparison, the refractive index (RI) mismatch was particularly high (close to 10^{-4}) as a result of defects in the measurement tools and our fluid preparation procedure, whcih means that the differences between PIV and RIM-fluid techniques are even more pronounced when the RI mismatch is optimized.

As light scattering cannot be used in RIM suspensions, we added a fluorescent dye (rhodamine 6G) to a fraction of the PMMA particles and used them as PIV tracers. Figure 3.13 sketches the FPIV measurement procedure. The laser light excites the dye on the tagged particles, the fluorescence of the dye is emitted isotropically. A high pass filter (see Fig. 3.14) in front of the camera blocks the eventually scattered and reflected laser light and allows only fluorescent light to enter the camera. This enhances the images, especially in the wall regions, and it improves the SNR.
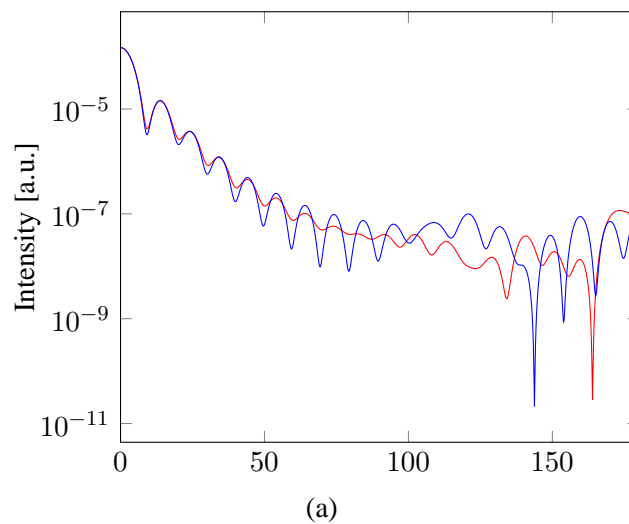

(a)

Figure 3.12: Calculated Lorentz-Mie small particle light scattering ($I_\perp$ in blue and $I_\parallel$ in red): (a) Classical polystyrene PIV tracers in water (particle diameter is $20\,\mu m$), (b) PMMA particles used in the present experiments in water ($200\,\mu m$), (c) PMMA particles used in the present experiments with the RIM fluid and with the largest uncertainty in the refractive-index-matching value, see § 4.2.7 (particle diameter is $200\,\mu m$) and (d) is the ratio of the values in (a) and the values in (c) between 80 and $100\,°$.
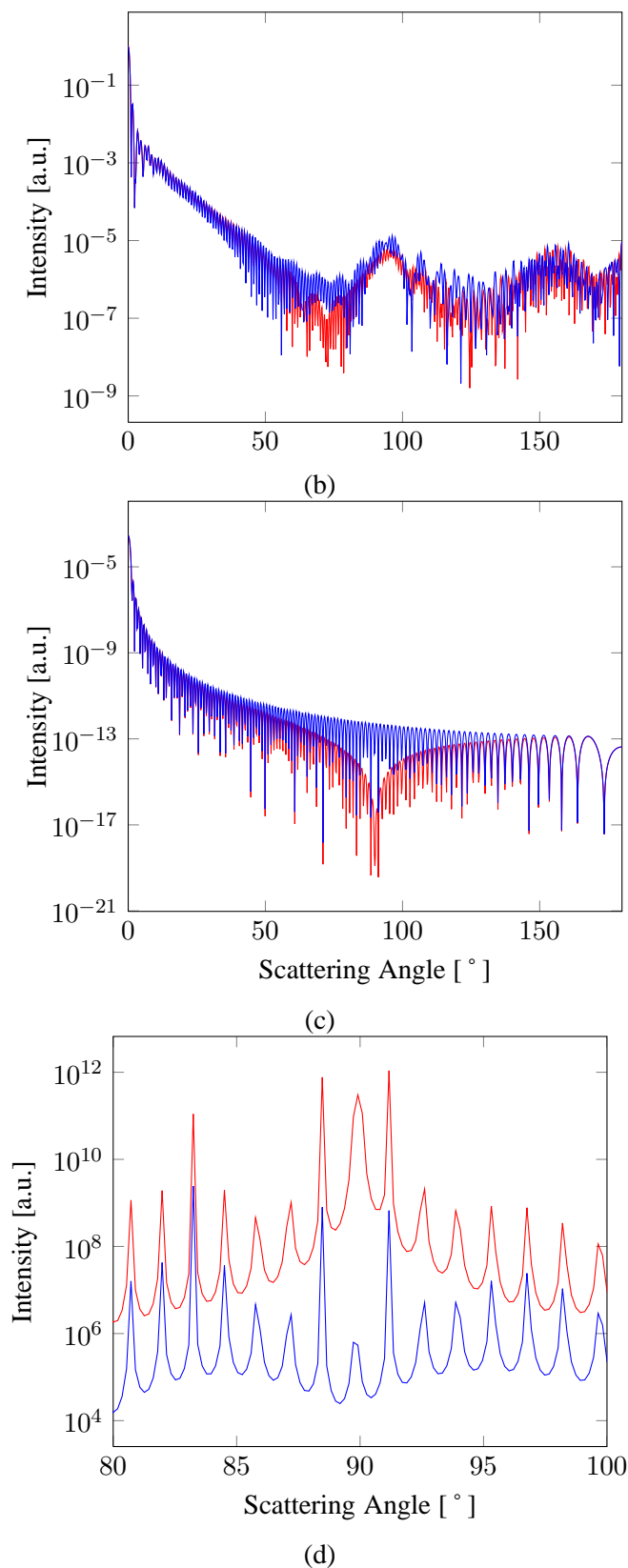
(b)

(c)

(d)

Figure 3.12: Calculated Lorentz-Mie small particle light scattering ($I_\perp$ in blue and $I_\parallel$ in red): (a) Classical polystyrene PIV tracers in water (particle diameter is 20 μm), (b) PMMA particles used in the present experiments in water (200 μm), (c) PMMA particles used in the present experiments with the RIM fluid and with the largest uncertainty in the refractive index matching value, see § 4.2.7 (particle diameter is 200 μm) and (d) is the ratio of the values in (a) and the values in (c) between 80 and 100 °.
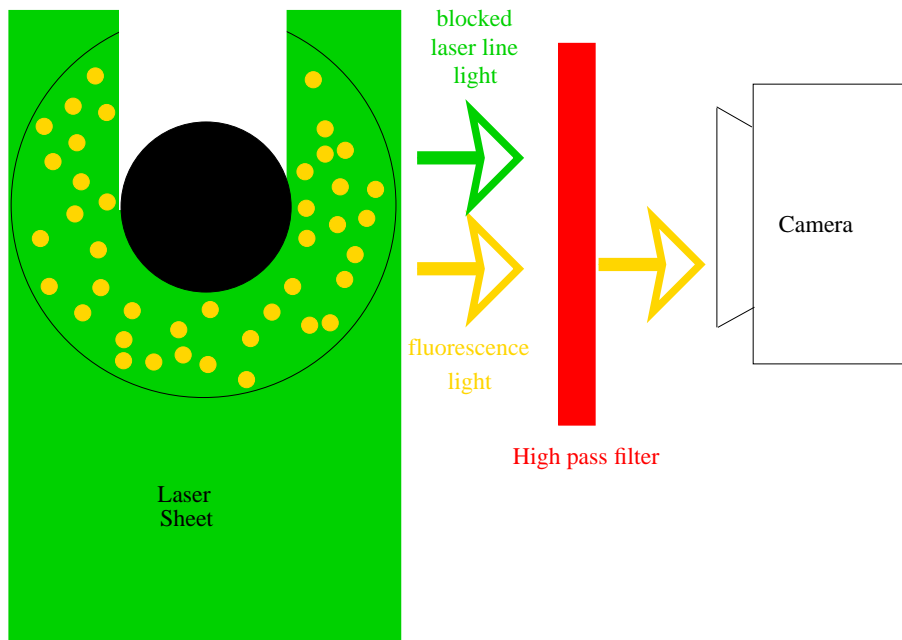
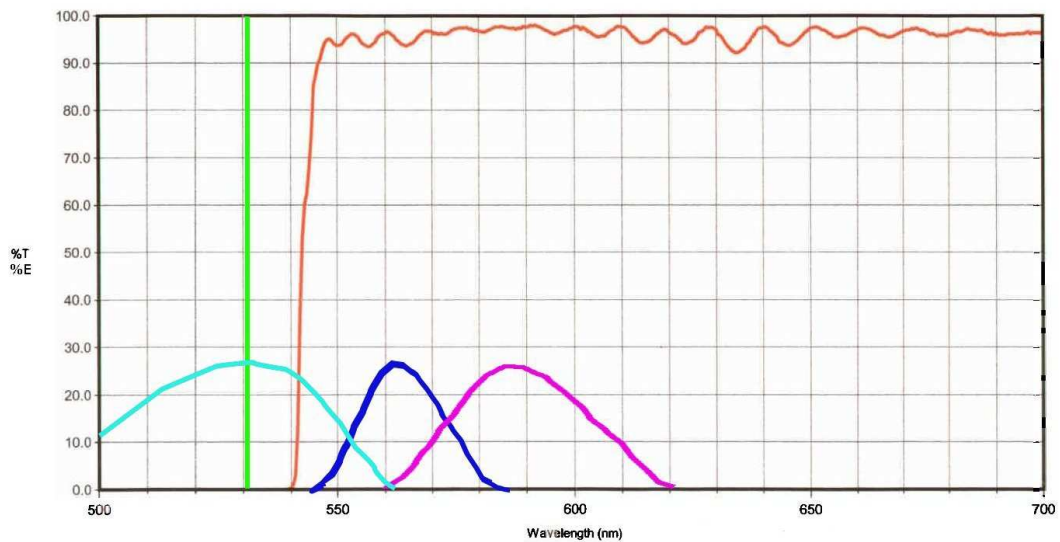Figure 3.13: Sketch of the FPIV procedure

Figure 3.14: Transmission curve of the sharp edge dielectric high-pass filter, green line is the laser line, red line is the filter transmission curve, cyan line is the rhodamine 6G absorption curve, blue line is the rhodamine 6G emission curve and the magenta line is the pyrromethene 597 emission curve.

3.5 Refractive index matching

3.5.1 Refractive index mixture rules

It is often desirable to determine the refractive index (RI) of a solute. This index can be estimated from the RIs of solution and solvent by using a suitable "mixture rule". There are several available methods in the literature (see for example Aminabhavi, Heller, Shindo or Tasic [10, 126, 272, 286] for an overview) All theoretically derived rules are based upon the electromagnetic theory of light and can apply only if there is no change of volume during the mixing:

Lorentz-Lorenz equation (theoretical) [180] :

$$\frac{(n_{12} - 1)}{(n_{12}^2 + 2)\rho_{12}} = \left(\frac{n_1^2 - 1}{n_1^2 + 2}\right)\frac{p_1}{\rho_1} + \left(\frac{n_2^2 - 1}{n_2^2 + 2}\right)\frac{p_2}{\rho_2} \tag{3.5}$$

Wiener equation (theoretical) [308] :

$$\frac{n_{12}^2 - n_1^2}{n_{12}^2 + 2n_1^2} = \phi_2 \frac{n_2^2 - n_1^2}{n_2^2 + 2n_1^2} \tag{3.6}$$

Heller equation (theoretical) [125] :

$$\frac{n_{12} - n_1}{n_1} = \frac{3}{2}\left(\frac{m^2 - 1}{m^2 + 2}\right), m = \frac{n_2}{n_1} \tag{3.7}$$

Dale-Gladstone equation (theoretical) [79, 80] :

$$\frac{n_{12} - 1}{\rho_{12}} = \frac{n_1 - 1}{\rho_1}p_1 + \frac{n_2 - 1}{\rho_2}p_2 \tag{3.8}$$

Arago-Biot equation (empirical) [18] :

$$n_{12} = \phi_1 n_1 + \phi_2 n_2 \tag{3.9}$$

Lichtenecker equation (empirical) [125] :

$$log(n_{12}) = \phi_1 log(n_1) + \phi_2 log(n_2) \tag{3.10}$$

Newton equation (theoretical) :

$$n_{12}^2 = \phi_1 n_1^2 + \phi_2 n_2^2 \tag{3.11}$$

3.5.2 Small particle index matching methods

As far as we know, there is no method to measure directly the RI of small particles accurately and conveniently. Thus, it is not possible to measure the RI of particles first and then adjust the RI of the interstitial fluid by changing it's composition so that it has the same RI. Therefore one has to measure it indirectly. There are two main types of methods to obtain the RI:

- By using a bulk solid sample and measuring the reflection/refraction of a light beam.

- By measuring transmitted light through a suspension sample by varying either the sample temperature or the light wavelength. Using this method requires to have good knowledge of the particle RI because it allows precise matching over a very limited range of refractive indices only.

For the second type of methods, all variants use the Christiansen effect:

"It is based on the various dispersions of two different media. A Christiansen filter is a narrow band-pass optical filter which consists of an optical cell which is stuffed with a crushed substance (i.e. here PMMA particles) and a liquid. The liquid is chosen according to the substance, so that the dispersion

curves coincide at one wavelength. For this wavelength the filled optical cell behaves like a plane-parallel, homogeneous disk and allows transmission. All other wavelength ranges of the spectrum are reflected, scattered as well as refracted at the many interfaces between substance and liquid. A change of the transmission behavior of this dispersion filter can be achieved by variation of the liquid, the temperature or variation of the pressure. The fundamental consequence is the change of the refractive index of the liquid." [1]

The bulk sample–laser method

Nouri *et al.* [223] proposed an ingenious way of matching the RI of their particles and the interstitial fluid. They shined a laser beam into a solution containing a large rod made up of the same material as the particles. By varying the composition of the solution (thus varying its RI), the laser beam passed through the system with different degrees of deflection depending on the mismatch between the rod and the fluid. The point of perfect match was attained when the beam passed through the system without any deflection. A variant of this technique consists to monitor the backward reflection of light on the immersed solid sample.

$$R = [(1 - n_l/n_s)/(1 + n_l/n_s)]^2 \qquad (3.12)$$

where R is the ratio of reflected beam power to incident beam power.
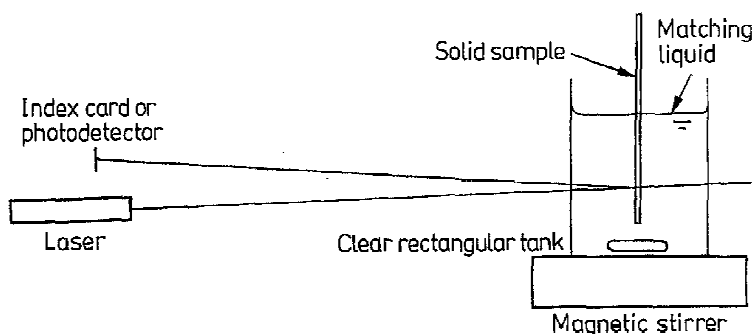

Figure 3.15: The backward reflection method (after [45]).

Figure 3.15 illustrates the apparatus to perform RI tuning based on equation (3.12). First, solution components must be chosen such that it is possible to obtain the RI of the solid with a mixture of them. Next, a flat sample of the solid material with one polished surface is held in a stirred tank of the liquid mixture. The sample is held so that reflected beam is just a few degrees away from backward reflection. The reflected beam is projected onto a photodetector. Finally, match is achieved by varying the component ratio of the liquid mixture until the reflected beam intensity attains a minimum.

To use this method, one needs to possess a bulk sample made up of the same material as the particles and has to be sure that the RI of the bulk sample has not been modified during the manufacturing process.

The bulk sample–refractometer method

Most refractometers can also be used to measure the RI of a solid. A small sample of the solid with one flat polished surface is placed in optical contact with the refractometer prism. Optical contact is

---

1. after http://en.wikipedia.org/wiki/Christiansen_effect

established by filling the gap between the prism and the sample with a liquid. The index of refraction of the fluid n_f must be below that of the prism n_{prism} and above that of the unknown sample n_{sample}.

$$n_{sample} < n_f < n_{prism}$$

A gem (or jeweler's) refractometer can also be used to measure the RI of a solid. Refractometry of solids is described at length in Sinkankas and Hurlburt [134, 277]. To use this method, we must have a bulk sample of the same material used for the particles.

The wavelength method

As a result of the differences in optical dispersion of each phase, the refractive indices can be matched for only one wavelength. Light with a different wavelength is refracted at the solid-liquid interfaces, with the angle of refraction growing with distance from the matching wavelength (Christiansen effect, [64, 65]). As shown in Fig. 3.16 this phenomenon results in a transmittance curve with a maximum at the matched wavelength. Once this curve has been measured, one can deduce the RI of the particles by mesuring the RI of the fluid at the wavelength corresponding to the maximum of transmittance using a spectrophotometer. During this experiment, care must be brought keeping the temperature constant because it does also vary the RI of the components. This method is described in details in Stöhr [282].
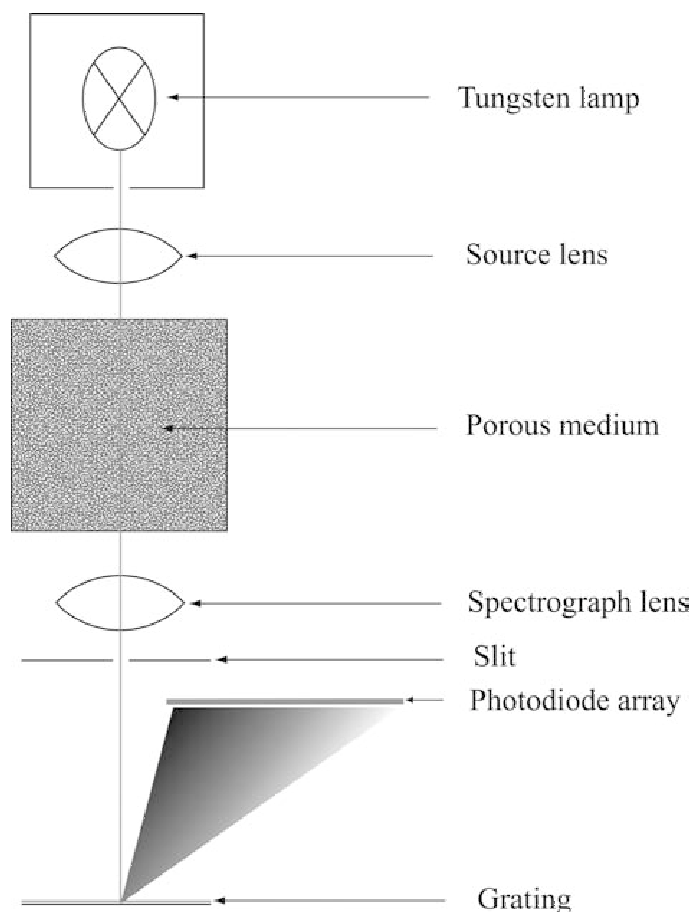

Figure 3.16: The wavelength method (after [282]).

The temperature method

Since the RI of the liquid phase and the solid phase depend differently from temperature, we can match the RI only for a given temperature. As shown on Fig. 3.17, shining a laser beam through a temperature-controlled suspension sample and recording the transmitted light results in a curve with a maximum at the matched temperature. We have finally to measure the RI of the fluid at that temperature to obtain the RI of the beads.
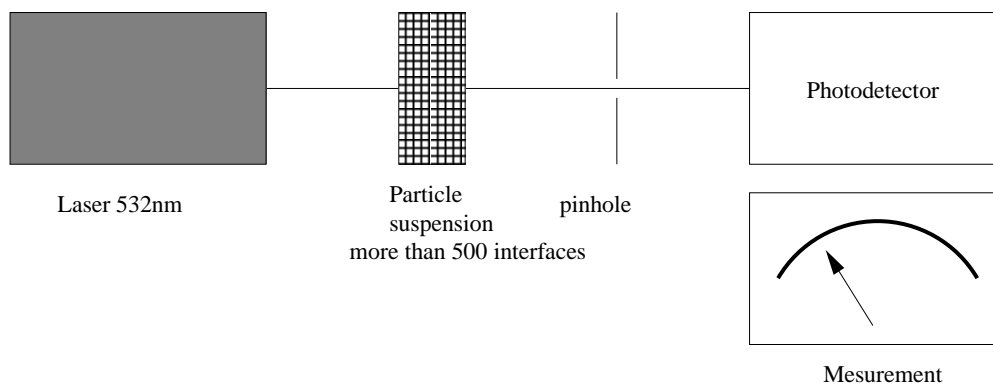

Figure 3.17: The temperature method (after [154, 155]).

3.5.3   Index-matching material for concentrated particle suspensions

The packing dictates the choice of interstitial fluid. It must be transparent, which reduces choice to plastics, glasses, and certain synthetic rubbers. Nylon, PC, PEEK, PET, PS, PVC, SAN and glasses are almost excluded because they exhibit too high refractive indices (RI from 1.48 to 1.60). They are discarded since their use would require liquids with refractive indices above 1.580. Indeed, such substances are rare and most of them are toxic. Some examples are Aniline (n=1.586), Bromoform ($n = 1.590$), Iodobenzene ($n = 1.620$), Quinoline ($n = 1.620$) and Carbon disulfide ($n = 1.625$). Some interesting candidates are simply too expensive. There are many plastics (RI from 1.37-1.60) which are transparent when free of fillers or other impurities provided that they are in the amorphous state or have a crystalline structure smaller than the wavelength of the light incident upon the plastic. Among synthetic rubbers only silicone rubber ($n = 1.42$) is transparent. Only one plastic, polymethylmethacrylate ($n = 1.49$) is normally manufactured industrially in the transparent (amorphous) form. However crystalline polymers may be rendered transparent by heating above the "melting temperature", where there is a transition to the amorphous state, followed by rapid quenching to room temperature. The plastics listed in the following table have refractive indices lower than 1.49 in the amorphous state.

Table 3.4: RI matching possible candidates.

	RI	Melting temperature [˚C]
Fluorinated ethylene-propylene (FEP)	1.34	340
Fused quartz	1.458	1650
Glass	1.47 to 1.65	500 to 1100
Polychlorotrlfluoroethylene (PCTFE)	1.435	216
Polyformaldehyde (POM)	1.41	175-180
Polymethylmethacrylate (PMMA)	1.49	130-140
Polysiloxanes(Silicone rubber)	1.40	300
Polytetrafluoroethylene (PTFE)	1.38	327
Polyvinylacetate (PVA)	1.466	230
Silica gel	1.472	1610
Tetrafluoroethylene (TFE)	1.34	-

Table 3.5: RI matching possible candidates with high-index fluids.

	RI	Melt temperature [˚C]
Nylon 6,6	1.565	255
Polycarbonate (PC)	1.586	267
Polyetheretherketone (PEEK)	1.65-1.77	334
Polyethyleneterephthalate (PET)	1.575	68
Polystyrene (PS)	1.59	100
Polyvinylchloride (PVC)	1.54	80
Styrene/acrylonitrile copolymer (SAN)	1.57	100

4 Facility and experimental procedure

4.1 Rheo-optical facility

4.1.1 Overview of the experimental setup

The basic components of the TSI PIV system used here are the PIV camera, frame grabber, camera-laser synchronizer, and the acquisition software. Combined to the TSI system, a Quantel CFR 200 is used for enlightening. A homemade laser sheet generator was built with a set of one spherical and three cylindrical lenses. For the rheometrical part, a Bohlin Gemini 200 from Malvern Instruments is used with a clear quartz cell for visualization. The rheometer is mounted on a vertical linear stage, which allows us to measure optically the flow at various levels in the Couette cell.

The camera is a Powerview Plus 2 Mpixel (1600×1200), model 630057. The maximum frame rate is 32 Hz at full resolution. It can be increased at reduced resolution. The dynamic range is 12 bit and the minimum frame straddling time is of 200 ns. Combined to the camera and for calibration purpose, we use a telecentric lens from Opto-Engineering, model TC 4M 48 with a fixed magnification factor of 0.368 and accordingly a fixed AOI of 32.2×24.2 mm with our CCD captor. The depth-of-view is 7 mm and the working distance is 134.6 mm. A dielectric filter commercialized by L.O.T. Oriel (LOT-Oriel GmbH & Co. KG), model CH-RS532-50 is used in front of the CCD. It rejects the 532 nm laser light for the FPIV. It is a sharp edge high-pass filter with transmission band starting at 538.4 nm (see Fig. 3.14 for the transmission curve).

The frame grabber is a Coreco X64-CL Full frame grabber from Dalsa Corporation.

The Delay generator for synchronization of the experiment is the LaserPulse Synchronizer Model 610034 manufactured by Berkeley Nucleonics Corporation for TSI. It has one input trigger and 6 output triggers for camera, laser and other equipment that need to be synchronized. Four of them are used to trigger the flashlamps and Q-switch of the laser. It allows to control the time interval between exposure and in the mean time to tune the pulse energy of both cavities. The fifth output triggers the camera acquisition. The last output trigger remains free for a future synchronization with the rheometer.

The Quantel CFR 200 is a water cooled laser with two optical cavities at 2×30 Hz. It is a doubled Nd:YAG laser working at 532 nm and with a beam energy up to 180 mJ per pulse at 30 Hz.

The laser sheet is composed of four lenses following Diemunsch (1987) and Prenel (1998) [89, 247]. It allows a precise independent control of the sheet thickness, beam waist position, sheet width, and lateral spreading.

The Couette cell is a cup made up of two glued quartz parts, a 60 mm inner diameter hollow cylinder and a flat circular bottom plate. Its design will be presented in more detail in section 4.1.3.

The rheometer is mounted on a vertically movable table with a stroke of 100 mm thanks to a linear stage manufactured by SKF (SKF Linear Motion and Precision Technologies), model RSK 150.410.100.-AR2. The linear stage is adjusted vertically with an uncertainty of $0.02\,°$ in both angular directions. The

maximal horizontal displacement generated is of order of 30 μm over the whole stroke. By taking two images with the camera looking at the Couette cell from the bottom, we were unable to see any horizontal shift. This means that the precision of the adjustment was below 20 μm because of the CCD pixel size and the zoom used. The rheometer can be moved back and forth on 70 mm on the table to allow homogeneous illumination of the whole Couette cell and measurement on either sides of the inner cylinder or vane. The reproducibility for the vertical positioning of the movable table is of 10 μm. This very fine adjustability of the Couette cell positioning allows us to make measurement at different heights during a rheometrical experiment and considerably simplify the calibration process as we will see in § 4.5.2.
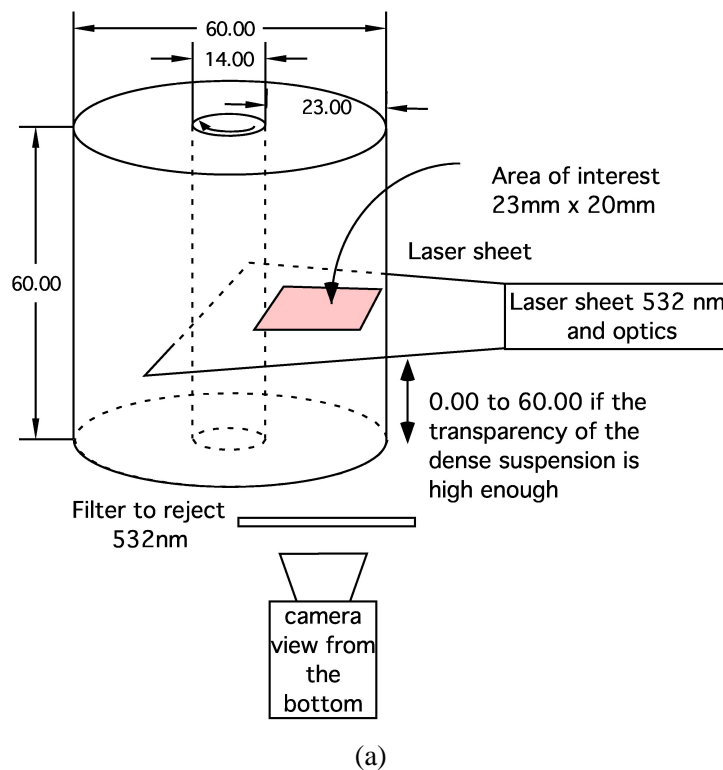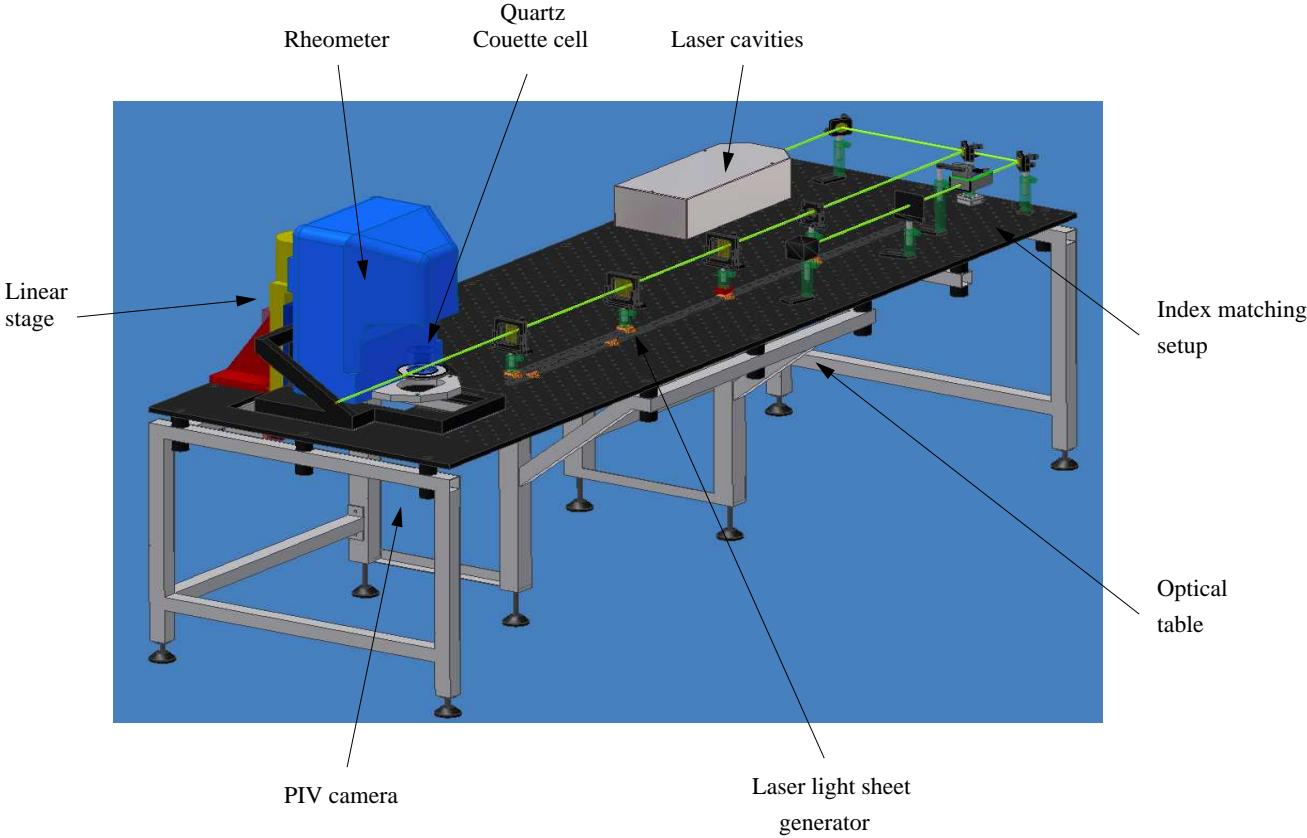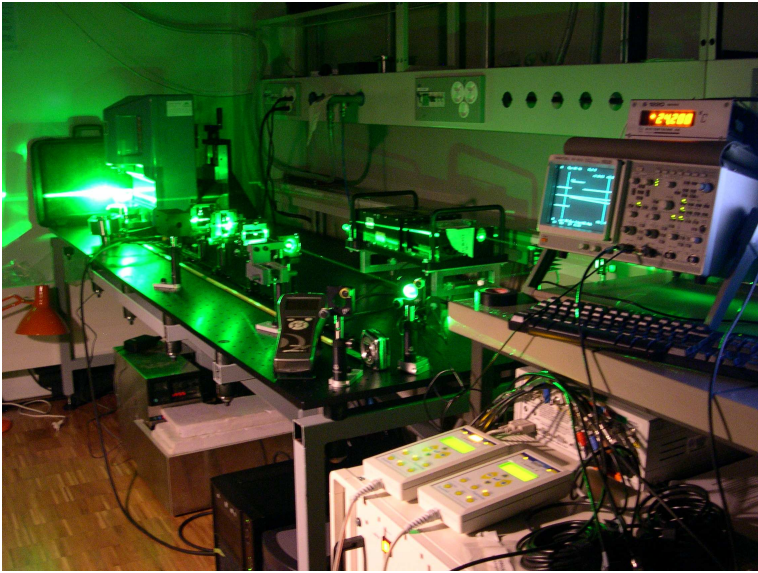

(a)

Figure 4.1: (a) Scheme of AOI and Couette cell imaging system, (b) Scheme of the rheo-optical facility (c) Picture of the rheo-optical facility.

(b)

(c)

Figure 4.1: (a) Scheme of AOI and Couette cell imaging system, (b) Scheme of the rheo-optical facility (c) Picture of the rheo-optical facility.

4.1.2   Temperature-controlled chamber

As we have seen in § 3.5, the Christiansen effect induces a change from a turbid suspension to a clear suspension by changing the temperature, pressure or light wavelength. In our case the pressure and the wavelength (laser line and near fluorescence) are almost constant. The temperature must be as constant as possible. The performance of temperature control will strongly affect our ability to carry out measurement deep into the suspension. To achieve this, an insulated chamber connected to a thermal water bath (*Julabo KTB 30*) was built around the Couette cell. Figure 4.2 shows temperature fluctuations in the chamber. We were able to control temperature within $0.05\,^{\circ}$C keeping buoyancy and turbidity effects negligible for the duration of the experiments.
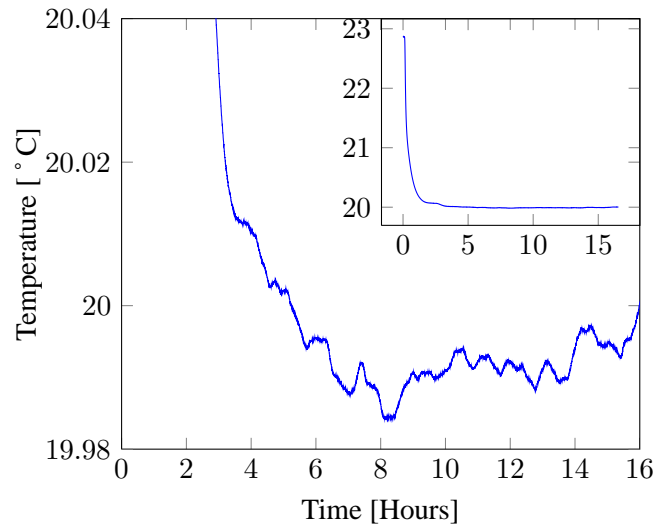

Figure 4.2: Example of temperature control of the chamber around the Couette cell, the main figure shows the temperature fluctuations around $20\,^{\circ}$C and the insert shows to whole temperature range starting from the room temperature at $23\,^{\circ}$C.

4.1.3   Couette flow Cell

The Couette cell dimensions must be chosen such that the ratio R/d is sufficiently large to contain enough particles across the gap to avoid finite size effects so that the measured properties would be independent of the gap width-to-particle ratio. This means that the concentric cylinder radius ratio $\kappa = R_{in}/R_{out}$ departs from 1. Therefore, as explained in § 3.2, standard methods for solving the Couette inverse problem fail and more sophisticated techniques must be used. It is not clear how well these methods perform when studying coarse-grain concentrated suspensions. The gap width must also be kept small enough in order to minimize vertical-end effects.

The Couette cell used for the FPIV measurement is a quartz cup manufactured by *EPOND S.A., Vevey*. The cell has an outer diameter of 60 ± 0.01 mm and a height of 60 ± 0.1 mm. The side and the bottom of the cell are transparent and can be used for laser shining and camera visualization. The cell was mounted on a *Gemini CVOR 200* commercial rheometer manufactured by *Malvern Instruments Ltd*.

Several stainless steel or titanium inner cylinders or inner 6-blade vanes with different radii ($\varnothing$ 8.75 to 27 mm) were used with the quartz cell. To reduce wall slip, the inner cylinder was roughened either by sandblasting or by gluing sandpaper on it. The gap width of at least 30 particle diameters is above

the empirical threshold of about 15 particles that allows us to consider the suspension as a continuum. The inner geometry bottom-end was conical to have an almost continuous shear rate transition from the Couette flow to the cone-plate flow near the bottom. The main drawback of this bob tip was the necessity to take into account bottom-end effect on the torque measurement. We preferred this kind of bottom-end for the inner geometry over others since it had a smaller influence on torque measurement and avoided a low shear-rate region where particle would migrate, as observed in the experiments of Leighton and Acrivos [169, 170] and Chow *et al.* [63].

The inner geometry alignment with the quartz Couette cell was controlled before each suspension loading so as to ensure a relative eccentricity e_r below 1% in the worst case, with $e_r = e/(R_{out} - R_{in})$ and where e is the distance between the inner and outer cylinder axes. Therefore the effect due to eccentricity with a Newtonian fluid on the torque measurement remains below 0.2 % [123, 135, 194].

4.2 Materials

4.2.1 Particle description

The particles selected were copolymer of polymethylmethacrylate ethylacrylate (PMMA EA) particles, manufactured by ARKEMA. In order to ensure a suspension that is as monodisperse as possible, we used only the particles in the size range 180 to 200 µm following the wet sieving procedure explained in § 4.2.5. For the polydisperse experiments, we used unsieved particles supplied by Altuglas (see Fig. 4.6). We chose particles in this size range for three reasons. First, these particles had the greatest clarity in the laser transmission experiments we performed. Second, they had also quite good sphericity and they were in the peak of the particle size distribution of the raw material. Third, being produced industrially, these particles are relatively inexpensive. The particles used in the experiment came from a single lot.

4.2.2 Fluid Description

To match the refractive index (RI) and the density of the particles at the same time, we had to use a mixture with at least three components. The fluid mixture composition is based on a recipe used, and subsequently fully characterized, by Lyon [181, 182]. We adapted it to our particles. A non-exhaustive list of refractive index matching fluid recipes used in the literature can be found in appendix A.

The particle density and refractive index were matched by a fluid mixture with mass fractions of about 50% Triton X100, 28% DBH, and 22% UCON oil. Each of these components provides a different feature of the mixture. Triton X100 has high refractive index, DBH has high density and by using different UCON oils, we can adapt the fluid viscosity in a relatively wide range. This last property of the UCON oil family was not used during the present study. The final mixture density is 1.184 ± 0.0005 g/cc, the refractive index at 532 nm and 20 ˚C is 1.48847 ± 0.0001 and its viscosity is 0.124 ± 0.0025 Pa·s at 20 ˚C. For the matching procedure, please refer to § 4.2.6 and § 4.2.7.

4.2.3 Fluid viscosities

In the temperature range between 15 and 25 degrees, the fluid viscosities of Triton X-100 and UCON oil 75-H450 decrease almost linearly with increasing temperature. With the largest available Couette geometry in our laboratory, we performed the 1,6 dibromohexane viscosity measurement near the lower torque limit of our rheometer (10^{-6} Nm). Therefore, the results (see appendix C) were relatively noisy and we were not able to measure the viscosity decrease with temperature. We could only deduce an upper bound. If suitable, the viscosity measurement was performed with two Couette geometries and also with

a cone-plate (CP) geometry. The viscosities varies as follows with temperature (see also Fig. 4.3 and the raw measurements in appendix C):

$$\eta_{X100}(T) = 0.9856 - 0.0280\,T$$
$$\eta_{UCON}(T) = 0.5645 - 0.0143\,T$$
$$\eta_{DBH}(T) \cong 0.009 - 0.0002\,T$$
$$\eta_{Trimix}(T) = 0.2840 - 0.0080\,T$$

From this linear interpolation viscosity gradient with temperature in the 15 to 25 °C range and the temperature fluctuation of 0.05 °C in the temperature-controlled chamber during an experiment (see § 4.1.2), we can conclude that temperature effects can be neglected in the experiment. Furthermore, temperature measurements within concentrated suspensions were performed during shearing and no notable temperature change was noticed in the studied regimes.
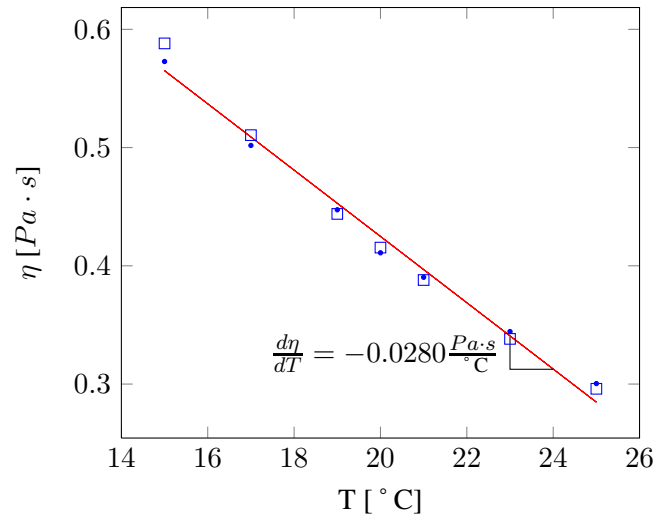
(a)

Figure 4.3: Dynamic viscosity of: (a) Triton X100, (b) UCON oil 75-H-450:
closed circles are cone-plate (CP) measurement ($\varnothing$ 40 mm and 4°) and open squares are bottom end corrected concentric cylinder measurements (inner and outer $\varnothing$ of 33–37 mm and 25–27.5 mm respectively).

(b)

Figure 4.3: Dynamic viscosity of: (a) Triton X100, (b) UCON oil 75-H-450:
closed circles are cone-plate (CP) measurement ($\varnothing$ 40 mm and 4°) and open squares are bottom end corrected concentric cylinder measurements (inner and outer $\varnothing$ of 33–37 mm and 25–27.5 mm respectively).
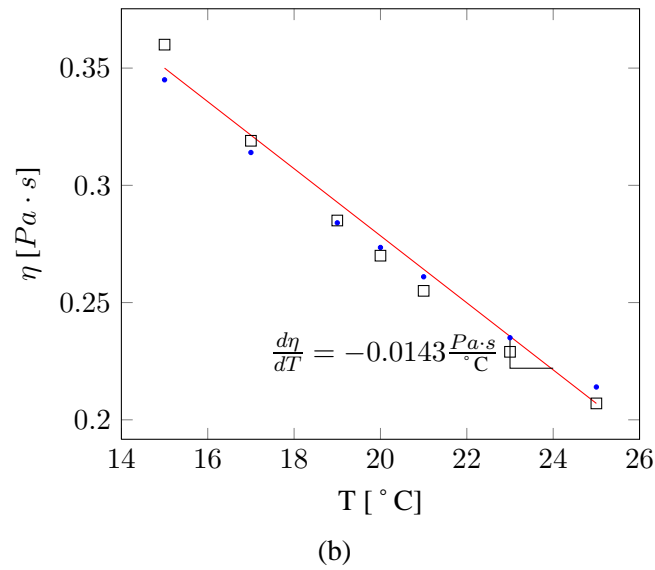

(c)

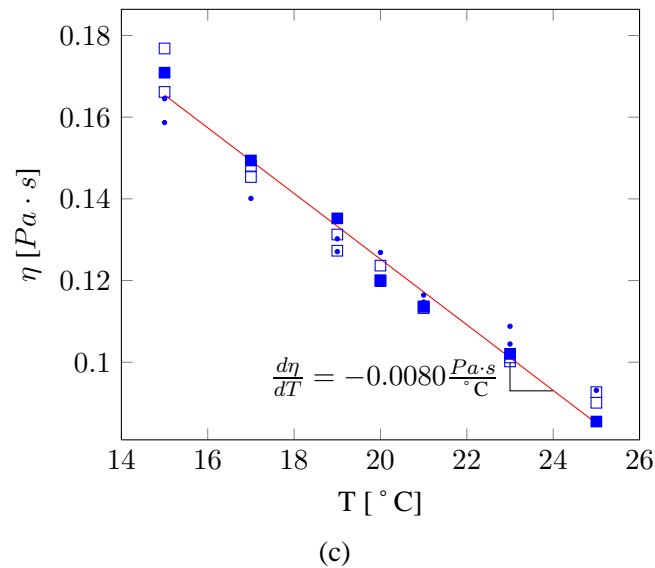Figure 4.4: Raw viscosity measurement at various temperature of the ternary mixture of Triton X-100, UCON oil 75-H450 and 1,6 dibromohexane:
closed circles are cone-plate (CP) measurement ($\varnothing$ 40 mm and 4°) and open squares are bottom end corrected concentric cylinder measurements inner and outer $\varnothing$ of 33–37 mm (open squares) and 25–27.5 mm (filled squares) respectively.

4.2.4   Important dimensionless numbers

From the particle properties, fluid properties and the Couette cell dimensions several relevant dimensionless numbers can be computed. The particle Reynolds number

$$Re_p = \frac{\rho r_p^2 \dot{\gamma}_{max}}{\eta_f} \cong 10^{-4}$$

is small enough for particle inertia to be neglected.
The Péclet number

$$Pe = \frac{6\pi \eta_f r_p^3 \dot{\gamma}_{min}}{kT} \cong 10^7$$

is high enough for Brownian motion and colloidal forces to be neglected.
The overall flow Reynolds number

$$Re = \frac{\rho U (R_{out} - R_{in})}{\eta} \cong 10^{-5} \text{ to } 2.5 \cdot 10^{-3}$$

depending on the gap, the velocity and the solid fraction in the suspension is small.
The Taylor number, which indicates whether a Couette inertial instability occurs,

$$Ta = 2 \left(\frac{U(R_{out} - R_{in})\rho}{\eta} \right)^2 \frac{(R_{out} - R_{in})}{R_{in}}$$

remains always below 6 for the most dilute suspension at the maximal rotation speed. This value is far below the critical value of ~ 3400 for the onset of Taylor secondary flow for Newtonian fluids.

4.2.5   Sieving procedure

For the monodisperse or quasi-monodisperse experiments, the PMMA particles were sieved using a Retsch AS200 Control (*Retsch GmbH*) sieving machine and a 180 µm and 200 µm sealed sieving stack. Several sieving procedure were tested (dry sieving, wet sieving, etc.). We finally modified the sieving stack column to perform the sieving in a recirculating flow of ethanol. In this way, we obtained reproducible size distribution and we got rid of surface tension effects (water) and electrostatic effects (dry sieving). Figure 4.6 shows a comparison between the raw material and the sieved size distribution.
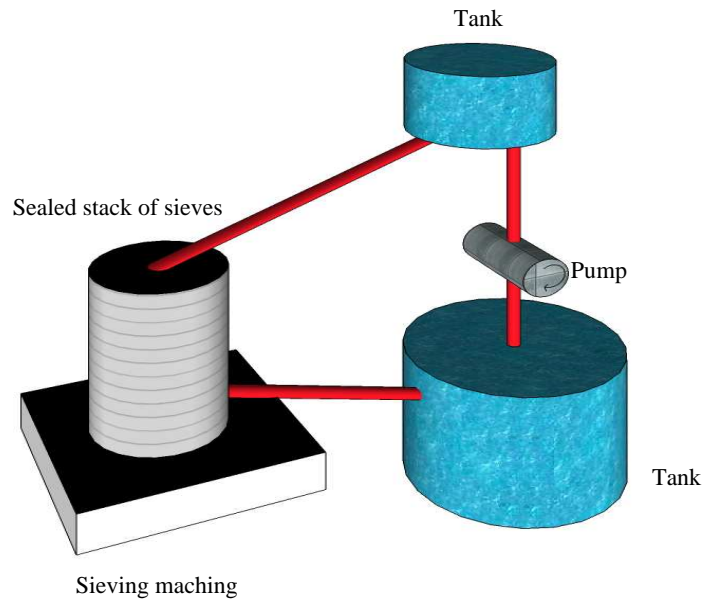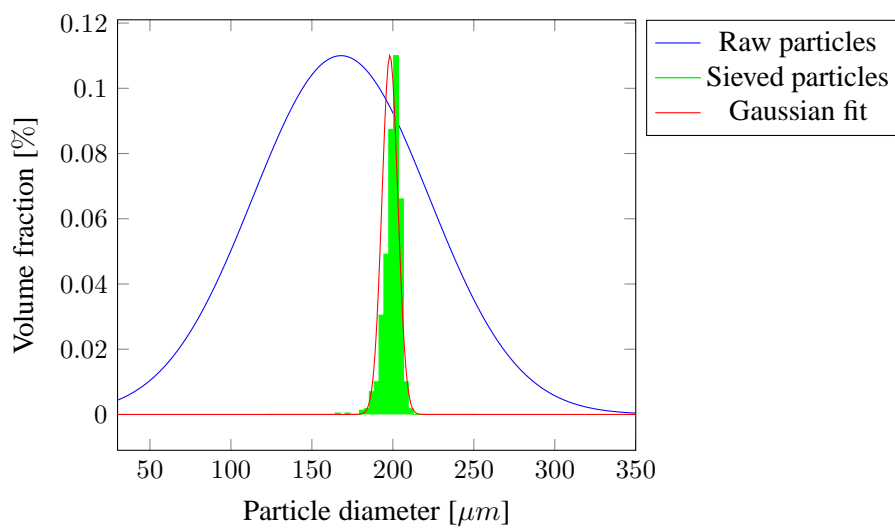
Figure 4.5: Sketch of the wet sieving setup.

Figure 4.6: Raw (blue, mean= $168\mu m$, s.d.= 54 µm) and sieved (red) particle size distribution, Gaussian fit of the sieved particle distribution with a mean of 199.1 µm and a standard deviation of 5.1 µm

4.2.6 Density matching procedure

The most difficult part when matching the fluid and particle densities was to measure the particle density. We did not have a density gradient column available [44, 70, 228, 296, 297, 298], so our matching method involved mixing many different fluids with a range of densities close to the PMMA datasheet values and observing the time it took for the particles to rise or sink. The mixtures where the particles remained in suspension the longest gave an estimate of the particle density. The densities of the fluid

mixtures were estimated as the average of the component densities weighted by the volume fractions of the components in the mixture. When a mixture was prepared in this way on the basis of the datasheet's densities of the fluids, a measure of the true mixture density was performed with a high precision aerometer (GECO-GERING, 0209 Aerometer DIN 12791 Serie L50, without Therm., Kl."H", precision of $5 \cdot 10^{-4}$ g/cc) in a temperature-controlled column at $20\,°C$ because of the density variation of the fluid with temperature (see for example Fig. 4.7).

We prepared fluids with densities ranging from 1.1800 to 1.1865 g/cc by steps of $5 \cdot 10^{-4}$ g/cc. Because of the possible small variations of particle density, we prepared particle-suspension samples with a solid fraction of 0.3 in sealed small bottles with a fluid height of 3 cm (i.e. on the same order or magnitude as the Couette cell of our experiments). Using a suspension of particles allowed us to infer the mean particle density, but because of the Boycott effect and of the reduced sedimentation velocity in "dense" (typically $\phi > \sim 0.2$) suspensions, the effective sedimentation velocity was lower than the single particle velocity at low Reynolds number:

$$V_\infty = \frac{1}{18} \frac{(\rho_p - \rho_f)g D_p^2}{\eta}$$

In an ideal geometry, the theoretical velocity of a suspension is:

$$V_{sedim} = V_\infty (1 - 6.55\phi)$$

This expression was deduced by a development at the first order of the sedimentation velocity at concentration ϕ, taking into account two-particle interactions. In practice this velocity will depend on the container. For example in a spherical vessel, this velocity becomes:

$$V_{sedim} = V_\infty (1 - 3.55\phi)$$

It was therefore not possible to calculate *a posteriori* the density mismatch from the sedimentation velocity. We could, however, obtain an upper bound (the terminal velocity of a single particle). The bottles were immersed in a thermal bath ($20 \pm 0.05\,°C$) for one week. A periodic observation of the particle sedimentation (rise or sink) of the particles was performed. In the best matched fluid, we could not see any sedimentation effect after this one-week experiment. Taking a fluid sedimentation of 1 cm/week (this is faster than what we could see) and calculating with the single particle terminal velocity, we can infer that the density mismatch must be below 10^{-4} g/cc. This value being below the uncertainties due to our capability to measure the fluid density ($5 \cdot 10^{-4}$ g/cc) added up with the effects due to the uncertainties in the control of temperature ($\pm 0.05\,°C$). As the Couette cell and the sedimentation vessel have dimensions of the same order of magnitude, we concluded from this experiment that we could perform experiments for a few days without sedimentation effects. Figure 4.7 shows the particle-suspension-sedimentation experiment after one week. The final density of the matching mixture was $1.1840 \pm 5 \cdot 10^{-4}$ g/cc, where the uncertainty resulted from various processes (e.g., the density fluctuation of the beads within the batch provided by our supplier, errors in the temperature control, errors in the fluid-density measurements).
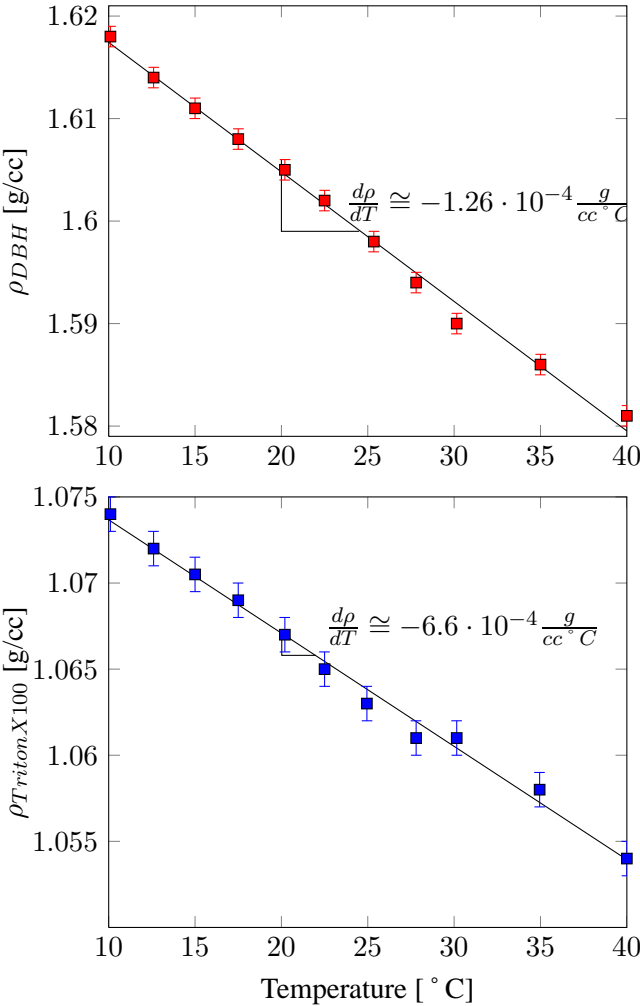
Figure 4.7: Density variation of DBH and Triton X100 with temperature.

Figure 4.8: The one week sedimentation experiment: from left to right, fluid densities of 1.1830; 1.1835; 1.1840; 1.1850 and 1.1865 g/cc. The bright part is due to a concentration of particles while the dark part means that the corresponding local volume is almost free of particules. In the 1.1840-g/cc sample, no demixing could be noted (in this experiement, particle and fluid were only density matched to allow a better sedimentation visualisation

4.2.7   Refractive index matching procedure

In § 3.5, we presented different methods to match the refractive index (RI) of a fluid mixture with that of small particles. In our experiments we used the temperature method proposed by Koh *et al.* [154, 155] because it allowed us to prepare directly the suspension at the laser wavelength used in the FPIV and LIF measurements and not just to select the clearest suspension to the naked eye. It allowed us to obtain a better index match and therefore to look further into the concentrated suspension. It limited also the mixture control to temperature. Furthermore we had no means to be sure that a bulk sample of PMMA made up of the same beads as the particles we used had the same RI. First because there are some variations of RI from one manufacture batch of the particles to another one and it was impossible to obtain beads and a bulk piece of PMMA out of the same batch. Secondly we preferred to use the particles directly because the RI may change slightly during the production of a bulk piece of PMMA. For the index matching experiments we always started with binary density matched fluids (Triton X100/DBH and UCON oil/DBH mixtures) prepared as explained in § 4.2.6. This avoided any sedimentation effects to take place during the turbidity experiments.

As the temperature variation technique needs to have a good *a priori* estimate of the RI of the particles, we took the RI value at $20\,^{\circ}$C of PMMA from the literature [51] and we prepared several fluid samples with different RI around that value (from 1.4830 to 1.4910 in our case). We performed preliminary turbidity experiments as described thereafter with this set of fluids. Results can be seen in Fig. 4.9. It can be seen that the high transmittance peak is very narrow and an accuracy up to the fourth digit in the fluid's refractive index must be achieved if we want to take measurements in a concentrated suspension. However, one should keep in mind that the further you want to see, the more precise the fluid's refractive index matching must be.

For the rough tuning of the RI we used the following variant of the Arago-Biot equation (3.9) based on the fact that we worked with density matched components:

$$(m_1 + m_2) \cdot n_{12} = m_1 n_1 + m_2 n_2 \tag{4.1}$$

We chose this equation for calculation convenience and it appeared to be precise enough for rough matching. For fine tuning, we proceeded by trials and errors by adding a small amount of one of the binary fluids to increase or decrease the mixture RI and measuring the RI of the ternary mixture after sufficient mixing with an Atago RX-5000α refractometer (ATAGO CO., LTD).
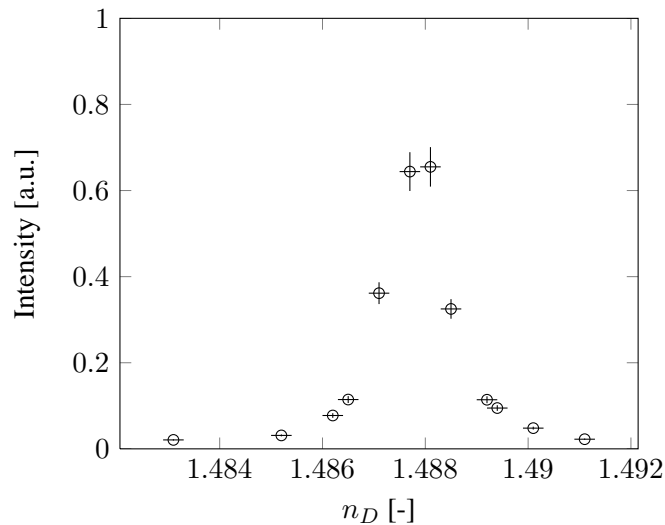
Figure 4.9: Results of preliminary turbidity experiments.

Once a suspension was prepared, a turbidity experiment as that sketched in Fig. 4.10 was performed. We used a continuous wave Hulk Series 200-mW laser (ChangChun Dragon Lasers Co., Ltd). A 532-nm laser beam was sent through a 50/50 beam splitter (CVI Melles Griot - France, Part number BSNP-532-50-1025). The beam splitter was used to monitor continuously the laser power fluctuation in time and avoid biased transmission curve due to power fluctuation. Half of the laser beam then passed through the particle suspension sample. The sample was temperature-controlled by two water cooled plates connected to a thermal bath (Julabo F34-HE circulator). Furthermore a Pt100 temperature probe was directly immersed into the sample to record precisely the sample temperature during the experiments. A typical turbidity experiment temperature profile involving five ramps is shown on Fig. 4.11. The offset between the sample temperature (Fig. 4.11, red curve) and the thermal bath (Fig. 4.11, blue curve) is due to ambient temperature. The suspension was stirred continuously during the experiment with a magnetic stirrer to ensure thermal homogeneity and improve the transmittance signal by changing the particle configuration into the beam. A pinhole was placed in front of the transmittance powermeter to reduce scattered light as much as possible.

The transmittance curve corresponding to the temperature profiles of Fig. 4.11 is shown on Fig. 4.12. In this experiment, the solid concentration ϕ_{bulk} was 15%, the mean particle diameter d_p was 100 μm.

As can be seen on Fig. 4.13 the temperature gradient $\frac{dT}{dt}$ of $\pm 1.25 \frac{°C}{hrs}$ was small enough so as to avoid any skewness in the transmission curves due to thermal inertia. Otherwise the differences from the ramps up and ramps down should be noticeable. From the mastercurve of Fig. 4.13 one can now deduce the temperature at which the ternary fluid matches the particles. We have still to measure the refractive index of the fluid at the maximum transmittance temperature using a refractometer. In the case of Fig. 4.13, the maximum was at 19.10 °C. On Fig. 4.14, several turbidity experiments were performed with different ternary fluid proportions and matching the PMMA particles at different temperature. As shown on Fig. 4.14 the RI of our PMMA particles was finally obtained from a linear interpolation of the turbidity experiments and was of 1.48847 at 20 °C. The variation of the RI with temperature was of about $-1.3 \cdot 10^{-4}$ C^{-1}. This value is in good agreement with measure from the literature [51] with bulk PMMA as can be seen on Fig. 4.15.

Conaghan and Rosen [69] developed a theory that quantifies the degree of light scattering in a sus-

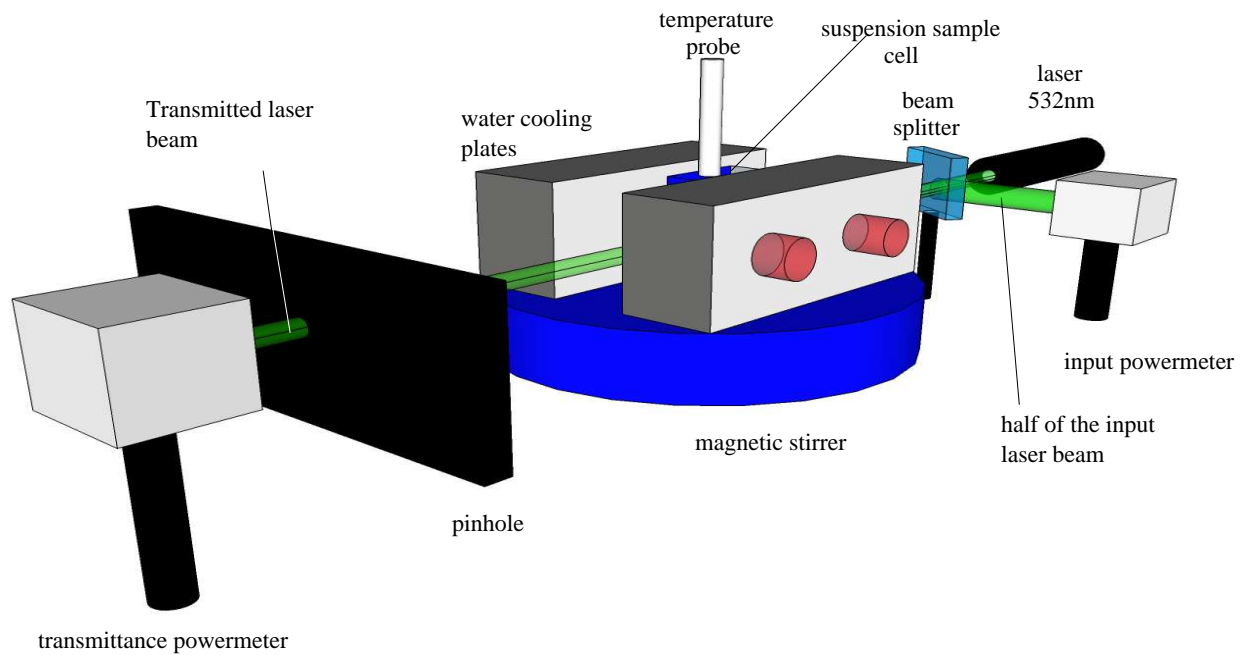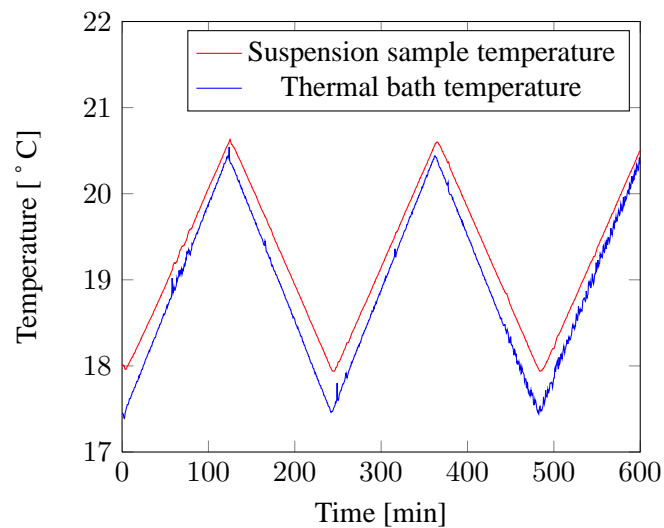Figure 4.10: Sketch of the turbidity experiment setup.

Figure 4.11: Thermal control of a typical turbidity experiment involving five ramps, the offset between the two curves is due to the ambient temperature difference.

pension as a fonction of the refractive indices of the two phases. The transmittance of light through a sample of thickness x is defined as:

$$T \equiv \frac{I}{I_0} = e^{-\tau x} \tag{4.2}$$
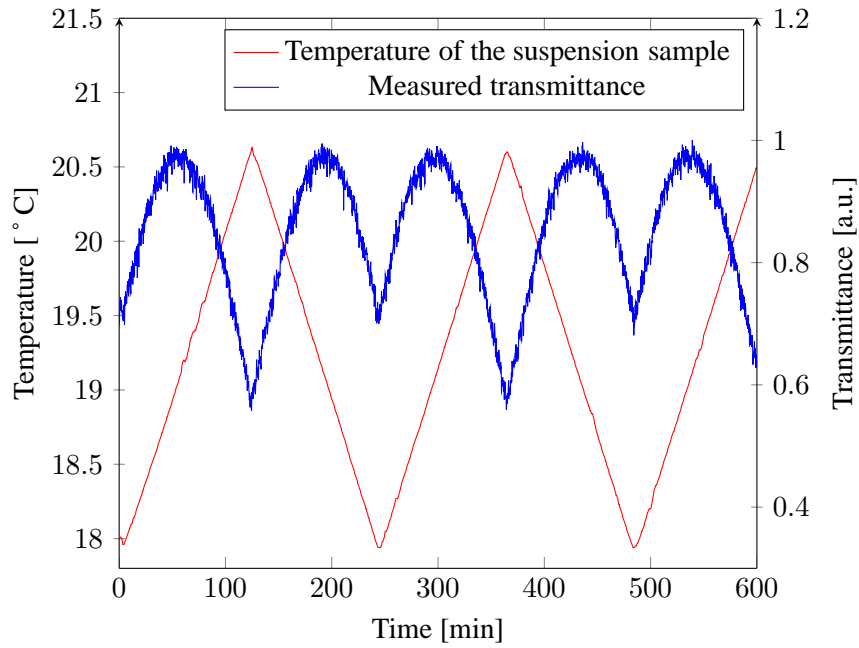
Figure 4.12: Experimental result from a typical turbidity experiment: $\phi_{mean} = 15\%$, $d_{p,mean} = 100\mu m$, $\lambda = 532nm$.
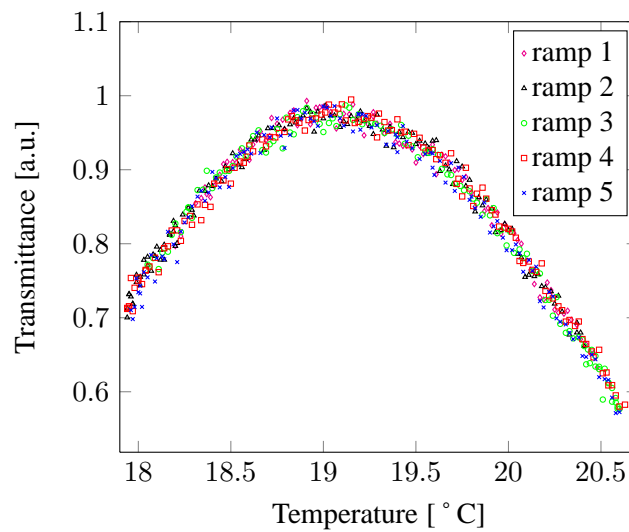

Figure 4.13: Mastercurve from the five turbidity ramp experiments of Figs. 4.11 and 4.12.

For a perfectly matched system, $T = 1$; otherwise, $T < 1$. The turbidity is given by:

$$\tau = \frac{3\phi K}{2d_p} \tag{4.3}$$

Normally, it is necessary to solve Maxwell's equation to obtain K. However for large particles
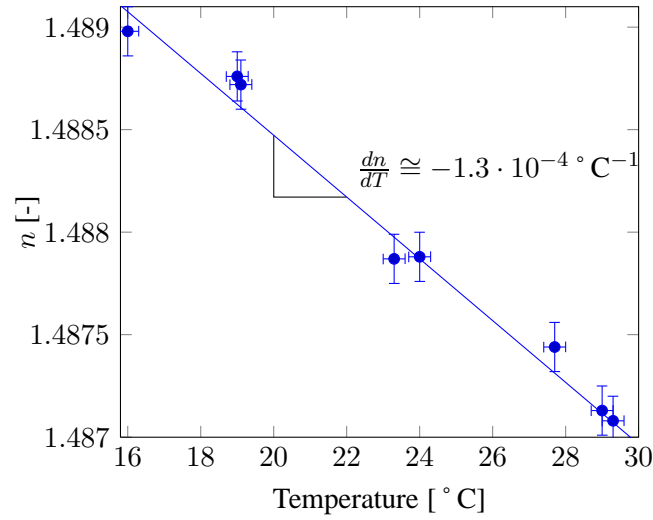
Figure 4.14: RI of the PMMA particles deduced from several turbidity experiments.
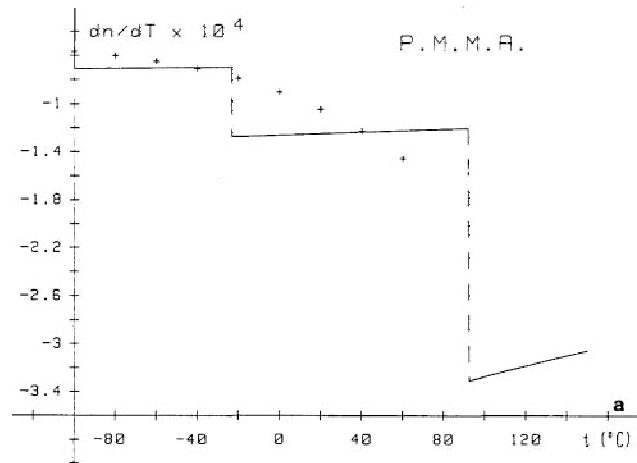
Figure 4.15: RI variation with temperature of solid PMMA (after [51]), solid line is the experimental result of Cariou *et al.* [51] and crosses represent the experimental results obained by Waxler *et al.* [306].

$(d_p \gg \lambda)$, Van De Hulst [300] derived the following relation:

$$K = 2 - \frac{4}{\rho}sin(\rho) + \frac{4}{\rho^2}(1 - cos(\rho)) \tag{4.4}$$

where

$$\rho = \frac{2\pi d_p n_s}{\lambda}\left|\frac{n_f}{n_s} - 1\right| \tag{4.5}$$

Figure 4.16 shows the experimental result of Figs 4.11 to 4.13: $\phi_{bulk} = 15\%$, $d_{p,mean} = 100$ μm, $\lambda = 532$ nm, and Conaghan's theoretical result [69] with a concentration ϕ_{bulk} of 15% and 4%. The

discrepancy between our experimental data and Conaghan's theoretical result is likely to come from two partially satisfied hypotheses in the experiment. First, one of Conahan's assumption is the use of monodisperse particles. Even if our particles were in a narrow particle size range (unsieved $50 - 300$ µm range), they were not monodisperse. Secondly, in Conaghan's derivation, only single scattering is considered. In the case of a 15% suspension, multiple scattering might occur. To find the origins of discrepancy, we should have conduct further experiments with monodisperse and lower concentration suspensions. Another explanation may lie in the fact that by stirring the suspension in the laser beam path, we reduced the particle concentration in the highly sheared laser beam area. A 4% suspension in Conaghan's equation seems to match our experimental results quite well, but we were unable to quantify shear-induced segregation in our cell. A quantitative comparison is therefore not possible.
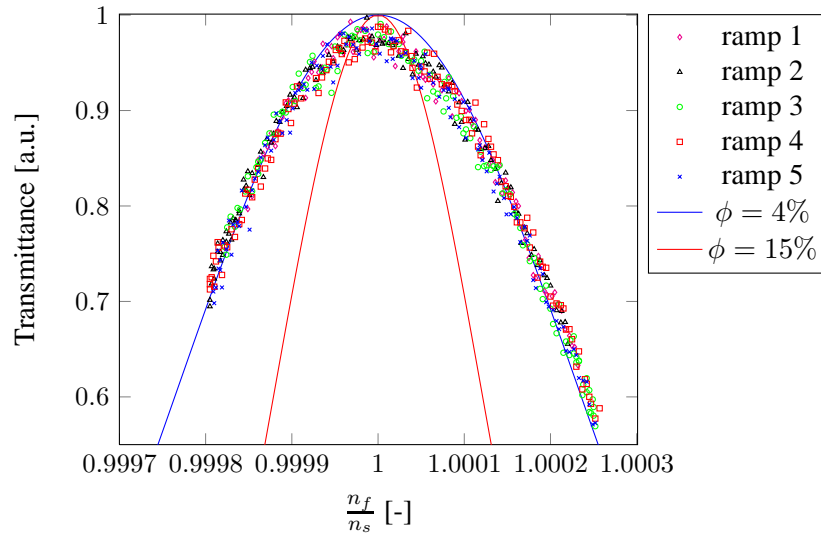

Figure 4.16: Transmission vs RI ratio $\frac{n_f}{n_s}$ of the typical experiment of figures 4.11 to 4.13, marks are experimental: $\phi_{bulk} = 15\%$, $d_{p,mean} = 100$ µm, $\lambda = 532$ nm, and comparison with the theoretical transmittance curve ($n_s = 1.48872$) with a concentration ϕ_{bulk} of 15% and 4%.

Final density and RI matched ternary fluid

The particle density and refractive index were matched using a fluid mixture with mass fractions of about 50% Triton X100, 28% DBH, and 22% UCON oil. Each of these components provides a different feature of the mixture. Triton X100 has high refractive index, DBH has high density and by using different UCON oils, one may adapt the fluid viscosity within a relatively wide range. This last property of the UCON oil family was not used during the present study. The final mixture density is 1.184 ± 0.0005 g/cc at $20\,^{\circ}$ C, the refractive index at 532 nm and $20\,^{\circ}$ C is 1.48847 ± 0.0001 and the viscosity is 0.124 ± 0.0025 Pa·s at $20\,^{\circ}$ C.

4.2.8 Molecular tagging procedure

The fluorescent dye used in the experiments was rhodamine 6G. As can be seen on Fig. 3.14 the absorption peak occurs at 524 nm and the emission peak at 565 nm. The onset of fluorescence is below 25 ps and the light emission duration (99% decay) is of 14.5 ns. It is therefore suitable to PIV measurement because these delay and duration lead to error of less than $0.1^0/_{00}$ on Δt. Rhodamine 6G was chosen

because of the closeness of the laser line to the maximum absorption of the dye and its high quantum yield. Furthermore because of the quantum efficiency of the CCD (Charge-coupled device) captor of the camera, which decrease from 55% at 500 nm to 39% at 600 nm, rhodamine 6G was prefered over other dyes (such as pyromethene 597). Nevertheless, even if they emit a weaker signal and the suspension becam more turbid farther away form the laser line, these other dyes may be used for tagging other particle species and make simultaneous measurements with two or more species using appropriate optical filters. I will just reduce somehow the depth at which we can perform measurements.
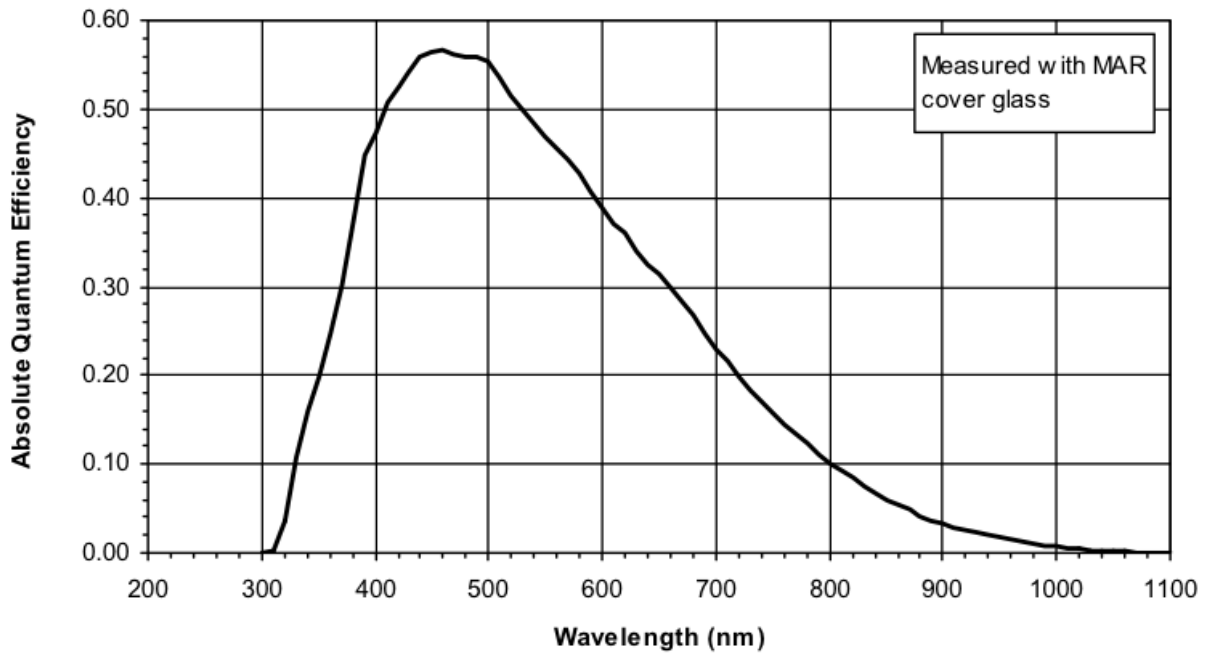

Figure 4.17: Quantum efficiency of the Powerview Plus 2 Mpixel camera (after [1]).

To maximize the amount of fluorescent light arriving at the CCD camera and, as a result, to exploit the camera intensity dynamic range, we were tempted to increase the dye concentration as much as possible until saturation is reached. On the other hand, we had to keep the concentration as low as possible to keep the refractive index of the tagged particles in a reasonable range. As measured by Oki in 2002 [226], the addition of a fluorescent dye to PMMA increases the PMMA refractive index with the dye concentration. As we can see on Fig. 4.18, Δn varies linearly with the rhodamine 6G concentration, with slope $\Delta n/\Delta C$ of 1.8750 M^{-1}. Assuming that:

- the difference in composition between the PMMA of Oki's measurements and ours has no effect on $\Delta n/\Delta C$,

- the rhodamine 6G concentration in our particles after tagging is the same as the dye-solvant mixture concentration (leading to a dye concentration of $6 \cdot 10^{-4}$ M in the PMMA particle),

leads us to find variations in the tagged-particle refractive index on the order of $1.1 \cdot 10^{-3}$. Unfortunately, for technical reasons, this value could not be checked experimentally. However, this seems reasonable. A small part of the particles being tagged, the effect of the refractive-index mismatch for this small amount of particles seems to have almost no visible effect on suspension turbidity.
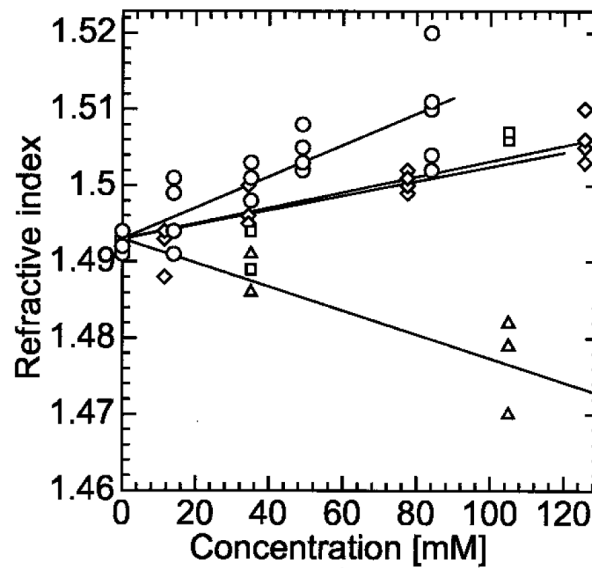
Figure 4.18: RI of dye-doped PMMA as fonction of a concentration of dopant: Circles, rhodamine 6G; Diamonds, 4-dicyanomethylene-2-methyl-6-p-dimethylaminostyryl-4H-pyran DCM; Triangles, Coumarin 500 (after [226]).

4.3 Measurement procedure

4.3.1 Interstitial fluid synthesis procedure

As explained in § 4.2, the PMMA particle density and refractive index was determined at the given working temperature of 20 ˚C. First, two binary mixtures of 1,6 dibromohexane (DBH) / Triton X-100 and DBH / UCON 75H450 were prepared in a 10-liter thermally-controlled vessel so as the density to match the 1.1840 g/cc determined earlier (see § 4.2.6). The correct fraction of each fluid in both mixtures was first calculated from the densities provided by the manufacturer. The fluid was then mixed by a propeller overnight to ensure fluid homogeneity. Both binary mixtures having the same density as the PMMA particles, the refractive index of the ternary mixture can be adapted without affecting the final fluid density. Using the two binary mixtures (high RI mixture of Triton X100 and Dibromohexane and low RI mixture of UCON oil and Dibromohexane), we prepared the final ternary fluid by calculating the proportion using the Arago-Biot equation (3.9) and (4.1). Fine tuning was then perform by trial and error.

4.3.2 Suspension synthesis procedure

The particle suspension was prepared by mixing a given amount of fluid with particles to obtain the desired suspension concentration. For measurements with rhodamine-6G tagged particles, a small amount of tagged particles was mixed with the raw batch of particle prior to mixing with the fluid part. The amount of particles and fluid was measured using a high precision scale. In the worst case, the suspension concentration error remained below 0.1 % for all the suspensions studied.

4.3.3   Suspension loading procedure

After synthesis (see §4.3.1 and §4.3.2), the particle suspension was gently poured into the quartz Couette cell to avoid formation of air bubble. The cell was then mounted on the rheometer in the controlled-temperature chamber. The suspension remained at rest for one hour for the temperature gradient to vanish. Finally the inner cylinder/vane was slowly pulled down into the suspension.

4.4   Estimation of experimental side effects

4.4.1   End effects

The total torque T_{total} applied on the inner cylinder/vane can be divided into two major contributions. A first one is due to the viscometric flow T_{visc} while the second one results from bottom end effects T_{bottom}.

$$T_{total} = T_{visc} + T_{bottom}$$

Only the viscometric component T_{visc} should be used in the flow-curve reconstruction (see 3.2). To estimate the bottom-end contribution T_{bottom} and thereby to be able to to properly measure the viscometric part, several authors proposed methods for slurries and concentrated suspensions [11, 15, 212, 278].

4.4.2   Wall slip

Wall slip is a special case of shear banding when it occurs at a wall. In particle-suspension rheometry, it is usually stated that it results from a local reduction in particle concentration, which arises from geometrical constraints [24]. Usually rough surfaces are used to reduce wall slip. Vane geometries have become popular over the years. Their supporters claim that it is equivalent to a cylinder with a wall made up of the studied fluid itself.

Authors who tried to take wall slip into account in classic rheometric procedures suggested conducting several (usually 2 or 3) experiments with inner cylinder/vane of different diameters. First, Mooney [204] proposed this technique, followed by Krieger [159], Schlegel [265], and Kiljanski [151]. This kind of technique was applied successfully to various homogenous materials. It is not clear if it can be used for concentrated particle suspensions. Indeed, because of the shear induced migration in the gap, the material does not remain homogenous and therefore the wall/suspension interaction does not remain identical between two experiments with varying geometries. In our experiments, knowing the velocity profiles of the flow, by using the measured suspension velocity at each wall, we were able to avoid this kind of techniques and all the associated unanswered questions. The velocity measurements were then directly used to correct the rheometer's angular-velocity measurement.

4.4.3   Effects of Brownian motion

The particle Péclet number Pe, an estimate of how important the viscous forces are as compared to Brownian forces, should be larger than unity for the suspension to be in a hydrodynamically-dominated regime. The Péclet number is defined as

$$Pe = \frac{\eta \dot{\gamma} r_p^3}{kT}. \tag{4.6}$$

with k the Boltzmann constant, T the temperature (293 °K), η the fluid viscosity, $\dot{\gamma}$ the shear rate, and r_p the particle radius.

In our experiments, the Péclet number was of order $O(10^6)$, which is much larger than unity. We then deduce that Brownian motion was not important, even at the lowest measured shear rates.

4.4.4 Effects of inertia

The particle Reynolds number Re_p, an estimate of the relative importance of inertial forces compared to viscous forces, should be much smaller than unity for the suspension to be in the viscous dominated or even in the frictional regime. A generalized Re_p number for shear-thinning fluids can be defined as

$$Re_p = \frac{\rho_f \dot{\gamma} r_p^2}{\eta(\dot{\gamma})}. \tag{4.7}$$

In the worst case, the generalized Reynolds number was of order $O(10^{-4})$, which was much smaller than 1. We conclude that the inertial effects were not expected to play any role.

4.4.5 Effect of gravity

In the worst scenario for sedimentation with density difference of 0.5 kg/m^3 between the particles and the fluid, the sedimentation speed u_0 of a single particle in a viscous fluid can be calculated as follows:

$$u_0 = \frac{2(\rho_p - \rho_f)g r_p^2}{9\eta} \sim 10^{-8} \text{m/s} = 0.8 \text{ mm/day}. \tag{4.8}$$

Considering the duration of the experiments, we can therefore neglect the sedimentation effect and assume a buoyancy-free flow.

4.5 Data reduction method

4.5.1 Classical rheometry

As already discussed in §2 and 3.2, inferring the flow curve $\tau = f(\dot{\gamma})$ from the torque and angular velocity (Ω_i, M_i) measurements is not obvious for concentrated particle suspensions. It is not always straightforward to infer the shear stress from the total torque because the local shear stress may depend on the flow height, i.e. on normal stresses as shown by Ancey and Coussot [15] for particle suspensions in the frictional regime. Usual techniques require an homogenous flow and fluid. Therefore the experimentalist has to check for shear localization and wall slip. This can be done quite easily by looking at the velocity profile as mentioned in §4.4.2. As we will see in chapter 5 and especially in § 5.3.1, we measured wall slip at both the inner and outer cylinder for concentrated suspensions. It varied with the tool surface roughness, tool geometry (cylinder vs vane), cylinder velocity, mean concentration, local concentration profile (due to shear induced migration) etc. Because the wall slip effect results from lots of different interacting processes, we did not try to avoid wall slip. Instead we inferred the apparent (inner or outer) cylinder velocity from the measured velocity profiles and we used them to correct the inner cylinder angular velocities. Some of the existing techniques use an *a priori* known velocity profile in the gap, i.e. an *a priori* known fluid rheology. Typical fluids are power-law fluids, Casson fluids, Bingham fluid, and Herschel-Bulkley fluids. Some of the existing techniques do not require any assumption on the fluid rheology. Direct measure of the flow profiles gives the opportunity to compare a large spectrum of Couette inversion techniques against the true flow curve derived from the local profile.

A first working basis for the appropriate methods for the frictional/viscous transition regime was provided by the papers of Nguyen *et al.* [213, 214]. More recent techniques such as the Tikhonov regularization technique proposed by Yeow [312], the simple formula techniques proposed by De Hoog and Anderssen [84, 86, 85], and the wavelet-vaguelette decomposition technique proposed by Ancey [13] can then be compared.
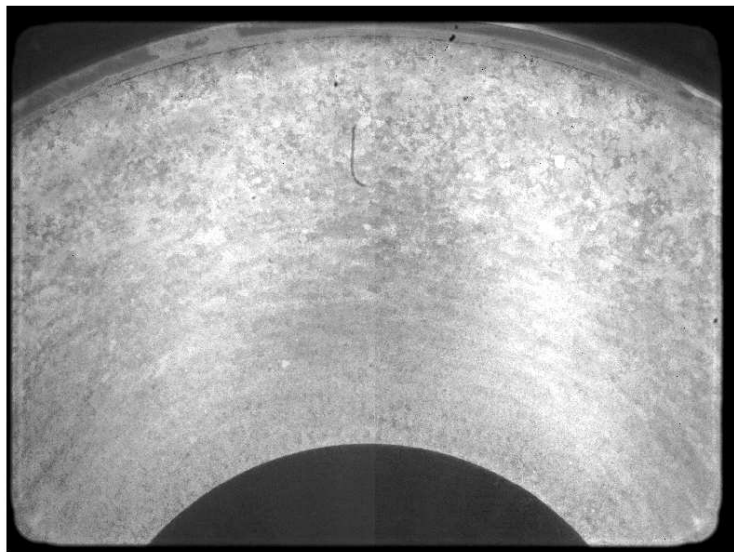
4.5.2   Spatial calibration

As shown on figure 4.1, the entire rheometer is mounted on a linear stage that allows to move the Couette cell vertically and to shine the laser sheet everywhere within the Couette cell. The very fine adjustability of the Couette cell position allows to make measurement at different heights during a single rheometrical experiment with a vertical position reproducibility of 0.02 mm.

The camera was mounted vertically on a tripod just below the quartz cup and at the working distance of $134 \ mm$ from the laser sheet with the telecentric lens. The telecentric lens has a magnification of 0.368, which corresponds to a nominal conversion factor of 19.44 µm/pixel for our CCD camera. The lens manufacturer guarantees that image distortion remains below $0.1 \ \%$. It allows therefore to perform measurements with a single conversion factor for the whole image. We preferred a non-invasive calibration technique over test pattern techniques because immersion of any kind of pattern into a highly concentrated suspension is an extremely difficult task. Furthermore it cannot be performed before starting the experiment because it would strongly interact with initial homogeneous conditions and modify them somehow. One could perform them afterwards, but with the risk of wasting the whole experiment (several days !!!) as a result of a wrong manipulation. As we will see, the non-invasive technique greatly simplifies the calibration process without interacting with the suspension and disturbing it.

Because of intrinsic magnification uncertainty of the lens and the alignment and relative positioning between the camera, Couette cell, and laser sheet, we just need to estimate the physical distance between two points. Having two concentric cylinders in our images, we could use the two circles delimited by the cylinders to retrieve the Couette cell center and to correct the lens conversion factor. Figure 4.19 shows a typical calibration image. Alignement of the Couette cell, laser sheet, and camera is performed using a high precision spirit level.

The overall error on the velocity field because of spatial calibration remains in all the experiments below 1%. The positioning error of the Couette cell center (and therefore the velocity profile position with respect to the radius) was evaluated to be at ± 3 pixels, which means about 0.06 mm.

(a)
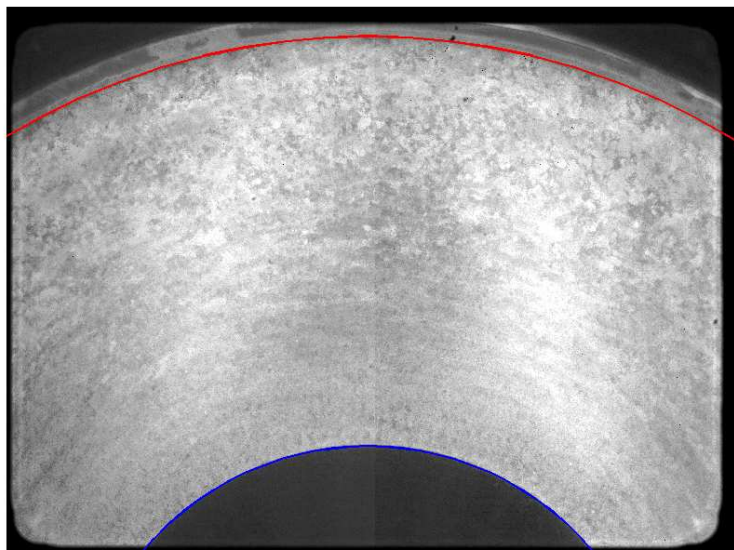
(b)

Figure 4.19: Spatial calibration and determination of the rotational axis of the Couette cell. (a) Typical raw image integrated over 100 measurement images, (b) Determination of the inner (blue) and outer (red) cylinder that allows calculation of the axis center position and the spatial conversion factor. In that example the axis is at position $(786, -402)$ in pixels and the conversion factor is 19.55 µm/pixel.

4.5.3   Velocity profiles

Velocity fields were computed using a modified version of the open source software called MatPIV [1] [283]. Computations were performed using a multiple pass scheme with a sub-window size reduction from 128×128 to 64×64, 32×32 and finally 16×16 pixels. SNR, global, local and velocity range filters were used to reject spurious correlation peaks and therefore wrong velocity vectors. As the velocity spans over a wide range, computation of the velocity profile cannot be performed using only one set of images with a given Δt. Indeed if the Δt was optimized near the inner cylinder, the PIV algorithm could not compute the velocity field correctly next to the outer cylinder and vice versa. For this reason, the velocity profile was obtained using several sets of images with different Δt.
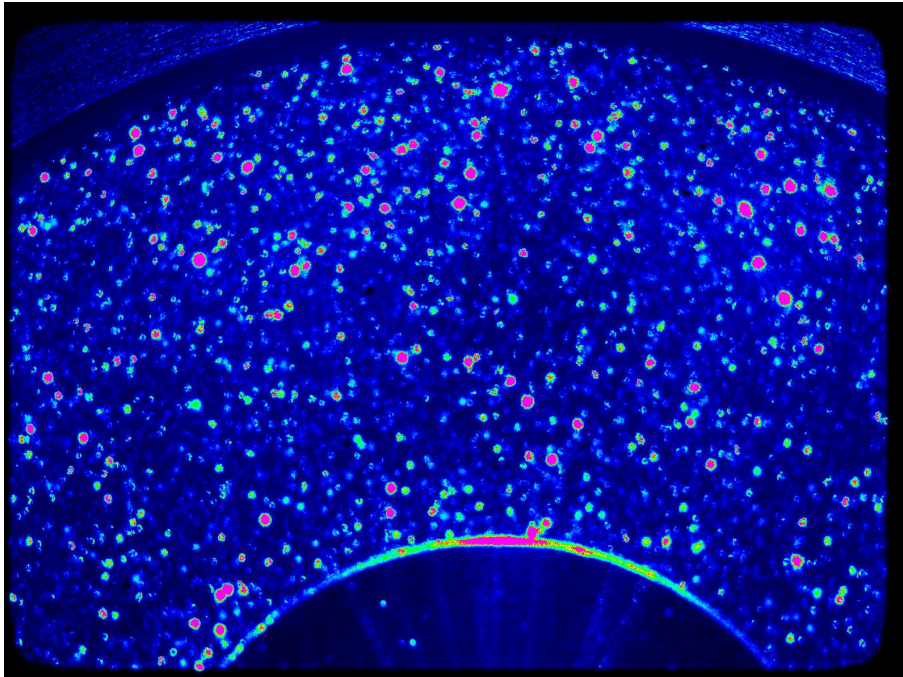

Figure 4.20: Typical PIV image in the Couette cell with a 0.55 volume fraction coarse particle suspension at 20 mm into the suspension (Color is only a pseudocolor scale that represent the light intensity scale).

---

1. http://www.math.uio.no/~jks/matpiv/

5

Experimental results

This chapter is concerned with the experimental data that we obtained with concentrated particle suspensions using a Couette cell. We first present validation tests, where the acquisition method was tested against homogeneous Newtonian fluids. Emphasis is given to the inner shearing tool, which could be either a 6-blade vane or a roughened metallic cylinder. Although the vane has been routinely used in the rheometry of slurries and pastes (because it has been supposed to provide better-viscometric flow conditions), it induces undesired effects (e.g., secondary flows), which precludes us from using it for our rheometric experiments. Focus is then given to velocity profiles, which can be used to derive the flow curve. I compare the flow curves obtained by differentiating the velocity profiles and those obtained by solving the inverse Couette problem.

5.1   Validation of the measurement setup with a seeded Newtonian fluid

For validation purpose, we used a Newtonian trimix and PMMA particles as seeding particles for the PIV/PTV treatment (they are the same as those used for the concentrated suspensions). Figure 5.1 reports the radial and azimuthal velocity profiles that were experimentally obtained as well as the exact analytical solution for the Couette geometry. Good agreement is found, which provides evidence that the acquisition method performs well.

5.2   Vane geometry

The use of vane geometries has become quite popular over the past 25 years for measurements of flow properties of non-Newtonian liquids, which are prone to undergo large slip effects at smooth walls. Originally, these geometries were used to measure the apparent yield stresses of dispersions [257], but they have recently been used to measure other rheological parameters. A recent review of the vane geometry can be found in an article of Barnes [25]. As strong wall slip effects have to be expected in concentrated suspension with a high packing fraction, we performed in parallel all measurements using a 6-bladed vane geometry and a rough sand-blasted inner cylinder with the same diameter. As we will see in this section, we are facing two major issues when using a vane with concentrated suspensions:

- recirculation vortices between the vane blades, which led to higher wall slip (at the apparent cylinder cut by the blade tips) compared with a sand-blasted cylinder (see § 5.2.1) than with a smooth cylinder;

- discrepancies between the measured, almost hexagonal, 6-bladed-vane flow field and a circular Couette flow (see § 5.2.2).
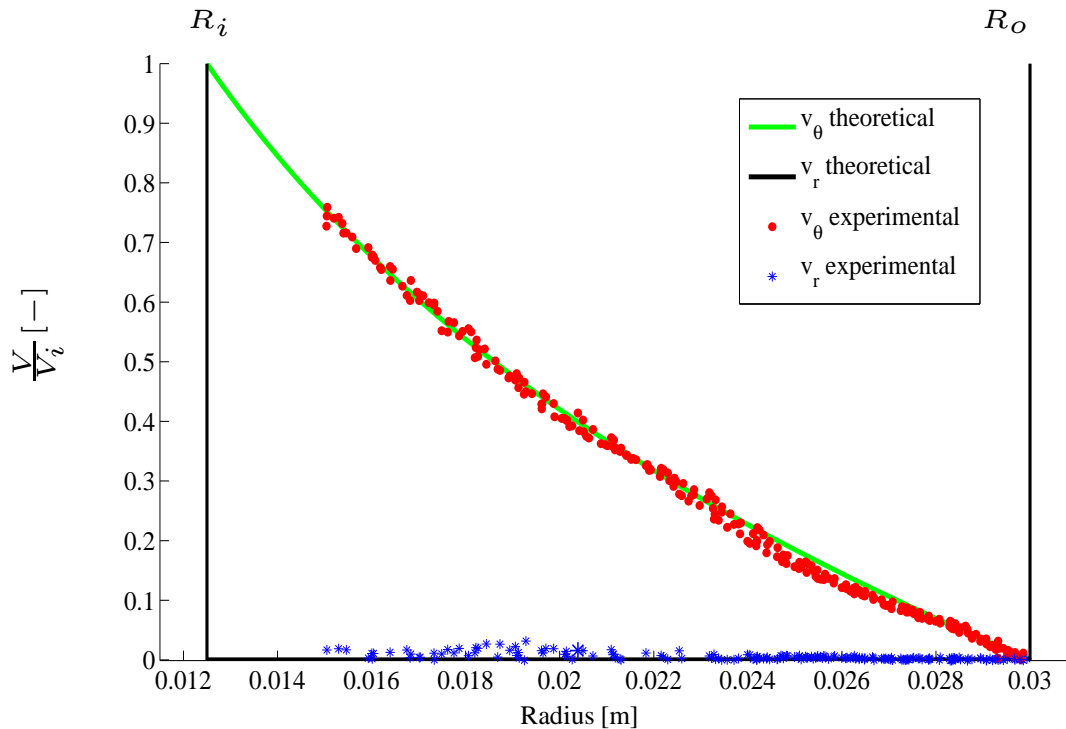
Figure 5.1: Setup validation using trimix Newtonian fluid with a negligible amount of tracer particles for PIV measurements: dimensionless velocity profile (inner cylinder angular velocity is 1 rad/s and inner cylinder diameter is 25 mm).

5.2.1 Interblade recirculation

In his review of the vane geometry [25], Barnes already mentioned limitation in its use for high-viscosity liquids. He also mentioned the possible formation of vortices behind the vane blades for low-viscosity liquids. However, this has remained so far an assumption. In our experiments, we used a 6-bladed vane with a diameter of 25 mm, and as can be seen on figure 5.2, the velocity field showed a flow recirculation in the clearance between the blades, confirming Barnes' hypothesis. Our spacial resolution allowed to clearly identify the main vortex just behind each blade. It seems to be a secondary vortex with an opposite vorticity in front of the blade, next to the inner shaft. As we will see in § 5.3.1, this recirculation process has a strong impact on the apparent inner cylinder wall slip. For non-colloidal particle suspensions, the presence of a vortex behind the blades is enhanced by the shear-induced diffusion process (see § 2.2 and § 2.3.2). Indeed at high packing fraction, the MRI measurements of Ovarlez *et al.* [229] have shown concentration differences within the $2 - 4\%$ range between the inner cylinder and the outer cylinder in these concentration range. These differences correspond to a change in local viscosity of about two to three orders of magnitude. Therefore the effective viscosity next to the vane will be relatively low compared with the outer wall region. This questions the use of vane geometries for measuring rheological properties of non-colloidal particle suspension (except for yield stress measurements). As we will see in § 5.3.1, we were never able to obtain a no-slip condition with the vane geometry, which remains yet its main purpose.
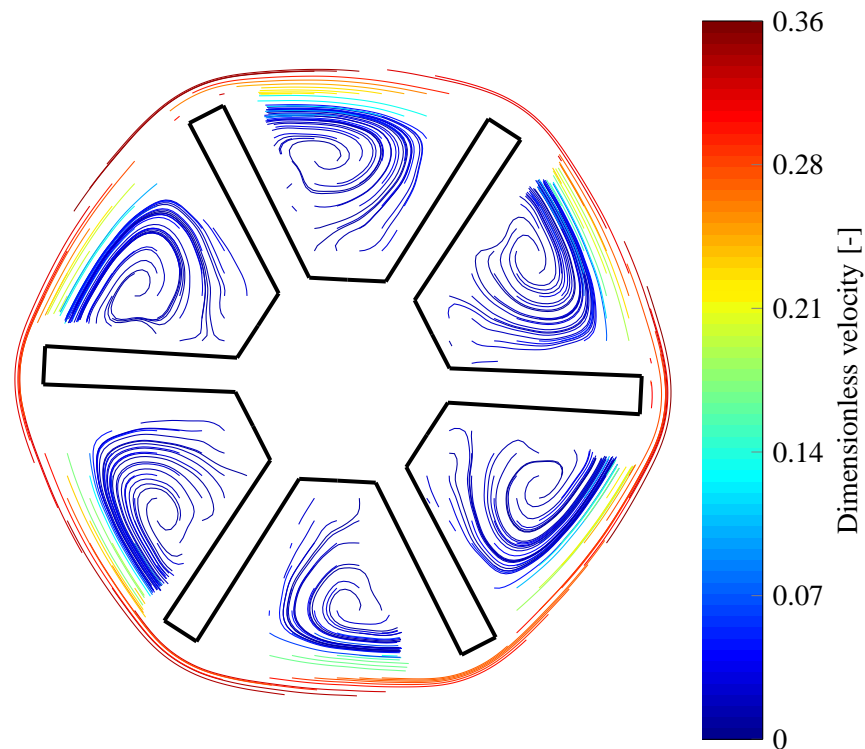
Figure 5.2: Streamlines of the interblade flow recirculations using a vane geometry: the inner 6-bladed vane has a diameter of 25 mm and an angular velocity of 1 rad/s, the particle suspension has a volume fraction of 0.5. The color scale represents the dimensionless velocity magnitude in the frame of reference attached to the vane (adimensionalized with the apparent outer cylinder velocity. Vane diameter is 25 mm, and the outer cylinder rotates clockwise in this frame of reference).

5.2.2   Gap stream

As can be seen at the blade tips on figure 5.2 and 5.3, the flow deviates substantially from a circular Couette flow. It looks more like a hexagonal flow near the vane and slowly rounds off when increasing the radius. This result is qualitatively in agreement with the numerical simulations of Barnes and Carnali [27]. Figure 5.4 shows the radial component of the velocity field around one blade. The whole width of the gap is influenced by a vane blade. The radial component ranges from about -7 % to 7 % of the inner cylinder velocity. We performed experiment for two different particle volume fractions (0.5 and 0.55) and several angular velocities between 0.01 and 10 rad/s. The velocity fields were similar when adimensionalized by the apparent inner cylinder velocity. We retrieved in each case a radial velocity component up to 7–10 % of the inner apparent cylinder velocity.

Finally, because of this interblade recirculation vortices, which generated non-negligible apparent wall slip and because of the non-circular streamlines in the gap, we preferred to the inner sand-blasted cylinder for the rheological measurements (see § 5.3 and § 5.5).
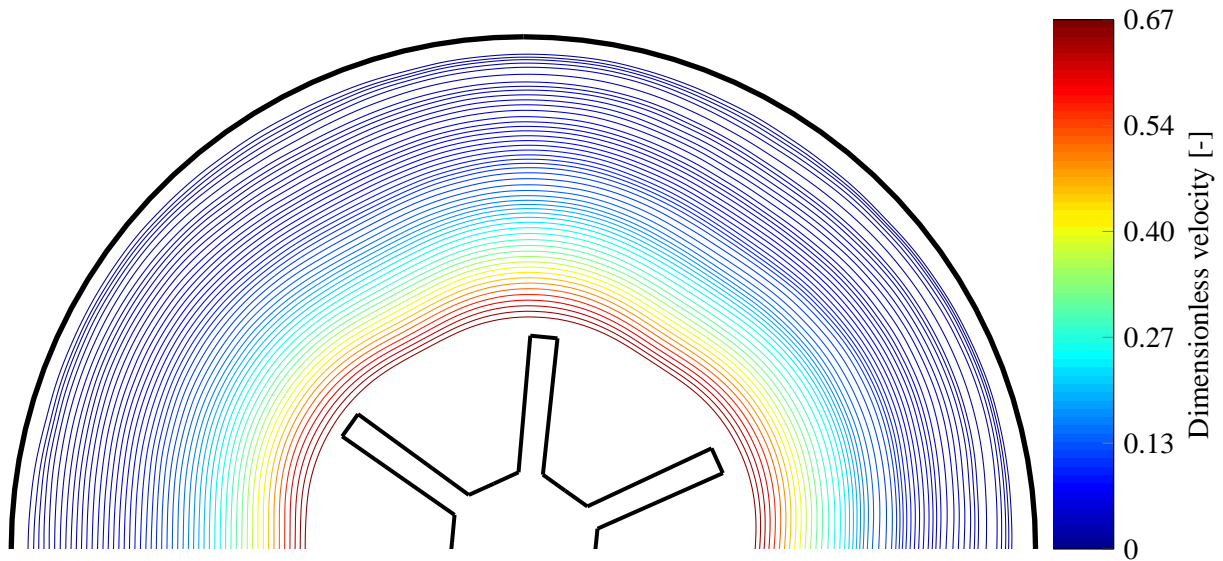
Figure 5.3: Streamlines in the gap using a vane geometry: The color scale represents the dimensionless velocity magnitude (adimensionalized with the apparent inner cylinder velocity, inner 6-bladed vane with $\varnothing = 25$ mm, angular velocity 1 rad/s, particle volume fraction of 0.5).
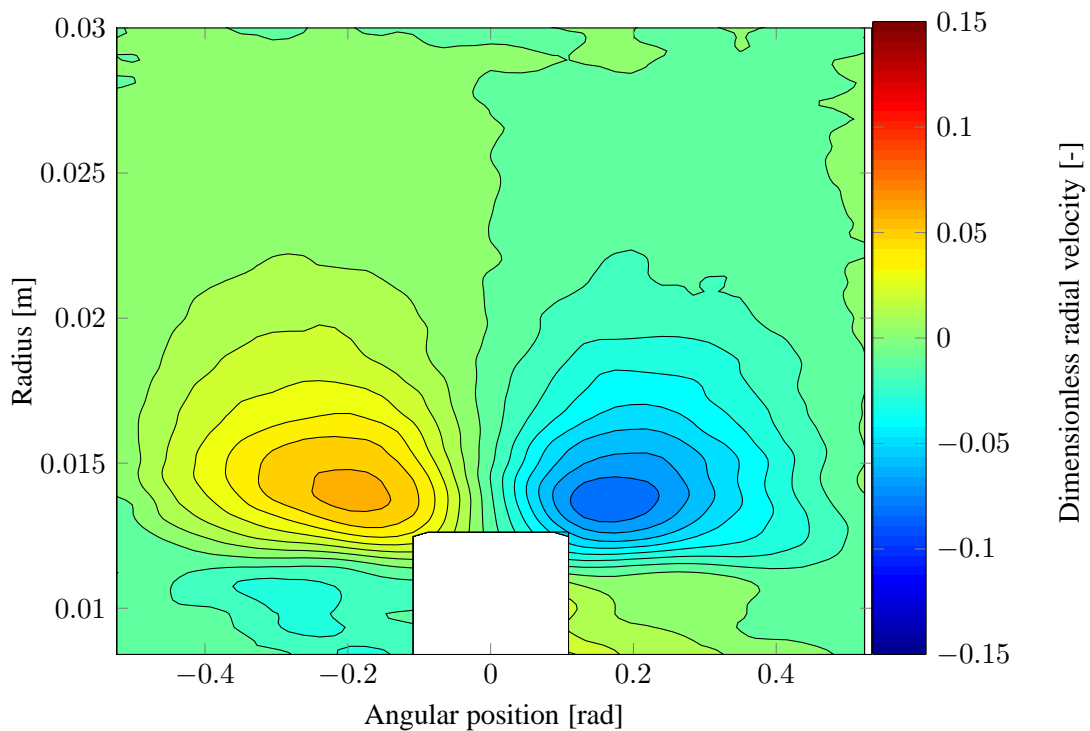
Figure 5.4: Radial velocity component around one blade (positioned at $\theta = 0$, adimensionalized with the apparent inner cylinder velocity, inner 6-bladed vane with $\varnothing = 25$ mm, angular velocity 1 rad/s, particle volume fraction of 0.5).

5.3 Steady-state measurements

All the measurements presented here were made when the velocity and particle concentration profiles reached a steady state, i.e. when the shear-induced diffusion process was at equilibrium. During an experiment, the shear flow reduced residual settling; no substantial change in the measured torque was observed. The reason why steady-state measurements are attractive is that they are easily reproducible. Furthermore, as shown by Ovarlez *et al.* [229] (see figure 5.5), as soon as a steady state is reached, the concentration profile seems to be independent of rotational velocity. As we will see in §5.3.3, this is useful to infer the true locally-derived flow curve.
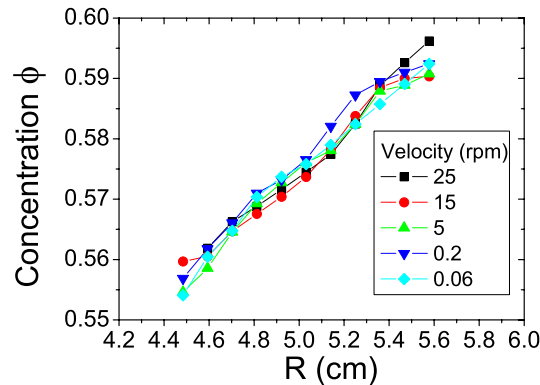

Figure 5.5: MRI concentration profile of concentrated particle suspension in a Couette cell for a suspension of mean volume fraction 58% at various rotational velocities (after [229]).

5.3.1 Wall slip

As already mentioned in §4.4.2 and §4.5.1, wall slip is an important issue in particle suspension rheometry. The actual trend in standard rheometry is to try to reduce it by any possible means because it is the easiest way to obtain valuable results without any recourse to heavy techniques such as the use of several inner cylinders as mentioned in §4.5.1. In concentrated particle suspensions, wall slip reduction has been done either by using an inner vane instead of the inner cylinder or by gluing sandpaper on the geometries. From our velocity field measurements, we could infer the velocity at the walls by an extrapolation of azimuthal velocity profile within the gap and compare it to the angular velocity measured or imposed by the rheometer. In all our measurements with concentrated particle suspensions, we measured a wall slip at both the inner and outer cylinder. We were never able to reduce wall slip to zero.

In this section, we will take a closer look at wall slip for both geometries in the steady-state regime. As we will see, wall slip is very complex and has various origins. In subsequent experiments, we did not try to avoid wall slip at any price, which is hopeless to our eyes. Instead, we used the measured inner and outer extrapolated slip values inferred from the velocity profiles to correct the angular velocity values measured by the rheometer. As we will see here, this task is relatively easy for wall slip on the outer cylinder because the shear rate tends there to zero. On the contrary, at the inner cylinder, the shear rate is at its maximum and it is relatively difficult to estimate wall slip accurately. In all experiments presented in this section, we used either a 6-blade vane ($\varnothing 25$ mm) or a rough sand-blasted inner cylinder ($\varnothing 25$ mm). For the outer cylinder, we used a smooth quartz cup ($\varnothing 60$ mm). The velocity profiles were taken at 25 mm from the bottom of the cell (i.e. at mid-height).
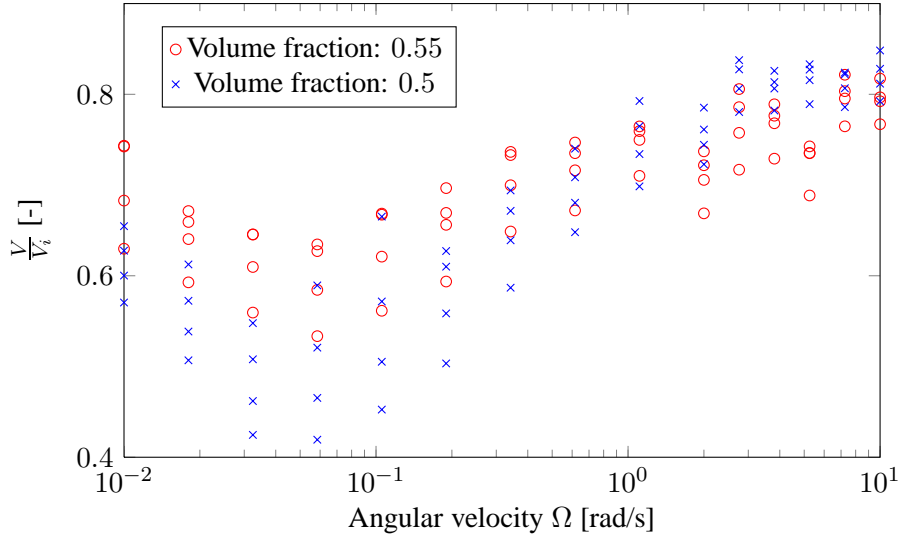
Inner cylinder velocity effects

Figure 5.6: Inner cylinder wall slip: inner cylinder wall slip velocity vs angular velocity
Values of the extrapolated inner slip velocities versus the inner cylinder angular velocities. The velocities are adimensionalized with the inner cylinder velocities (inner sand-blasted cylinder $\varnothing = 25$ mm, particle volume fraction $\phi = 0.55$ (○) and 0.5 (×)).

As shown on figure 5.6, wall slip at the inner cylinder is not constant with the inner cylinder velocity. The raw velocity profiles next to the inner cylinder can be found in appendix D. The measurements first show a slip increase when Ω lies between 0.01 rad/s and 0.05 rad/s; then, the wall slip reduces to about 20% for $\Omega \sim 10$ rad/s. This trend seems to be weakly dependent on mean concentration (for the concentration range we worked in).

On the contrary, at the outer cylinder (smooth quartz cup in our case), in the steady regime (i.e. once the shear induced diffusion is at equilibrium), wall slip was almost independent of the inner cylinder velocity. Within our measurement errors, we were unable to see any trend in its variation with the inner cylinder velocity. Once an apparent steady-state regime was reached, the slip velocity seemed to be influenced essentially by the wall, the particles, the fluid, and the proportion of each of them. This is in agreement with the concentration profiles measured by Ovarlez *et al.* [229], which showed an independent steady-state concentration profile with the inner cylinder velocity. More focused experiments on this issue should be carried out to really understand what occurs at the smooth outer wall. This goes beyond the scope of this work. We just limited ourselves here to the fact that the measured slipping velocity was independent of the inner cylinder velocity. As shown on figure 5.7, this means that at low rotational velocities (i.e. $\sim 0.01 - 0.5$ rad/s), wall slip may be not negligible at the outer cylinder, with a relative value of a few percent of the inner cylinder velocity, whereas at higher velocity, it becomes completely negligible (see also figure D.2 and D.3 in appendix D for the raw velocity profiles). We finally used this value for the wall-slip-corrected flow curve in § 5.3.2.

Inner geometry

As shown in § 5.2, the 6-blade vane induces recirculation loops in the inter-blade space. For this reason, at the apparent inner cylinder cut by the vane blades, the suspension velocity was not that of
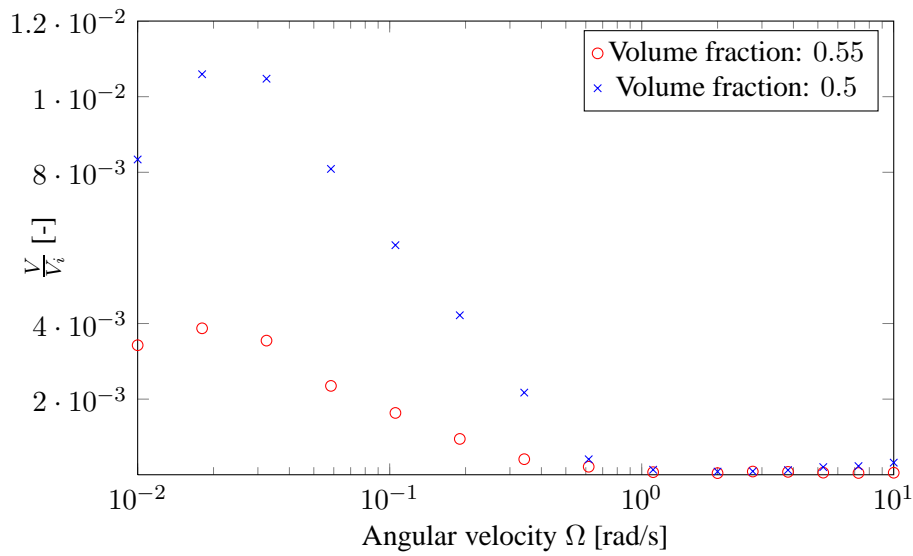
Figure 5.7: Outer cylinder wall slip: wall slip vs angular velocity
Value of the extrapolated outer slip velocity versus the inner cylinder angular velocity. The velocities are adimensionalized with the inner cylinder velocities (inner sand-blasted cylinder $\varnothing = 25$ mm, particle volume fraction $\phi = 0.55$ ($\circ$) and 0.5 ($\times$)).

the blade tips. It was rather influenced by the vortex recirculation velocity. As shown on figure 5.8, compared with a sand-blasted inner cylinder, the apparent wall velocity was lower for the vane than the sand-blasted cylinder, i.e. there was more slip with the vane. For this reason and those presented in §5.2 (keeping a flow as viscometric as possible), in order to compare the local measurements with those obtained in classic rheometry, we mainly concentrated our measurement on the sand-blasted inner-cylinder experiments.
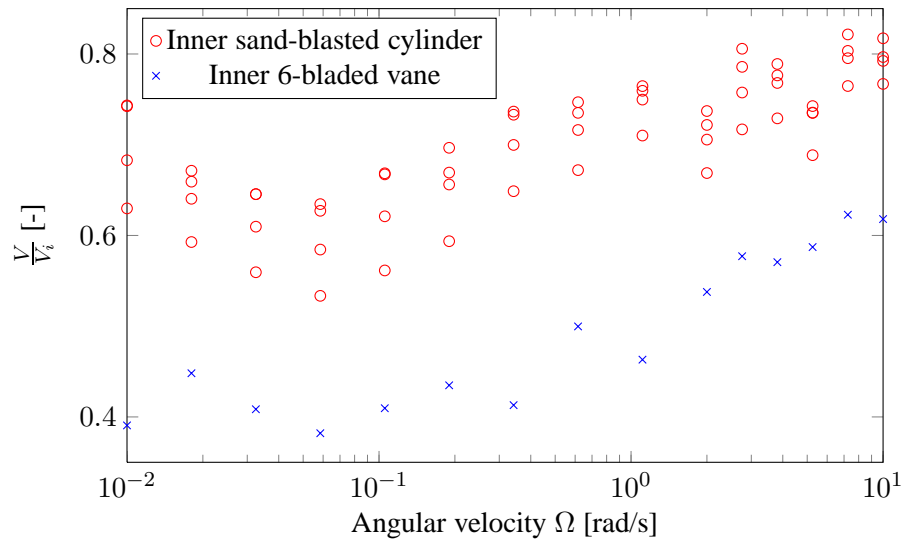
Figure 5.8: Inner cylinder wall slip: inner cylinder vs vane

Values of the extrapolated inner slip velocity for an inner cylinder ($\circ$) and an inner 6-bladed vane ($\times$). The velocities are adimensionalized with the inner cylinder velocity and the inner apparent cylinder velocity (inner sand-blasted cylinder $\varnothing = 25$ mm and inner 6-bladed vane $\varnothing = 25$ mm, particle volume fraction $\phi = 0.55$).

5.3.2   Rheometric flow curve

Once wall slip has been measured correctly, the raw angular velocity can be properly corrected (see figure 5.9 (a) and 5.10 (a) for the corrected and uncorrected measurements). Moreover, as already discussed in § 3.2 and illustrated with artificial Herschel-Bulkley data, deriving the flow curve from Couette-cell measurements (with a wide-gap cell) gives rise to inversion problems. As we have already seen, the inferred flow curve may be relatively different depending on the inversion technique. Figure 5.9 (b) and 5.10 (b) show the inferred flow curves using several different techniques with and without wall slip correction. The differences between curves are indeed quite large. These results again show the problems associated with the rheometry of concentrated particle suspension, which requires the use of wide-gap rheometers to avoid finite-size effects and, as a result, generates:

- measurements with a wide range of shear rate within the gap (see figure 5.12),

- a non-homogenous material (see figure 5.5),

- a Couette inversion technique problem (see § 3.2).

As discussed in § 2.4, § 3.1, and § 3.2, from these bulk measurements alone, it is not possible to answer the underlying questions addressed in this work associated with the above listed effects:

"Is it possible to obtain a reliable flow curve for concentrated particle suspensions from bulk measurement? And this by considering the wide shear range within the gap, the non-homogeneous material and the inversion techniques problems due to the wide gap?"

As we will see in §5.3.3, local measurements will help us to understand further the different aspects and try to answer, at least partially, that question.

(a)

(b)

Figure 5.9: Cylinder wall slip: effect on the bulk measurements
Semi-logarithmic plot of wall slip uncorrected (●) and corrected (×) raw rheometric measurements (a) and the inferred flow curves (b) obtained with following inversion methods: Mooney (●, ×) [204], Newton (●, ×), power law (●, ×), mid-point formula (●, ×) [86, 84], modified mid-point formula (●, ×) [86, 84] , quart-point formula (●, ×), three-eight-point formula (●, ×), modified first-term Krieger-Elrod formula (●, ×) [86, 84], modified-quart-point formula (●, ×), modified-three-eight-point formula (●, ×), Krieger (1952) (●, ×) [159], Krieger (1953) (●, ×) [158], Krieger (1968) (●, ×) [163], Mac Sporran (●, ×)[185], Tikhonov regualrization (●, ×) [312], wavelette-vaguelette decomposition (●, ×) [12] (inner sand-blasted cylinder ∅ = 25 mm, particle volume fraction $\phi = 0.55$).
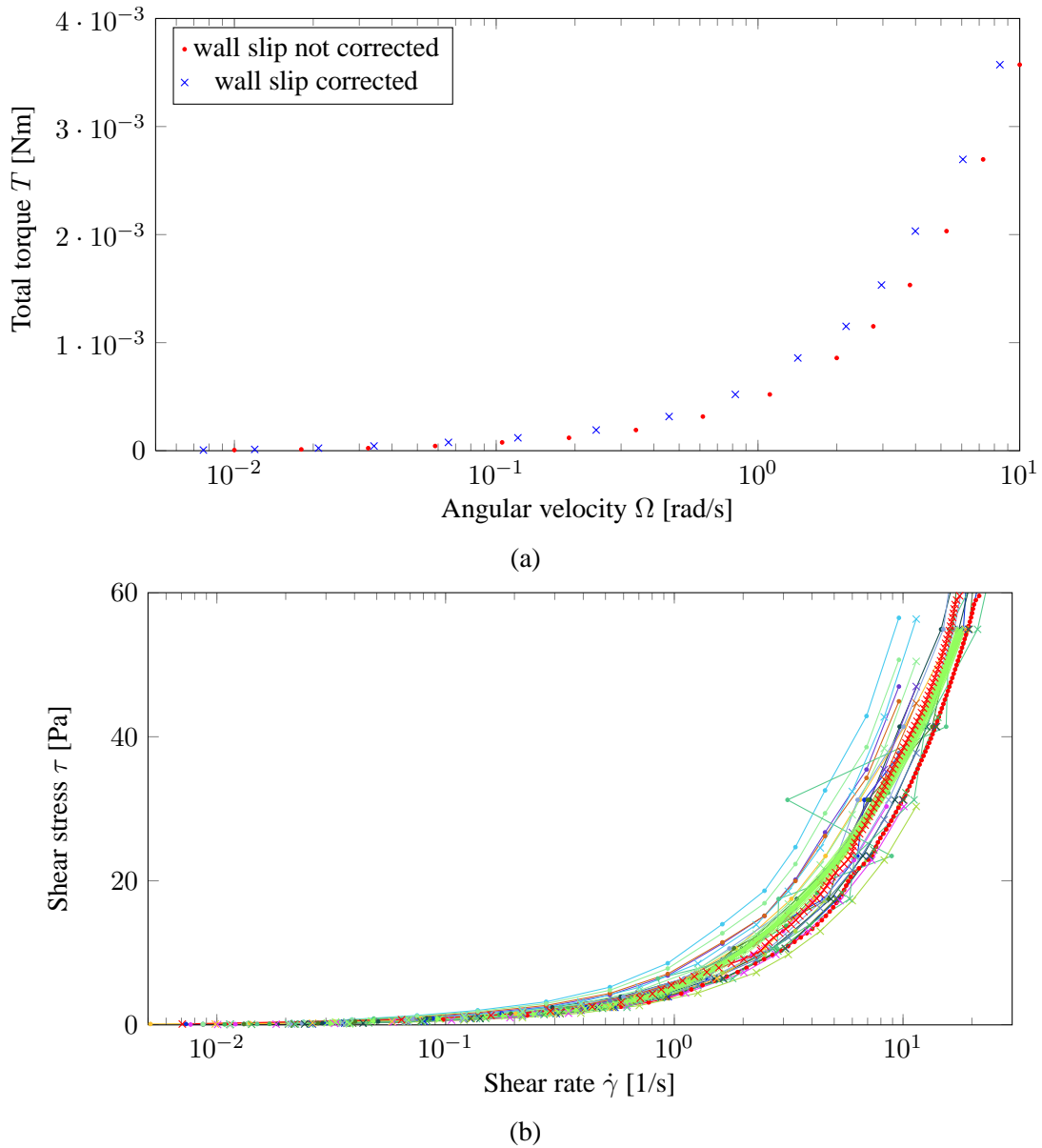
(a)

(b)

Figure 5.10: Cylinder wall slip: effect on the bulk measurements

Log-log plot of wall slip uncorrected (•) and corrected (×) raw rheometric measurements (a) and the inferred flow curves (b) obtained with following inversion methods: Mooney (•, ×) [204], Newton (•, ×), power law (•, ×), mid-point formula (•, ×) [86, 84], modified mid-point formula (•, ×) [86, 84] , quart-point formula (•, ×), three-eight-point formula (•, ×), modified first-term Krieger-Elrod formula (•, ×) [86, 84], modified-quart-point formula (•, ×), modified-three-eight-point formula (•, ×), Krieger (1952) (•, ×) [159], Krieger (1953) (•, ×) [158], Krieger (1968) (•, ×) [163], Mac Sporran (•, ×)[185], Tikhonov regualrization (•, ×) [312], wavelette-vaguelette decomposition (•, ×) [12] (inner sand-blasted cylinder ⌀ = 25 mm, particle volume fraction $\phi = 0.55$).
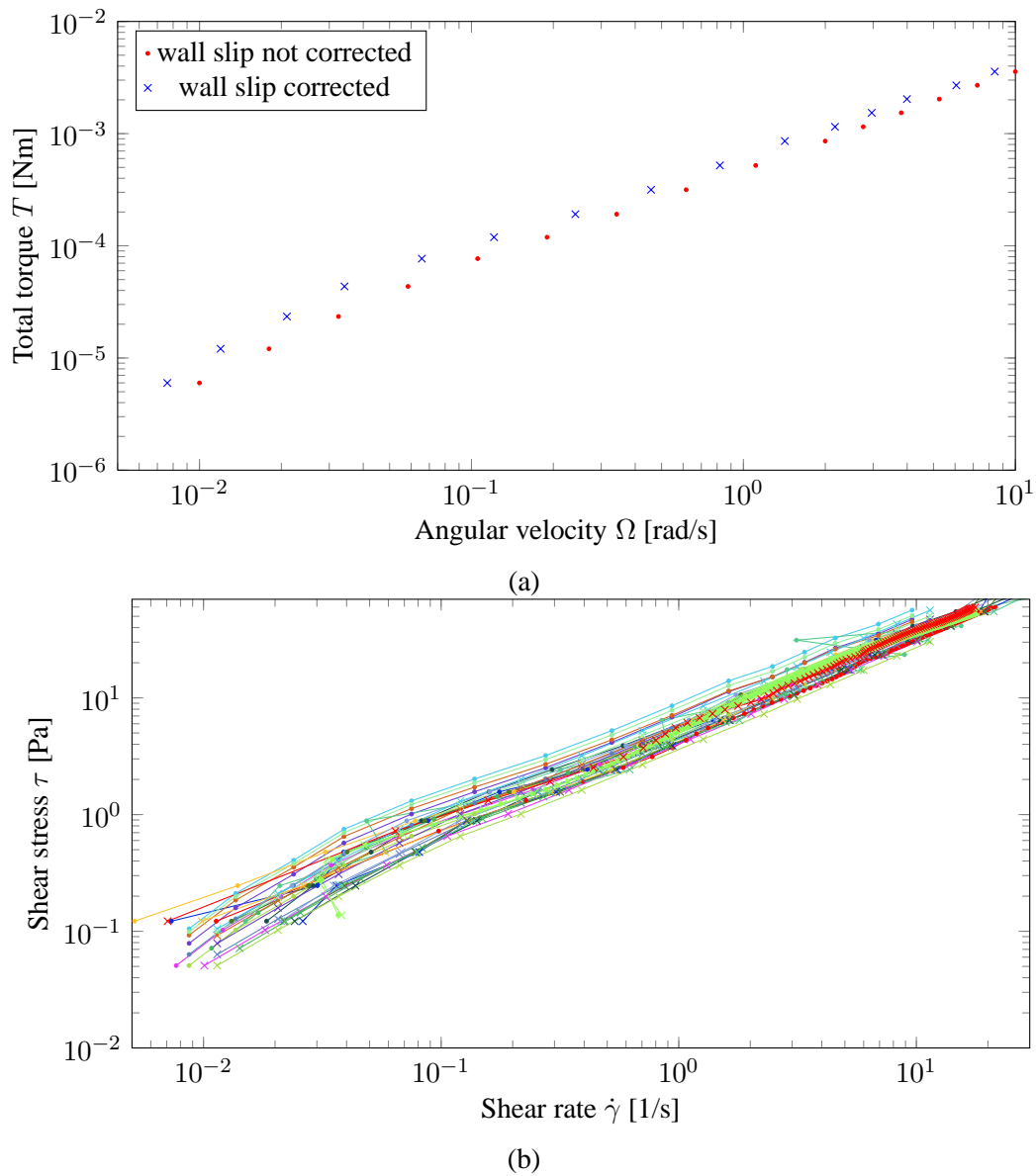
5.3.3 Rheometry versus rheophysics

In the steady-state regime (i.e. when shear induced particle diffusion is at equilibrium), the measured azimuthal-velocity profiles of concentrated particle suspensions experience a sup-exponential decay next to the inner cylinder. However, near the outer cylinder, we measured an abrupt change in the profiles. Its origin is not yet clear. Figure 5.11 shows the azimuthal velocity profiles for the inner-cylinder angular velocity ranging from 0.01 to 10 rad/s for a suspension with a particle volume fraction of 0.55. From these velocity profiles, the shear rate distribution in the gap can then be calculated for each rotational velocity. These are represented in Fig. 5.12. As shown by this figure, the shear rate within the gap spans over two (0.01 rad/s curve) to six (10 rad/s curve) orders of magnitude. For some unknown reasons, because of the well-marked velocity-profile slop change in the outer wall region, the measured shear rate never went below 10^{-4} 1/s. This phenomenon is unclear and should be examined more carefully.
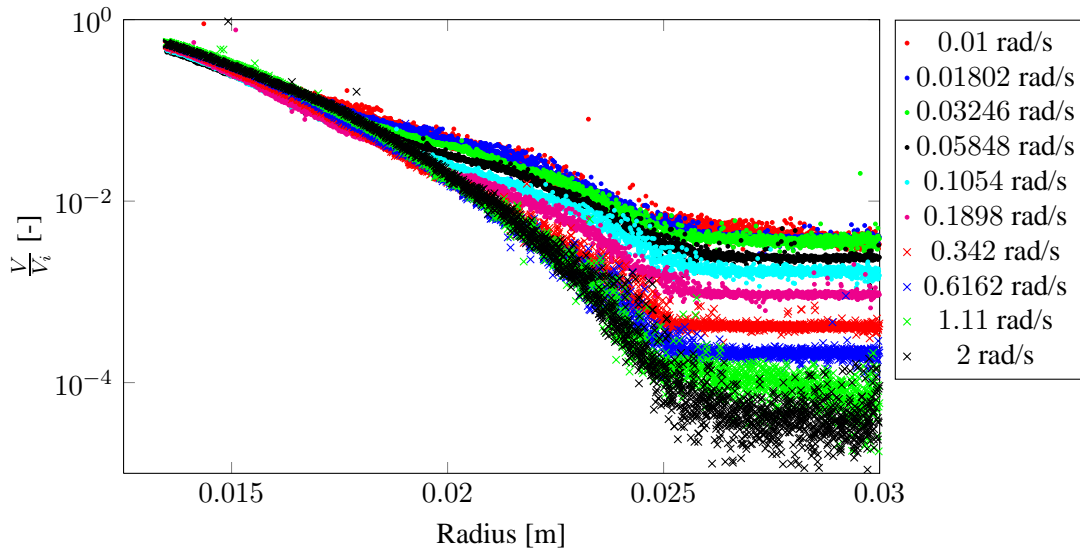

Figure 5.11: Dimensionless azimuthal velocity profile at several inner cylinder velocities: 0.01 rad/s ($\bullet$), 0.01802 rad/s ($\bullet$), 0.03246 rad/s ($\bullet$), 0.05848 rad/s ($\bullet$), 0.1054 rad/s ($\bullet$), 0.1898 rad/s ($\bullet$), 0.342 rad/s ($\times$), 0.6162 rad/s ($\times$), 1.11 rad/s ($\times$), and 2 rad/s ($\times$). The velocities are adimensionalized with the inner cylinder velocities (inner sand-blasted cylinder $\varnothing = 25$ mm, particle volume fraction $\phi = 0.55$). For clarity, the measurement between 2 and 10 rad/s where not reproduced here. Raw measurements can be found in figure D.9 and D.10

Nevertheless, from inferred shear-rate profiles and measured steady-state torques at the inner cylinder, local flow curves can be derived. Figure 5.13 shows (i) the calculated flow curves using several inversion techniques for solving the Couette equation and (ii) the locally-inferred flow curves at each angular velocity. The bulk measurement cross the local ones at a given point (we will come back to this thereafter). What seems to happen in fact in global methods is that at a given angular velocity, the bulk measurements somehow average the values over the whole gap.

If the locally-inferred flow curves would fulfill all the assumptions presented in § 3.2, they should collapse on a single curve, which is not the case. There is a simple reason for that: as briefly mentioned in chapter 2 and at the beginning of § 5.3, the shear-induced particle diffusion process generates a non-homogeneous material in the gap. Therefore, to infer properly the flow curve in a wide-gap Couette rheometer with a wide range of shear rate and a non-homogeneous material, simultaneous measurements
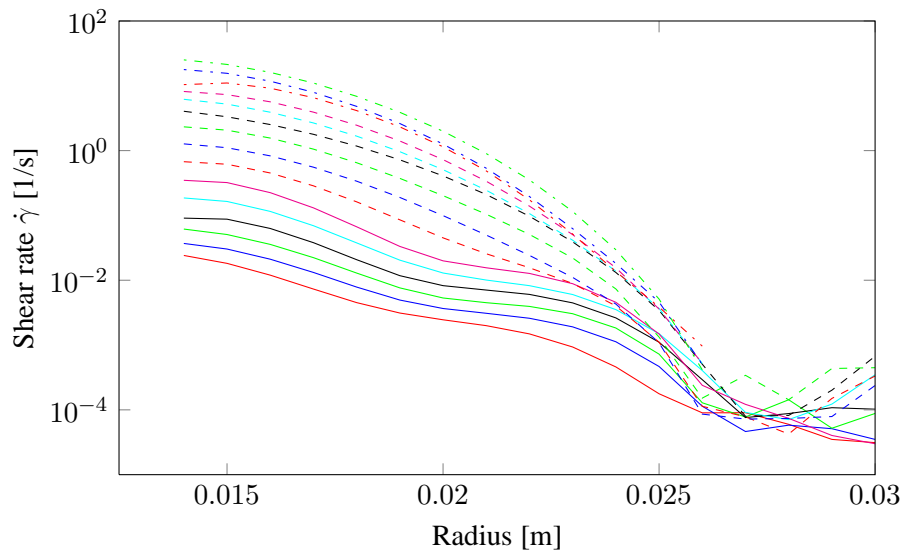
Figure 5.12: Steady state shear rate within the gap: at 0.01 rad/s (—), 0.01802 rad/s (—), 0.03246 rad/s (—), 0.05848 rad/s (—), 0.1054 rad/s (—), 0.1898 rad/s (—), 0.342 rad/s (--), 0.6162 rad/s (--), 1.11 rad/s (--), 2 rad/s (--), 2.759 rad/s (--), 3.807 rad/s (--), 5.253 rad/s (-·-), 7.248 rad/s (-·-), and 10 rad/s (-··-). (inner sand-blasted cylinder $\varnothing = 25$ mm, particle volume fraction $\phi = 0.55$ and inner cylinder angular velocity $\Omega = 0.1$ rad/s).

of the velocity and particle concentration fields have to be carried out. Unfortunately we have not been able as yet to perform reliable concentration measurements. MRI steady-state concentration profiles given in the literature [229] have shown, that these profiles are independent of the angular velocity at which the measurement is taken. Following this, we can plot the flow curve for a given particle volume fraction by plotting the data at a given radial position. Figure 5.14 shows again the local measurements reploted in this way. As can be seen in the linear plot of figure 5.14 (a), the flow curves seem to be fairly linear, i.e. Newtonian, with an increasing viscosity, when moving away from the inner cylinder. The local viscosity versus radius relation can be found in figure 5.15. Again to compare this data with other measurements in the literature would require the concentration profile in the gap, so as to be able to give a concentration value for each of the locally inferred flow curves of figure 5.14. The bulk measurement seems to be in quite good agreement with the flow curve at radius r $\cong$ 17 mm.

The Newtonian behavior seems to break down in the outer wall region where the velocity profiles have significantly changed. Further investigation should be carried out in this region.

(a)

(b)

Figure 5.13: Concentrated particle suspension steady-state flow curve: lin-lin (a) and log-log plot (b)
The line-connected closed symbols represent the wall-slip-corrected bulk rheometric measurement using
different Couette-inversion techniques: Mooney (•) [204], Newton (•), power law (•), mid-point formula
(•) [86, 84], modified mid-point formula (•) [86, 84], quarter-point formula (•), three-eight-point formula
(•), modified first-term Krieger-Elrod formula (•) [86, 84], modified-quarter-point formula (•), modified-
three-eight-point formula (•), Krieger (1952) (•) [159], Krieger (1953) (•) [158], Krieger (1968) (•)
[163], Mac Sporran (•) [185], Tikhonov regualrization (•) [312], wavelette-vaguelette decomposition
(•) [12].
The unconnected symbols represent the local measurement, i.e. the flow curves derived from the steady-
state velocity profile at mid-height of the Couette cell: at 0.01 rad/s (×), 0.01802 rad/s (×), 0.03246
rad/s (×), 0.05848 rad/s (×), 0.1054 rad/s (×), 0.1898 rad/s (×), 0.342 rad/s (+), 0.6162 rad/s (+), 1.11
rad/s (+), 2.0 rad/s (+), 2.759 rad/s (+), 3.807 rad/s (+), 5.253 rad/s (∗), 7.248 rad/s (∗), and 10 rad/s
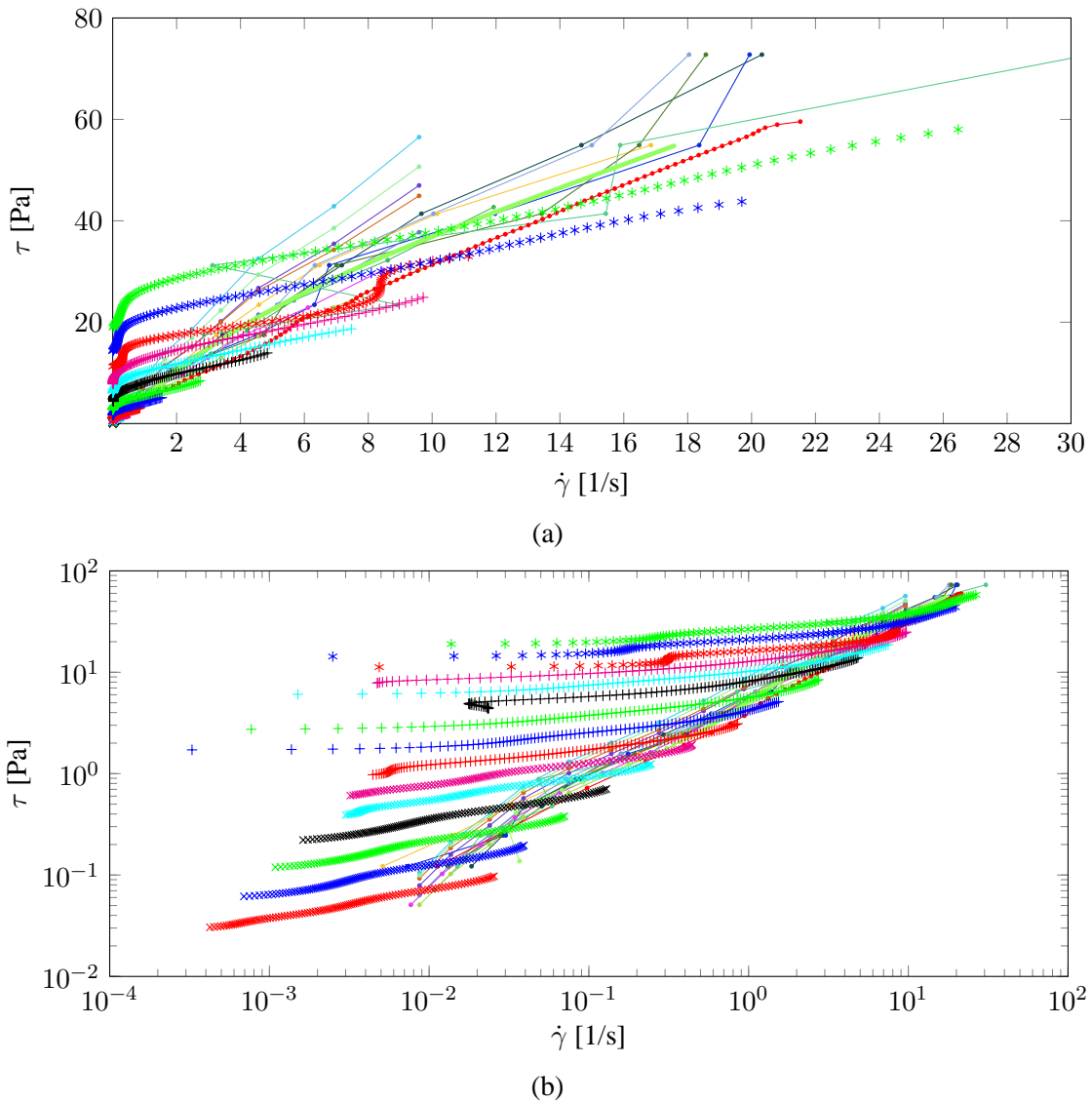(∗),

(a)

(b)
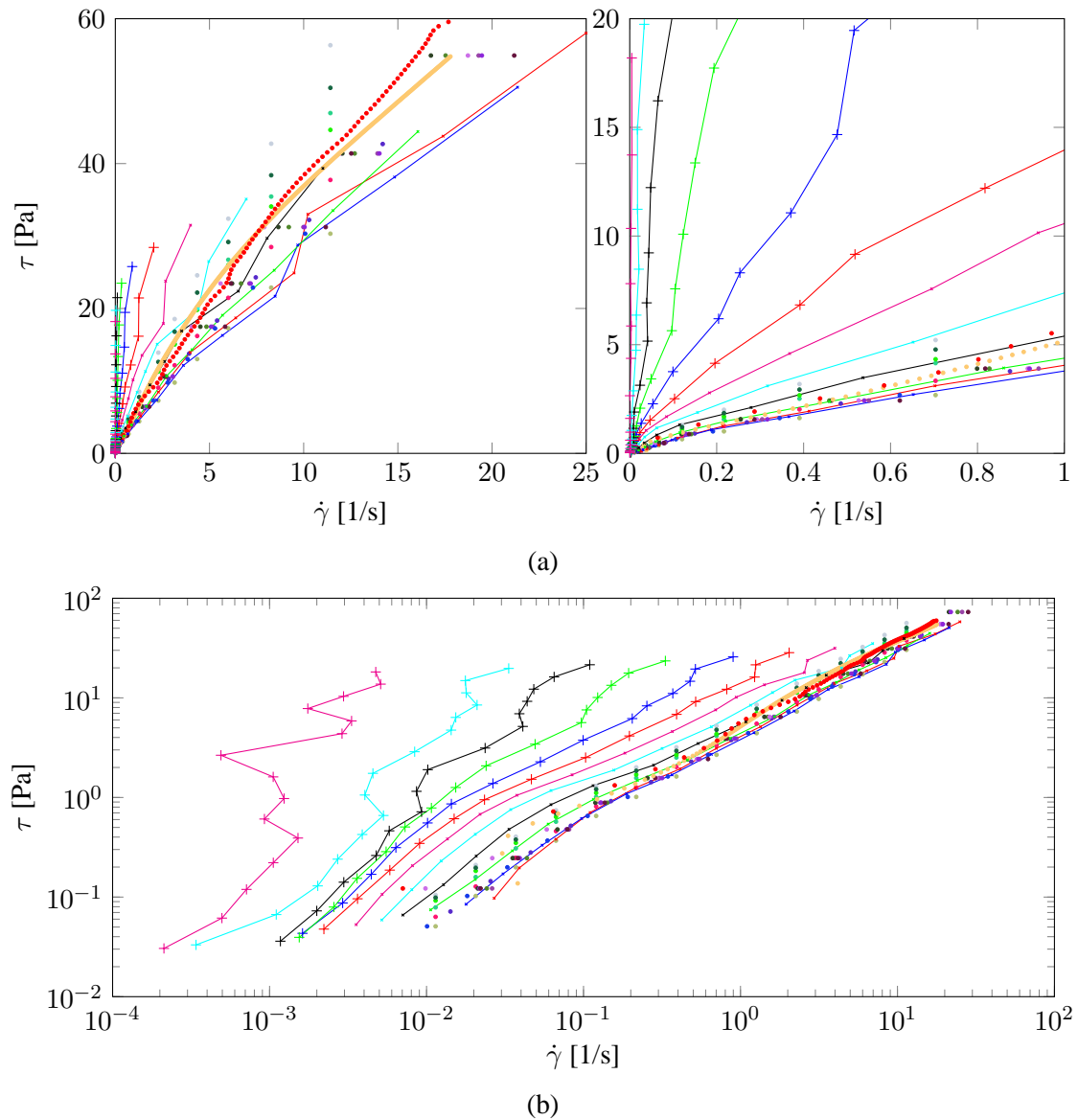
Figure 5.14: Corrected concentrated particle suspension steady-state flow curve: linear plot (a) and log-arithmic plot (b). The line-connected closed symbols represent the wall-slip-corrected bulk rheometric measurement using different Couette-inversion techniques: Mooney (•) [204], Newton (•), power law (•), mid-point formula (•) [86, 84], modified mid-point formula (•) [86, 84], quarter-point formula (•), three-eight-point formula (•), modified first-term Krieger-Elrod formula (•) [86, 84], modified-quarter-point formula (•), modified-three-eight-point formula (•), Krieger (1952) (•) [159], Krieger (1953) (•) [158], Krieger (1968) (•) [163], Mac Sporran (•) [185], Tikhonov regualrization (•) [312], wavelette-vaguelette decomposition (•) [12].

The line connected symbols are the locally inferred flow curve at several radii: at 14mm (×), 15 mm (×), 16 mm (×), 17 mm (×), 18 mm (×), 19 mm (×), 20 mm (+), 21 mm (+), 22 mm (+), 23 mm (+), 24 mm (+), and 25 mm (+)
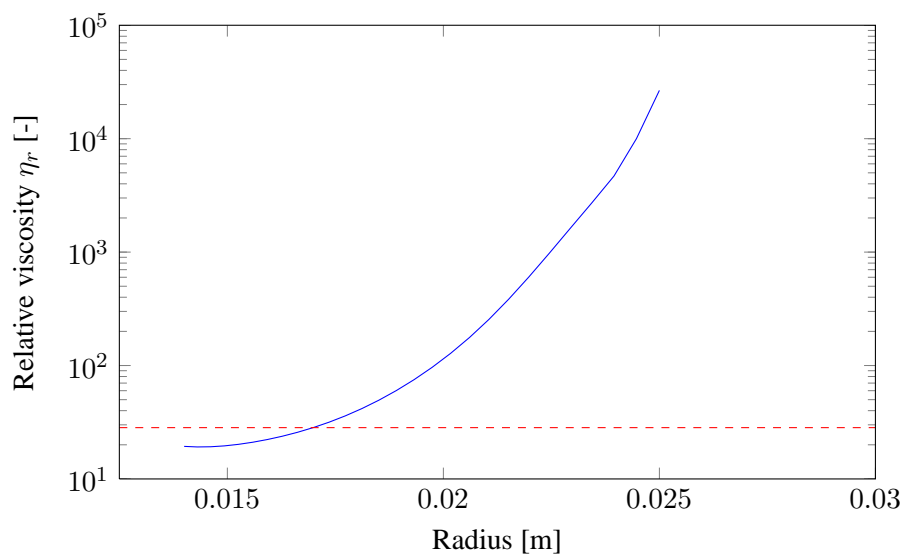
Figure 5.15: Relative viscosity distribution in the gap inferred from the local measurements (continuous line) and the dashed red line represent the bulk measurement viscosity (inner sand-blasted cylinder $\varnothing = 25$ mm, particle volume fraction $\phi = 0.55$).

5.4 Transient measurements: shear-induced particle diffusion process

As discussed in § 2.2 and § 2.3.2, shear-induced particle diffusion takes place within the gap in concentrated particle suspensions. As we will see, this process also affects wall slip in the transient regime (§ 5.4.1), the velocity profile within the gap and hence the inferred shear rate distribution (§ 5.4.2).

5.4.1 Wall slip

In our experiments, when starting from a homogeneous suspension, wall slip slowly reduces at the inner cylinder with the number of inner cylinder rotations, i.e. with the diffusion process. Figure 5.16 shows the inner slip velocity as a function of the number of inner-cylinder rotation. The last measurement taken after 3100 rotations corresponded to a steady state, i.e. when the measured torque at the inner cylinder reached an almost constant value. These measurements seem to be in agreement with the idea that slip decreases with local particle concentration. As shear-induced diffusion takes place and pushes the particle away from the inner cylinder, wall slip decays. It would tend to a no-slip condition if the local particle concentration would decrease further at the inner interface.

Figure 5.16: Inner cylinder wall slip: wall slip vs number of inner cylinder rotations
Values of the extrapolated inner slip velocity versus number of inner cylinder rotations. The velocities are adimensionalized with the inner cylinder velocity (inner sand-blasted cylinder $\varnothing = 25$ mm, particle volume fraction $\phi = 0.55$ and inner cylinder angular velocity $\Omega = 0.1$ rad/s).

As shown figure 5.17, a similar process takes place at the outer wall. With increasing number of inner cylinder rotation, the wall slip decreases as well, even if the local particle concentration increases. Therefore, the particle content cannot explain this phenomenon. It should, on the contrary, increase wall slip effects. Furthermore, as the steady-state measurements with various mean concentration showed it (see figure 5.7), an increasing mean concentration and thereby an increasing local concentration at the outer wall lowers outer-wall slip. Therefore particle concentration cannot be the sole process involved. Another assumption comes up by looking at the shear-rate evolution in the gap during the diffusion process. The shear-rate profile changes substantially as a result of particle migration. In the outer part of the gap, the shear rate at the end of the diffusion process is two orders of magnitude lower than the

value measured at the first times, whereas close to the inner cylinder, it remains approximately constant. Figure 5.18 shows 4 different shear-rate profiles after 50, 80 , 540 and 3100 inner cylinder revolutions.
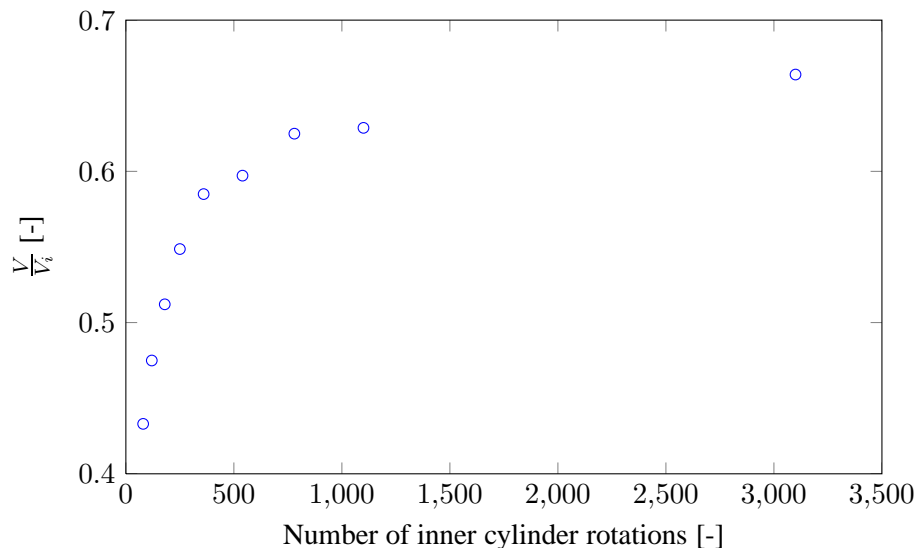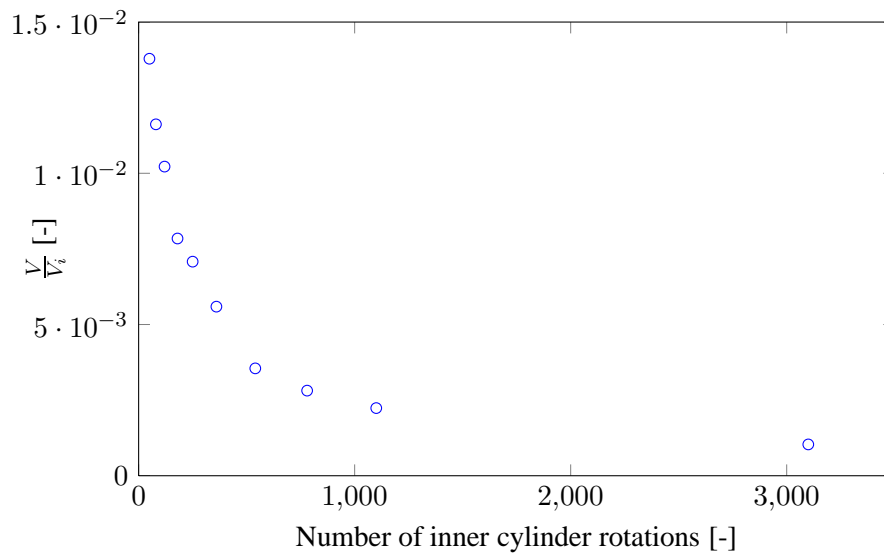

Figure 5.17: Outer cylinder wall slip: wall slip vs number of inner cylinder rotations
Value of the extrapolated outer slip velocity versus number of inner cylinder rotations. The velocities are adimensionalized with the inner cylinder velocity (inner sand-blasted cylinder $\varnothing = 25$ mm, particle volume fraction $\phi = 0.55$ and inner cylinder angular velocity $\Omega = 0.1$ rad/s).

5.4.2 Velocity profile

Our velocity field measurements highlighted strong changes in the azimuthal velocity profile within the gap during the shear-induced migration process. Figure 5.18 and 5.19 show the dimensionless velocity profiles after wall-slip correction for a concentrated suspension starting from a homogenous state with particle volume fraction of 0.55 and the corresponding inferred shear rate. For clarity, we plotted only part of the data (raw measurements can be found in appendix D on figure D.6, D.7, and D.8). During the shear-rate-induced particle diffusion process, the inner part of the velocity profile seems to change from a sub-exponential to a super-exponential, whereas in the outer part of the gap, a plug-like region develops. The super-exponential steady-state velocity profile seems to be, at least qualitatively, in agreement with the MRI measurements of Ovarlez *et al.* [229]. For the outer plug region and for the remaining transient measurements, to our knowledge, there is no other measurement in the literature to compare with.

As unfortunately we have not been able as yet to measure the concentration profile of the suspension in the gap, this transient measurement cannot be used to infer a flow curve of the sheared material. This also means that we have no way to compare these measurements with the steady-state ones, nor we can have a look at consistency between both measurements.

5.5 Normal stress or bottom-end effect

As shows figure 5.20 (a) for a suspension with particle volume fraction of 0.55 and sheared at 0.01 rad/s, the velocity profile does not seem to be influenced by the bottom end of the cell for flow depth in
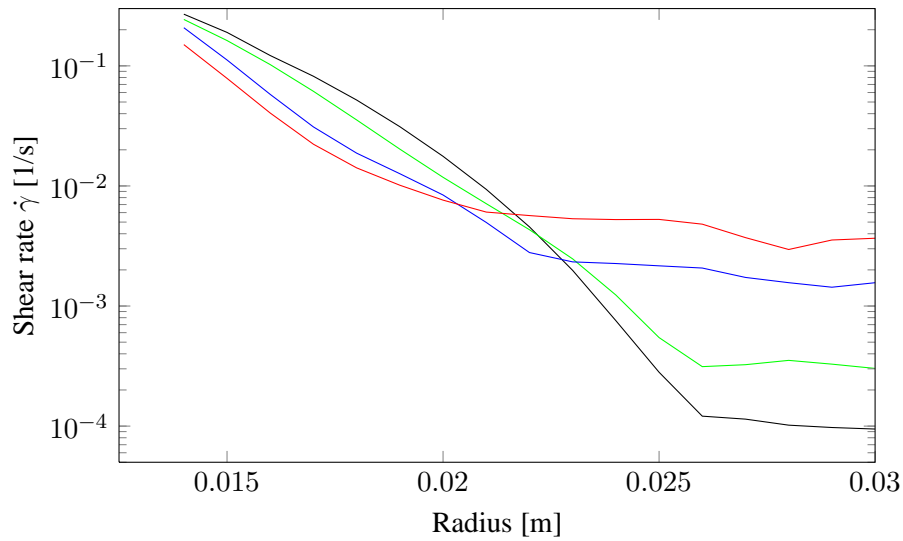
Figure 5.18: Shear rate evolution during the particle diffusion process: after 50 inner cylinder revolutions (–), 80 revolutions (–), 540 revolutions (–), and 3100 revolutions (–) (inner sand-blasted cylinder $\varnothing = 25$ mm, particle volume fraction $\phi = 0.55$ and inner cylinder angular velocity $\Omega = 0.1$ rad/s).

excess of 5 to 10 mm. This was checked for several angular velocities. However, if one does look at the logarithmic plot of figure 5.20 (b), the outer region velocity profiles seem to show greater slip velocity (at the outer wall) at deeper positions in the cell. The reason for this wall slip effect is not clear. It may result from normal stress effects, but this remains speculative. If one gets rid of inner and outer wall slip velocities, the profiles collapse on a single curve, as can be seen on figure 5.21.
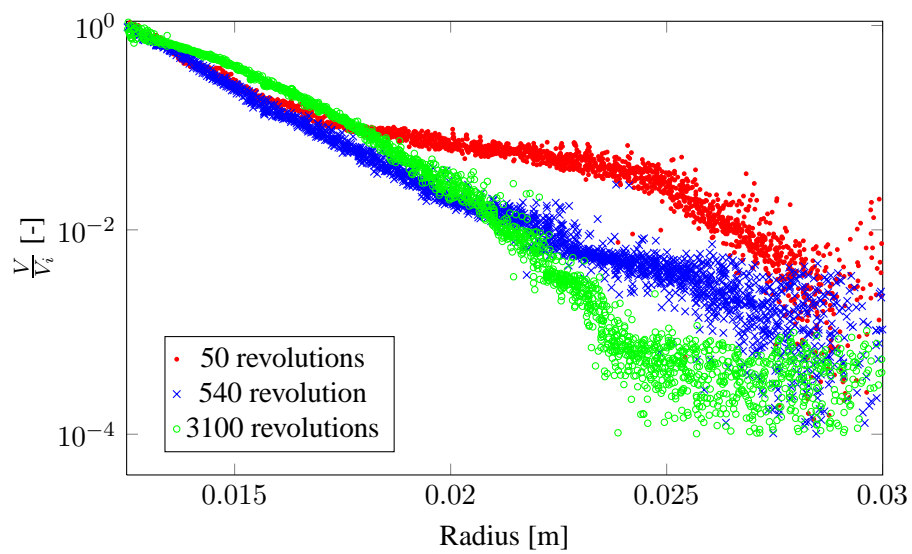
Figure 5.19: Dimensionless azimuthal velocity profile evolution: profile after 50 inner cylinder rotations (•), 540 rotations (×), 3100 rotations (∘) (inner sand-blasted cylinder $\varnothing = 25$mm, particle volume fraction $\phi = 0.55$, angular velocity $\Omega = 0.1$ rad/s).
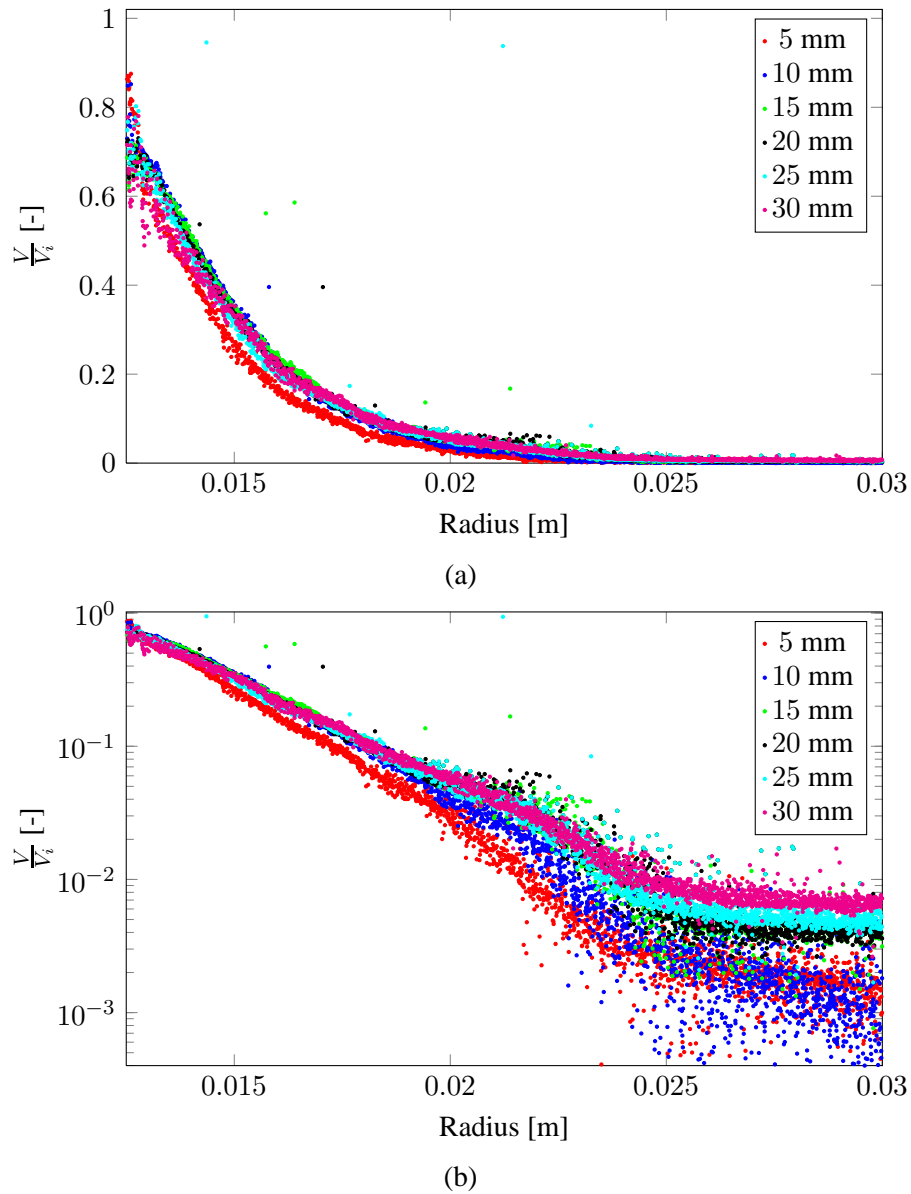
Figure 5.20: Linear plot (a) and logarithmic plot (b) of the dimensionless azimuthal velocity profile at several height in the gap: at 5 mm (•), 10 mm (•), 15 mm (•), 20 (•), 25 mm (•), and 30 mm (•) (inner sand-blasted cylinder $\varnothing = 25$ mm, particle volume fraction $\phi = 0.55$, angular velocity $\Omega = 0.01$ rad/s).
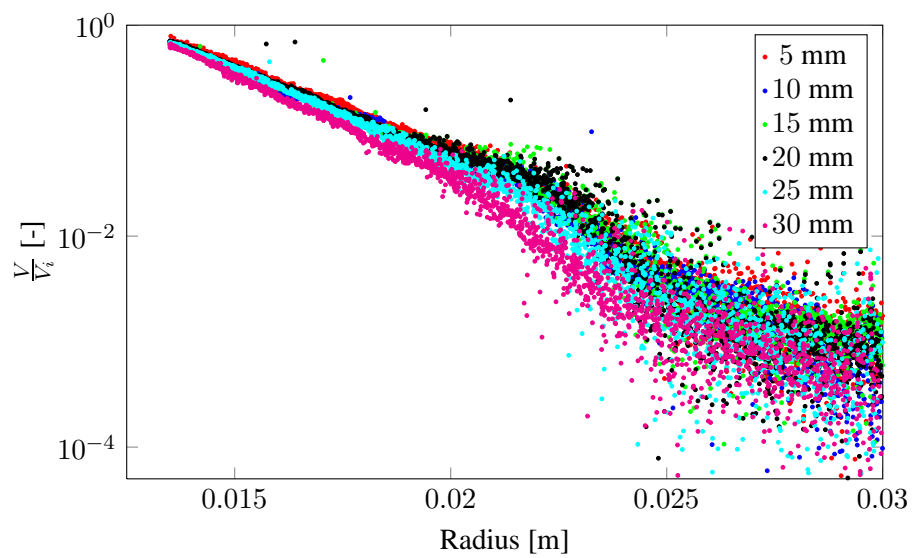
Figure 5.21: Logarithmic plot of the dimensionless wall-slip corrected azimuthal velocity profile at several height in the gap: at 5 mm (●), 10 mm (●), 15 mm (●), 20 (●), 25 mm (●), and 30 mm (●) (inner sand-blasted cylinder $\varnothing = 25$ mm, particle volume fraction $\phi = 0.55$, angular velocity $\Omega = 0.01$ rad/s).

6 Conclusion

The aim of this PhD thesis was to contribute to a better understanding of concentrated non-colloidal particle suspensions. We developed refractive-index-matching techniques, which allowed us to gain insight into their flow behavior. We performed experiments down to 35-mm depths (more than 350 particle-fluid interfaces to look through) and used suspensions with particle volume fraction as large as 60%. Combined to FPIV techniques, these techniques allowed us to get an improved time and spatial resolution compared to MRI technique, which have also been used for this kind of experiments.

With the help of this combined refractive-index-matched technique (developed at the Laboratoire d'Hydraulique Environnementale) as well as FPIV, I addressed different questions:

- Is it possible to obtain a reliable flow curve for concentrated particle suspensions from bulk measurements? And this by considering the wide shear range within the gap, the non-homogeneous material, and the inversion-technique problems due to the wide gap?

  Rheometric measurements of concentrated non-colloidal suspensions had to be taken in wide-gap geometries (because of the particle size). Comparison between bulk and local measurements has shown that all the Couette inversion methods average both (i) the fluid properties and (ii) the resulting flow behavior over the gap:

  i. as the particle concentration changes across the gap (a few percent), the fluid is no longer homogeneous and, for example in the viscous regime, the local viscosity can change by a factor of 10^5 over the gap;

  ii. as the shear rate in the gap spans orders of magnitude, the flow may undergo different flow regimes within the gap and therefore, inversion methods may not identify these regimes properly.

  Current sophisticated inversion techniques are able to solve the wide-gap effect satisfactorily. However, the point measurement of angular velocity and torque (Ω_i, T_i) at the inner (or outer) wall does not contain enough information and therefore these techniques cannot properly take effects (i) and (ii) into account. In the viscous regime, by accounting for particle migration and hence for the local viscosity and shear rate, one may improve the existing inversion techniques. However, this would relegate the inversion technique to a method using an *a priori* knowledge of the fluid behavior. This is unavoidable because of the lack of measured information. One has to keep in mind that there is no consensus on particle migration. Very accurate concentration-profile measurements should be carried out in transient (especially at the beginning) and steady-state regimes to obtain this *a priori* knowledge. And even if we were able to obtain such information, we would have to face many unclear points, e.g. how do particle size, size distribution, particle shape, surface roughness, etc, affect rheological properties?

97

- What are the main rheological properties of concentrated non-colloidal particle suspensions in the frictional and viscous regimes? What about the transition between these two regimes?

  Unfortunately, since to date, we are unable to accurately measure the concentration profile in the gap, part of the problem is still unsolved and we cannot give proper answers to these questions. Most measurements within the flow showed that the flow exhibited a viscous behavior. This could be anticipated since we worked with buoyant particles. Note that a thin region around the outer cylinder departed from this behavior. This region still underwent small deformation; it was therefore not a plug region slipping at the outer wall. This seems to provide evidence for another flow behavior of non-colloidal particle suspension, which differs significantly from the viscous regime. As it has been inferred from local measurements, this behavior cannot be related to the bulk-measured apparent frictional regime. However, since we used buoyant particles, we cannot exclude that this behavior reflects some plastic process. Further investigation should be carried out.

  Concerning the transition between these two regimes, all our local measurements have shown a kink in the velocity profiles (the thickness of the transition region is approximately the particle size). Therefore, there is apparently no region where both regime coexist.

Perspectives

In the present work, image processing techniques were chosen because of their spatial and time resolution. Once the refractive-index-matching technique is well harnessed, its versatility is an additional key advantage over other techniques to tackle problems in various geometries and transient applications related to concentrated particle suspensions. Our know-how was first developed within the laboratory for the Couette cell experiments presented in this thesis and is now being carried over to other flow geometries such as the dam-break experiment of concentrated particle suspensions.

- To improve the measurement technique for highly transient flows, e.g., during migration process in a Couette cell or when tracking the front wave in dam break experiments, we plan to combine refractive-index-matching techniques and time-resolved PIV using a high frame rate laser and camera. Figure 6.1 shows an image (side view) of the front of a dam-break flow in a flume.

- As we have seen in this work, the rheology and velocity field in concentrated particle suspensions are strongly affected by the local particle concentration. The next step to improve our understanding of concentrated non-colloidal particle suspensions is the particle-concentration measurement in these index-matched fluids.

Figure 6.1: Flow front (dam-break experiment) of a concentrated and refractive-index-matched suspension with a particle volume fraction of 0.55 and an inclination of 0 ˚ , images have been taken from the side at a depth of 20 mm into the fluid. The suspension flows from left to right and the bright dots are marked particles advected by the fluid, which are used as tracers to infer fluid velocity.

Refractive index matched fluid recipes

In this section, the reader will find other recipes used in the literature to match the refractive index of particles.

- PMMA (Polymethylmethacrylate)

    - Potassium thiocyanate solution [108]

    - Triton X100 (Sigma Aldrich) [138, 146]

    - Glycerin 40.67% by weight, ethylene glycol 22.82% by weight and styrene glycol 36.51% by weight [169]

    - Aqueous zinc iodide solution [127]

    - Kerosine and an oil mixture (Shellflex 214 BG) [36]

    - Demineralized water, zinc chloride [282]

    - Dow Corning fluid 550 84% by weight and Dow Corning fluid 556 16% by weight [38, 239, 254, 282]

    - Dow Corning fluid 550 and Dow Corning fluid 200 [142]

    - Dow Corning fluid 556 98% by weight and Dow Corning fluid 200 2% by weight [282]

    - Demineralized water, zinc chloride and Triton X100 (Sigma Aldrich) [39, 40, 41, 42, 166, 290]

    - 1,1,2,2 tetrabromoethane (Eastman Kodak) 14.07% by weight, polyalkylen glycol (UCON oil 75 H 90'000) 35.66% by weight, Triton X100 (Sigma Aldrich) 50.27% by weight and Tinuvin 328 (Ciba Specialty Chemicals) 0.1% by weigth [3, 22, 109, 201, 271]

    - Decahydronaphthalene, tetrahydronaphthalene and cyclohexylbromide [57, 107]

    - Decahydronaphthalene, tetrahydronaphthalene and carbon tetrachloride [150]

    - Decahydronaphthalene, tetrahydronaphthalene [6]

    - Cyclohexylbromide and decahydronaphthalene [88, 305, 307]

    - Cyclohexylbromide, decahydronaphthalene and tetrabutyl-ammonium chloride [148]

    - Polyalkylene glycol oil (UCON oil 50-HB-5100, Union Carbide) and 1,1,2,2 tetrabromoethane (Aldrich Chemical Company) [110]

    - Di-butylphtalate [313]

    - para-cymene [115, 116, 117, 122]

    - Tetraline and 40% by weigth turpentine [131, 146, 178, 179, 223, 225, 224, 288]

- – Polyglycol oil (UCON oil 50-HB-5100, Union Carbide) 33.7% by weight, terpineol 41.8% by weight, 1,1,2,2 tetrabromohethane (Aldrich Chemical Company)24.4% by weight and Tinuvin (Ciba Geigy) 0.1% by weight [203]

- – L42 organosilicone fluid (Union Carbide Co.) 27% by weight and 550 fluid (Dow chemical Co.) 73% by weight [92, 219, 220, 221]

- – Ethyl and benzyl alcohol [122]

- – Aqueous sodium iodide solution and glycerin [317]

- – Aqueous sodium iodide solution (60% concentration) [122, 227, 233, 299, 314]

- – 1,6 dibromohexane (Aldrich caltalogue no. D4,100-7), polyalkylen glycol (UCON oil 75 H 450) and Triton X100 (Sigma Aldrich) [181, 182]

- – Hexadecane and microscope oil (Sigma-Aldrich S150) [172, 173]

- – Aqueous solution of potassium thiocyanate and ammonium thiocyanate [46]

- – Tetrachloroethylene [145]

• PS (polystyrene)

- – 1-methylnaphtalene (Aldrich catalogue number M5,680-8), 1-chloronaphtalene (Aldrich C5,765-0), polyalkylene glycol (UCON oil 75-H-90'000, Dow Chemicals Co.) [154, 155]

- – 1-methylnaphtalene 28% by volume, 1-chloronaphtalene 31% by volume and tetraline 41 % by volume [77]

• PVA (Polyvinyl alcetate)

- – Polyglycol oil (UCON oil 50-HB-5100, Union Carbide) and 4% by volume tetrabromo-hethane [147]

• Nylon

- – Pale 4 oil (oxidized castor oil, Baker Castor oil Co.) and tetrabromoethane [147]

• Glass

- – Glycerine and water [231]

- – Soddard solvent and mineral oil [231]

- – Glycerol [53, 207]

- – Esso Marcol 82 and Primol 352 [261, 262]

- – Dow Corning fluid 550 and Dow Corning fluid 556 [304, 311]

- – Oil (Pharma 5, DEA) and a light protective liquid (Eusolex, Merck) [156]

- – Tetrechloroethylene and Freon113 [302]

- – Methylbenzoate at 25°C [320]

- – Light fuel oil and 30% by volume of palatinol C [91]

- – Xylen and 44% by volume and Varsol [100]

- – Tetralin and silicone oil in proportion (1:2.57, by weight) [58, 199, 200]

- – Alkyl benzyl phthalate plasticizer, named Santicizer 278 and produced by Monsanto [118, 215, 216, 217]

- – Isopropyl alcohol and methylnaphthalene [122]

- – Diethylphthalate [122]

- – Sodium Iodide water solution (55% by weight) [60, 136, 195, 284]

- – Tetralin and clear coal oil [315]

- Silica gel

  - – Chloroform and water [2]

  - – Water solution of sodium iodide (50%) [59, 60, 61, 144, 211, 309]

  - – Benzyl alcohol 45% by volume and ethyl alcohol 55% by volume [77]

- Fused quartz

  - – Tertaethylene glycol [279]

  - – Tetrahydropyran-2-methanol [279]

  - – Cyclooctane and cyclooctene [279]

- Other

  - – Silicon rubber with methylcylohexane and water glycerin mixture [48]

  - – Glycerol and potassium dihydrogen phosphate (monobasic) [9]

  - – Ethanol and Epsom salt solutions [20]

  - – Sugar and Epsom salt as solutes in water [191]

  - – Ethyl alcohol and salt (NaCl) [83, 119, 120]

  - – Fluoropolymer (FEP) was tested in water [122]

  - – Sucrose-water continuous phase; trichlorotrifluoroethane-1- octanol droplet phase liquid-liquid system [45, 47]

  - – n-heptane and 50% water glycerol mixture [21]

  - – silicone oil and a water glycerol mixture [218]

B

PIV pattern images and image correlation

The main equations used in the following are token from Raffel 2007 [252].

Image intensity field of PIV images

A typical PIV image intensity field can be written as:

$$I = I(\mathbf{X}, \mathbf{\Gamma}) = \tau(\mathbf{X}) * \sum_{i=1}^{N} V_0(\mathbf{X_i})\delta(\mathbf{X} - \mathbf{X_i})$$

$$= \sum_{i=1}^{N} V_0(\mathbf{X_i})\tau(\mathbf{X} - \mathbf{X_i})$$

with

- $\mathbf{X}_i$ is the ith particle position,

- $\mathbf{\Gamma}$ describes the state of the particle ensemble at a given time t,

- $V_0(\mathbf{X_i})$ is the transfer function giving the light energy of an individual particle i inside the interrogation volume V_I and its conversion into an electronic signal,

    - $V_0(\mathbf{X_i}) = W_0(X, Y)I_0(Z)$
    - I_0 is the intensity profile of the laser sheet (typically gaussian or almost constant if the laser beam intensity profile is a top-hat beam)
    - $W_0(X, Y) = \begin{cases} W_{xy} & \text{if the particle is inside of the laser sheet} \\ 0 & \text{if outside} \end{cases}$

- $\tau(\mathbf{X})$ is the intensity transmissivity point spread function of the photograph (commonly token as gaussian in the literature),

- $\delta(\mathbf{X} - \mathbf{X_i})$ is the Dirac function.

Correlation

Autocorrelation

$$
\begin{aligned}
R_I(\mathbf{s}, \mathbf{\Gamma}) &= \; <I(\mathbf{X}, \mathbf{\Gamma})I(\mathbf{X} + \mathbf{s}, \mathbf{\Gamma})) > \\
&= \; \frac{1}{a_I} \int_{a_I} \sum_{i=1}^{N} V_0(\mathbf{X_i})\tau(\mathbf{X} - \mathbf{X_i}) \sum_{j=1}^{N} V_0(\mathbf{X_j})\tau(\mathbf{X} - \mathbf{X_j} + \mathbf{s})d\mathbf{X} \\
&= \; \underbrace{\frac{1}{a_I} \sum_{i \neq j}^{N} V_0(\mathbf{X_i})V_0(\mathbf{X_j}) \int_{a_I} \tau(\mathbf{X} - \mathbf{X_i})\tau(\mathbf{X} - \mathbf{X_j} + \mathbf{s})d\mathbf{X}}_{R_C(\mathbf{s},\mathbf{\Gamma})+R_F(\mathbf{s},\mathbf{\Gamma})} \\
&\quad \underbrace{+\frac{1}{a_I} \sum_{i=j}^{N} V_0^2(\mathbf{X_i}) \int_{a_I} \tau(\mathbf{X} - \mathbf{X_i})\tau(\mathbf{X} - \mathbf{X_j} + \mathbf{s})d\mathbf{X}}_{R_P(\mathbf{s},\mathbf{\Gamma})}
\end{aligned}
$$

(B.1)

with

- $<I(\mathbf{X}, \mathbf{\Gamma})> = \frac{1}{a_I} \int_{a_I} I(\mathbf{X}, \mathbf{\Gamma})d\mathbf{X}$, the spatial average,

- $\mathbf{s}$ the separation vector in the correlation plan,

- a_I the interrogation area.

$R_C(\mathbf{s}, \mathbf{\Gamma})$ can be viewed as the convolution of the mean intensities, $R_F(\mathbf{s}, \mathbf{\Gamma})$ the fluctuating noise component from the i≠j terms and $R_P(\mathbf{s}, \mathbf{\Gamma})$ the self correlation peak located at (0,0) in the correlation plane.

Cross-correlation of 2 images

$$
\begin{aligned}
I(\mathbf{X}, \mathbf{\Gamma}) &= \; \sum_{i=1}^{N} V_0(\mathbf{X_i})\tau(\mathbf{X} - \mathbf{X_i}) \text{ and } I'(\mathbf{X}, \mathbf{\Gamma}') = \sum_{j=1}^{N} V_0(\mathbf{X_j})\tau'(\mathbf{X} - \mathbf{X_j}) \\
R_I(\mathbf{s}, \mathbf{\Gamma}, \mathbf{\Gamma}') &= \; <I(\mathbf{X}, \mathbf{\Gamma})I(\mathbf{X} + \mathbf{s}, \mathbf{\Gamma}')) > \\
&= \; \frac{1}{a_I} \sum_{i,j}^{N} V_0(\mathbf{X_i})V_0(\mathbf{X_j}) \int_{a_I} \tau(\mathbf{X} - \mathbf{X_i})\tau'(\mathbf{X} - \mathbf{X_j} + \mathbf{s})d\mathbf{X}
\end{aligned}
$$

Raw viscosity measurements
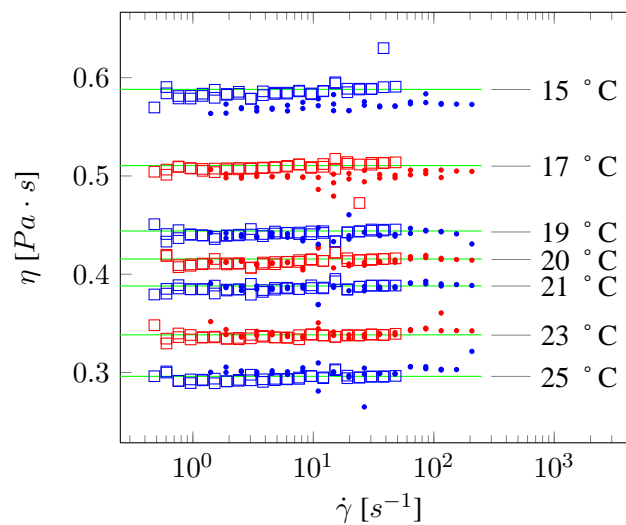
(a)
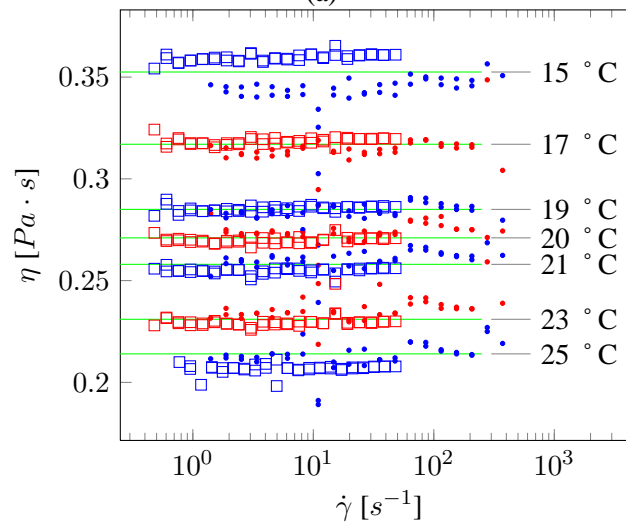
(b)

Figure C.1: (a) Raw viscosity measurement at various temperature of Triton X-100 (bottom-end effect corrected), (b) Raw viscosity measurement at various temperature of UCON oil 75-H450 (bottom-end effect corrected), (c) Raw viscosity measurement at various temperature of 1,6 dibromohexane (bottom-end not effect corrected) (closed circles are cone-plate (CP) measurement ($\varnothing$40 mm and 4 $^\circ$) and open squares are bottom-end corrected concentric cylinder measurements ($\varnothing$33 - 37 mm and 25 - 27.5 mm))

(c)

Figure C.1: (a) Raw viscosity measurement at various temperature of Triton X-100 (bottom-end effect corrected), (b) Raw viscosity measurement at various temperature of UCON oil 75-H450 (bottom-end effect corrected), (c) Raw viscosity measurement at various temperature of 1,6 dibromohexane (bottom-end not effect corrected) (closed circles are cone-plate (CP) measurement ($\varnothing$40 mm and 4 $^\circ$) and open squares are bottom-end corrected concentric cylinder measurements ($\varnothing$33 - 37 mm and 25 - 27.5 mm))
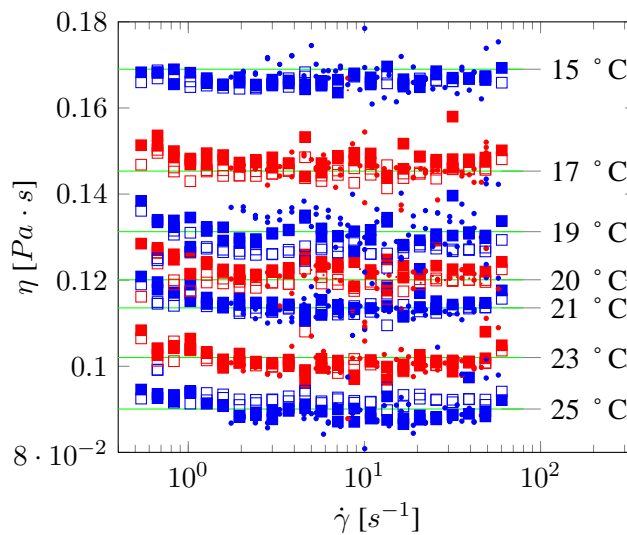
Figure C.2: Raw viscosity measurement at various temperature of the ternary mixture of Triton X-100, UCON oil 75-H450 and 1,6 dibromohexane (closed circles are cone-plate (CP) measurement ($\varnothing$40 mm and 4 $^\circ$) and squares are bottom-end corrected concentric cylinder measurements ($\varnothing$33 - 37 mm (open squares) and 25 - 27.5 mm filled squares)))
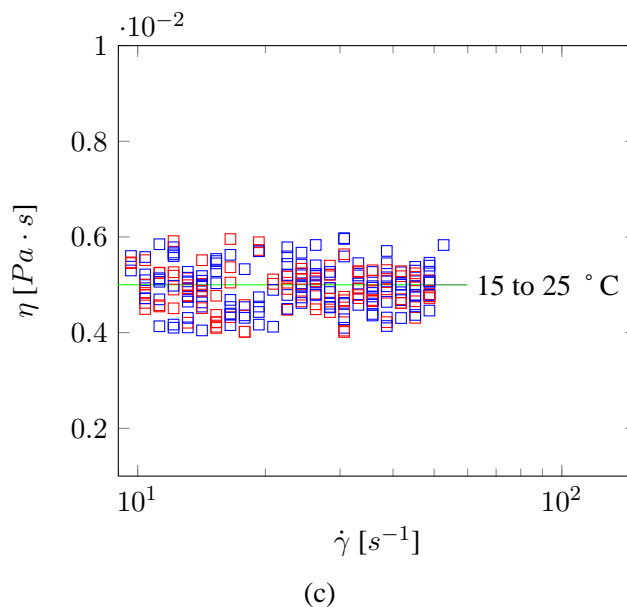
Raw velocity profiles

D.1 Wall slip

D.1.1 Inner cylinder wall slip vs angular velocity

Figure D.1: Inner cylinder wall slip: impact of the inner cylinder velocity

Dimensionless azimuthal velocity profile at several inner cylinder velocities: 0.01 rad/s (●), 0.01802 rad/s (●), 0.03246 rad/s (●), 0.05848 rad/s (●), 0.1054 rad/s (●), 0.1898 rad/s (●), 0.342 rad/s (×), 0.6162 rad/s (×), 1.11 rad/s (×) , 2 rad/s (×), and 10 rad/s (×). The extrapolated inner cylinder slip velocity (solid lines) are shown on figure 5.6. For clarity in the figure we removed the data that are influenced by the presence of inner cylinder wall in the data processing algorithms. The velocities are adimensionalized with the inner cylinder velocities (inner sand-blasted cylinder $\varnothing = 25$mm, particle volume fraction $\phi = 0.55$).

D.1.2   Outer cylinder wall slip vs angular velocity
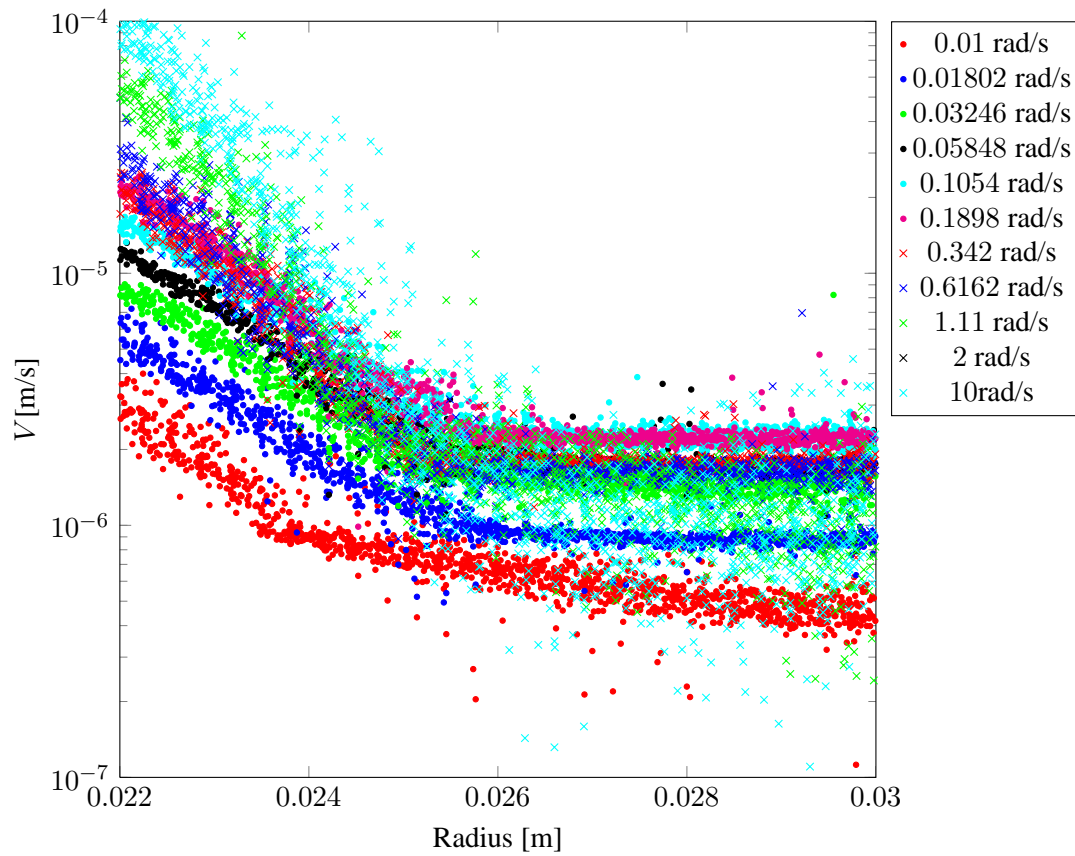
Figure D.2: Outer cylinder wall slip: impact of the inner cylinder velocity
Azimuthal velocity profile at several inner cylinder velocities: 0.01 rad/s (•), 0.01802 rad/s (•), 0.03246 rad/s (•), 0.05848 rad/s (•), 0.1054 rad/s (•), 0.1898 rad/s (•), 0.342 rad/s (×), 0.6162 rad/s (×), 1.11 rad/s (×) , 2 rad/s (×), and 10 rad/s (×)(inner sand-blasted cylinder $\varnothing = 25$mm, particle volume fraction $\phi = 0.55$).
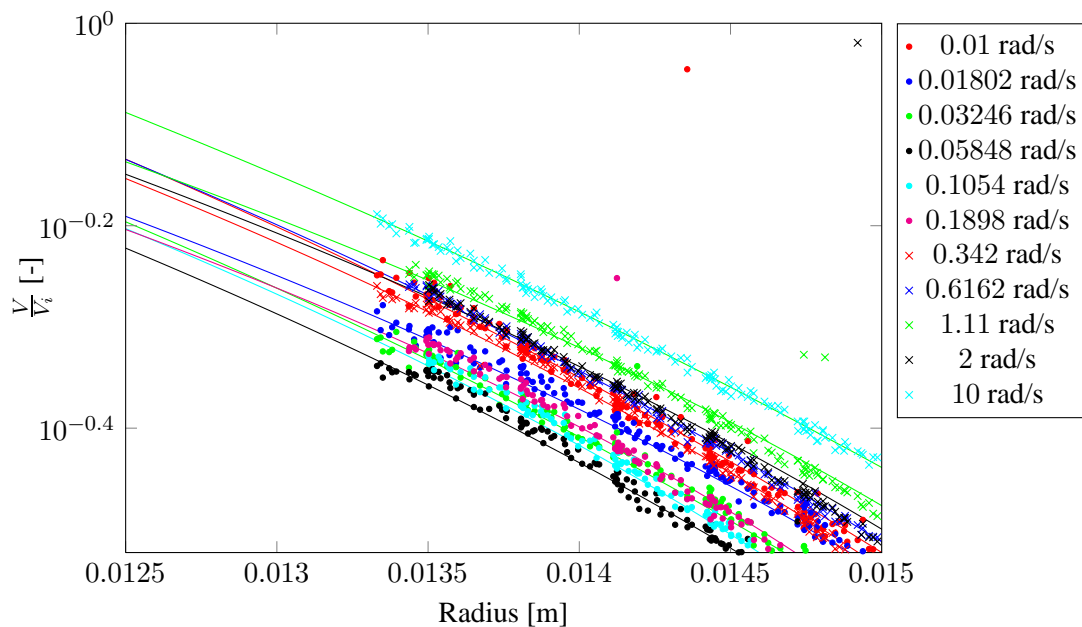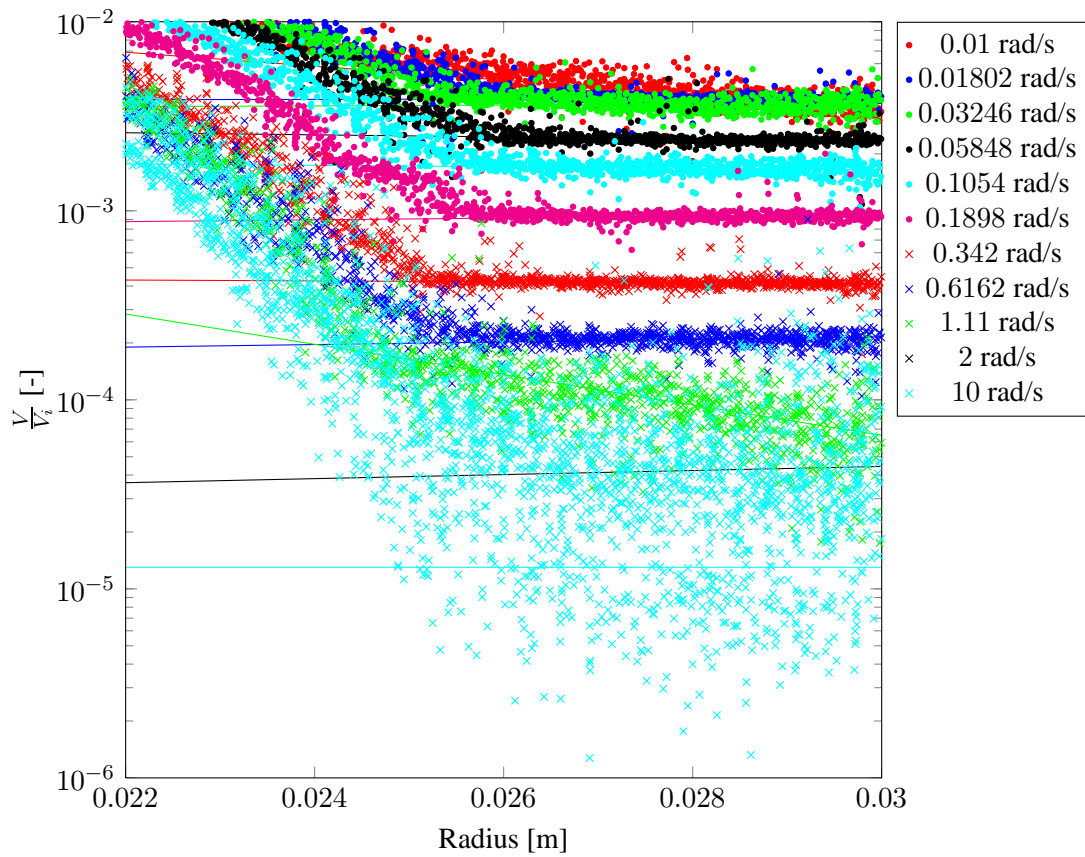
Figure D.3: Outer cylinder wall slip: impact of the inner cylinder velocity
Dimensionless azimuthal velocity profile at several inner cylinder velocities and its impact on the outer cylinder wall slip: at 0.01 rad/s (●), 0.01802 rad/s (●), 0.03246 rad/s (●), 0.05848 rad/s (●), 0.1054 rad/s (●), 0.1898 rad/s (●), 0.342 rad/s (×), 0.6162 rad/s (×), 1.11 rad/s (×) , 2 rad/s (×), and 10 rad/s (×). The extrapolated outer cylinder slip velocity (solid lines) are shown on figure 5.7. The velocities are adimensionalized with the inner cylinder velocities (inner sand-blasted cylinder $\varnothing = 25$mm, particle volume fraction $\phi = 0.55$).

D.1.3   Shear induced particle diffusion
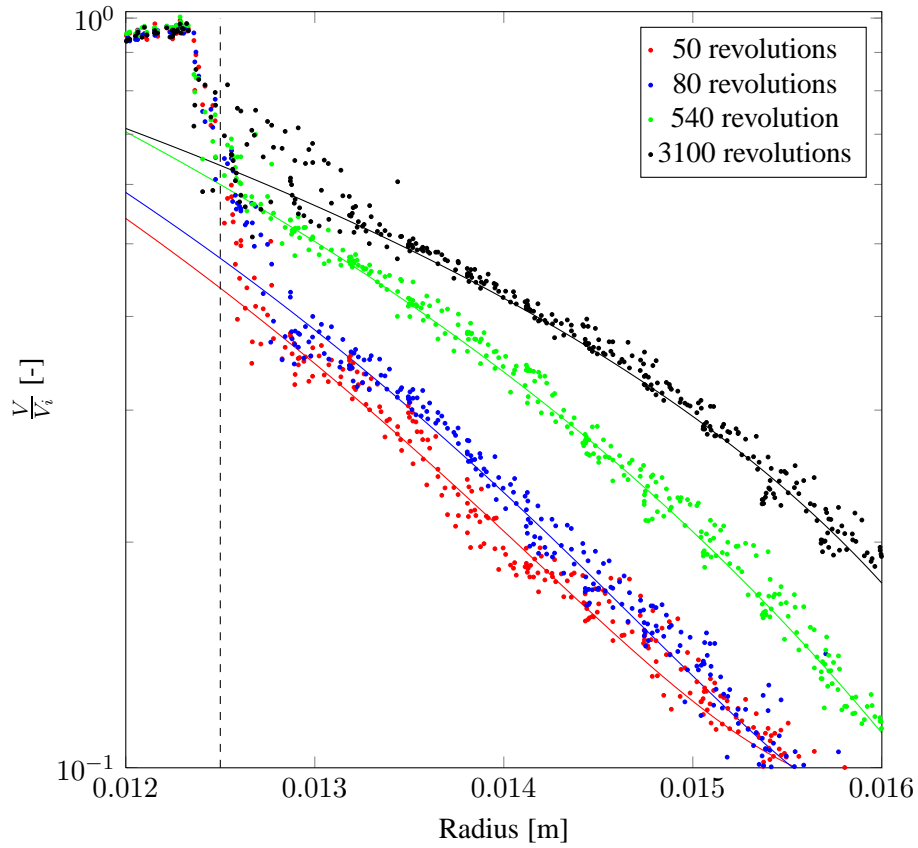
Figure D.4: Inner cylinder wall slip: impact of shear induced particle migration (starting with an homogeous sample)

Dimensionless azimuthal velocity profile next to the inner cylinder: profile after 50 inner cylinder rotations (●), 80 rotations (●), 540 rotations (●), 3100 rotations (●). The extrapolated apparent suspension velocities at the inner cylinder (solid lines) are shown on figure 5.16. The vertical dashed line represent the inner cylinder surface position (sand-blasted inner cylinder, $\varnothing = 25$mm, particle volume fraction $\phi = 0.55$, angular velocity $\Omega = 0.1$ rad/s).
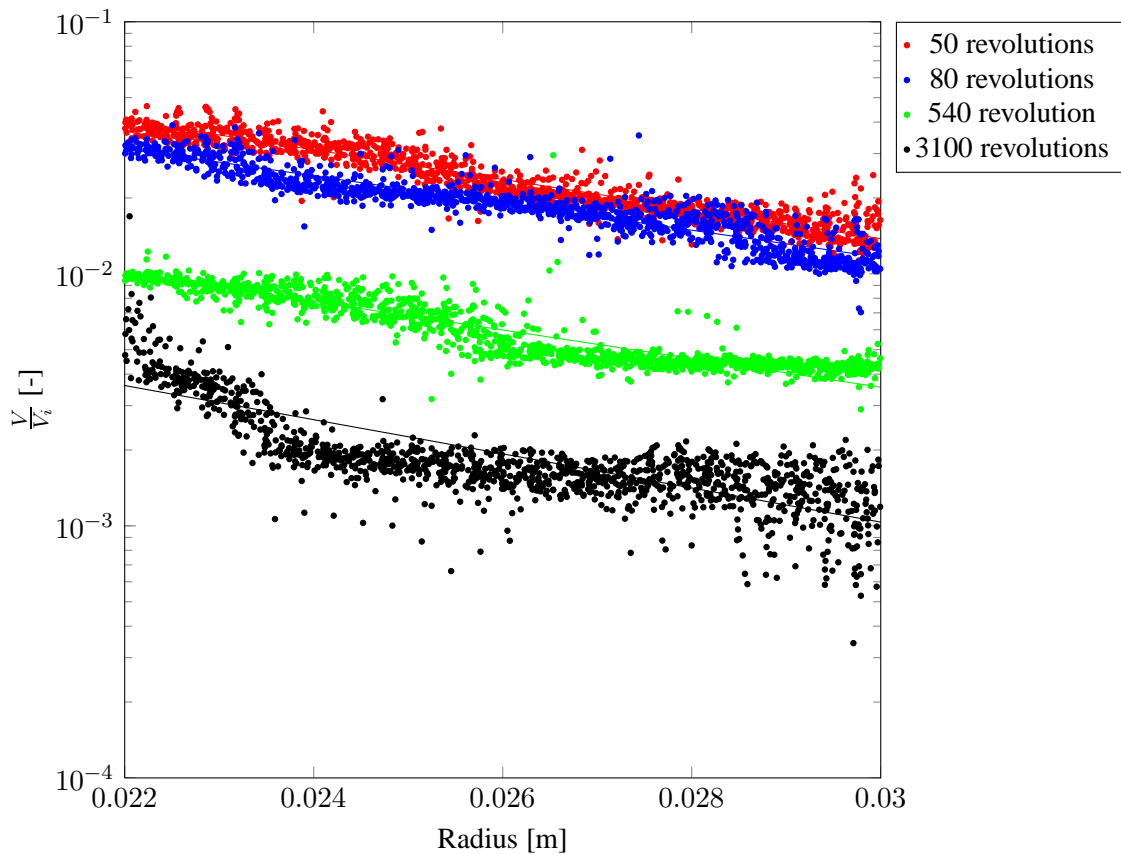
Figure D.5: Outer cylinder wall slip: impact of shear induced particle migration (starting with an homogeous sample)

Dimensionless azimuthal velocity profile next to the outer cylinder: profile after 50 inner cylinder rotations (•), 80 rotations (•), 540 rotations (•), 3100 rotations (•). The extrapolated apparent suspension velocity at the outer cylinder (solid lines) are shown on figure 5.17(sand-blasted inner cylinder, $\varnothing = 25$mm, particle volume fraction $\phi = 0.55$, angular velocity $\Omega = 0.1$ rad/s).

D.2   Shear induced particle diffusion

(a)

(b)
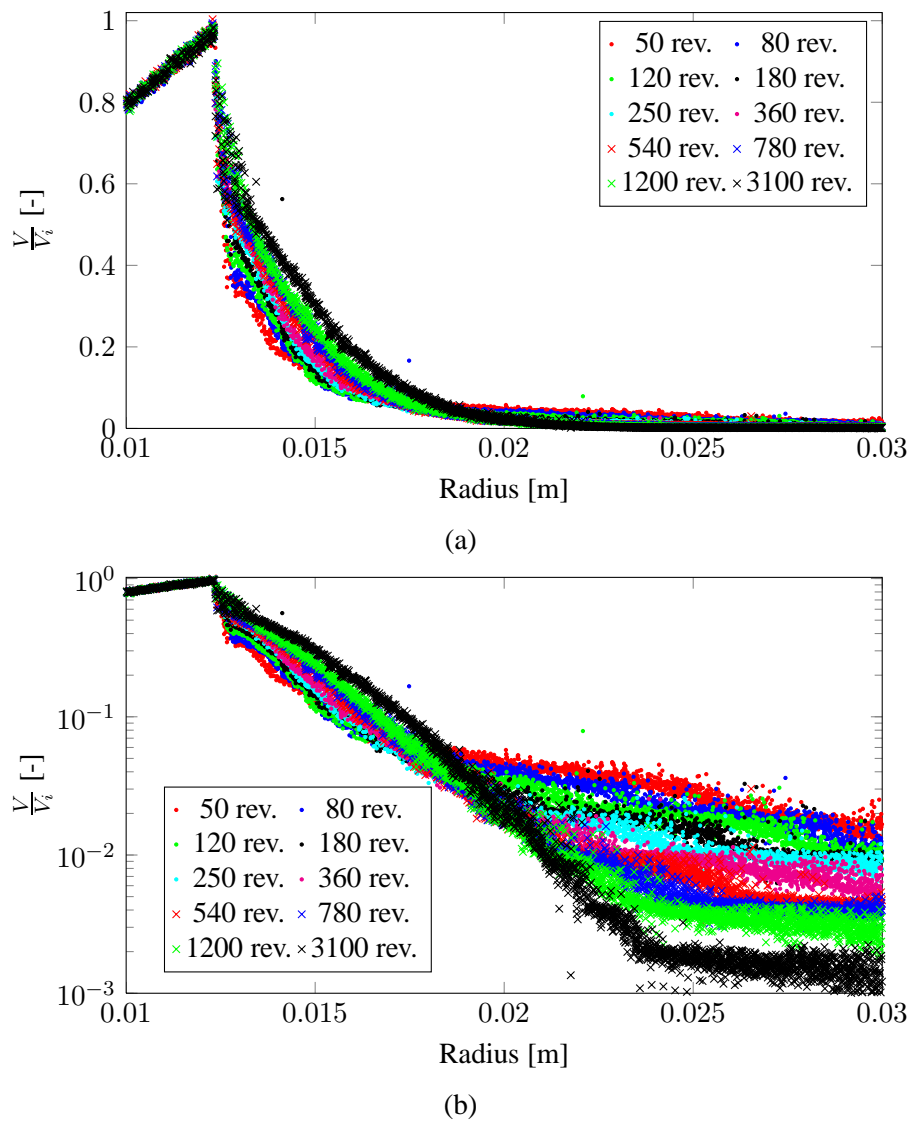
Figure D.6: Dimensionless azimuthal velocity profile evolution: (a) linear plot, (b) semi-logarithmic plot of the profiles after 50 inner cylinder rotations (●), 80 rotations (●), 120 rotations (●), 180 rotations (●), 250 rotations (●), 360 rotations (●), 540 rotations (×), 780 rotations (×), 1200 rotations (×) ,and 3100 rotations (×) (inner sand-blasted cylinder $\varnothing = 25$mm, particle volume fraction $\phi = 0.55$, angular velocity $\Omega = 0.1$ rad/s).
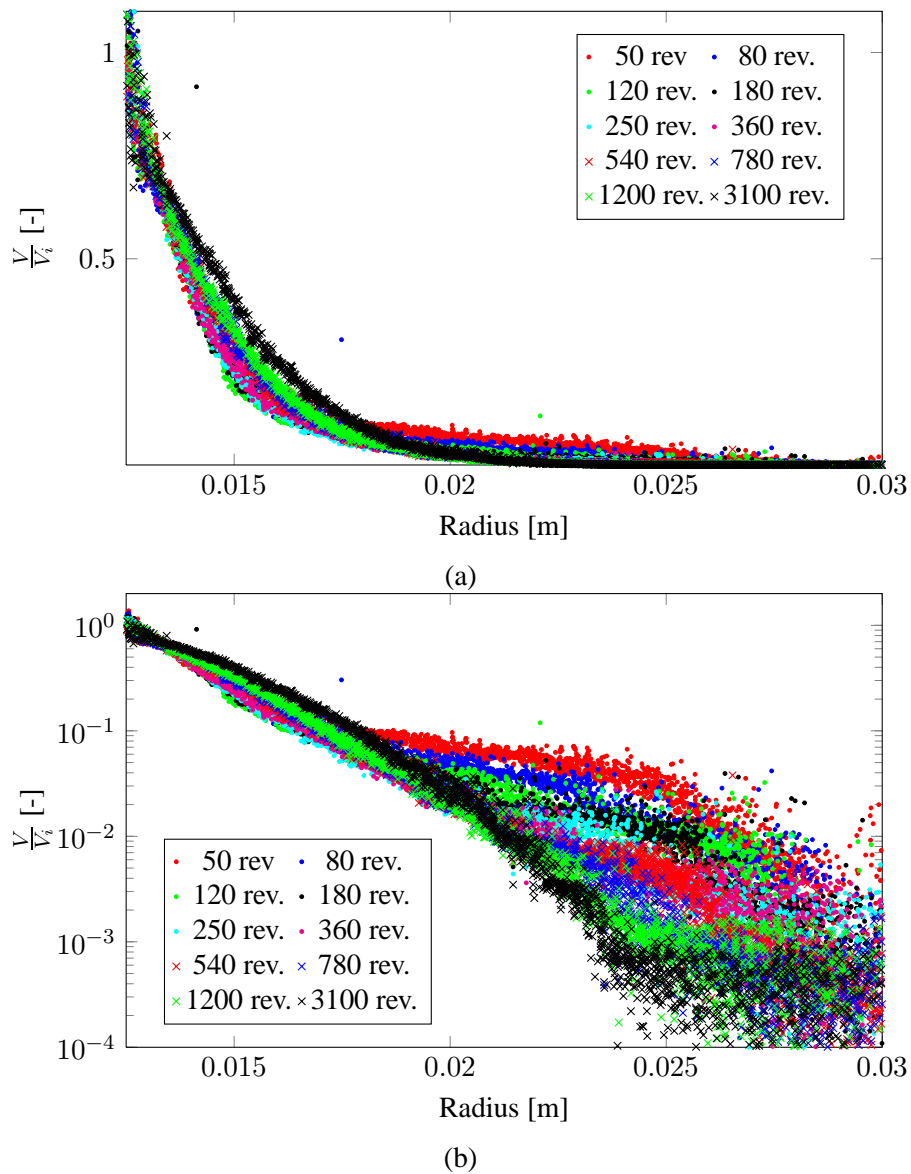
Figure D.7: Dimensionless wall-slip-corrected azimuthal velocity profile evolution: (a) linear plot, (b) semi-logarithmic plot of the profiles after 50 inner cylinder rotations (●), 80 rotations (●), 120 rotations (●), 180 rotations (●), 250 rotations (●), 360 rotations (●), 540 rotations (×), 780 rotations (×), 1200 rotations (×) ,and 3100 rotations (×) (inner sand-blasted cylinder $\varnothing = 25$mm, particle volume fraction $\phi = 0.55$, angular velocity $\Omega = 0.1$ rad/s).
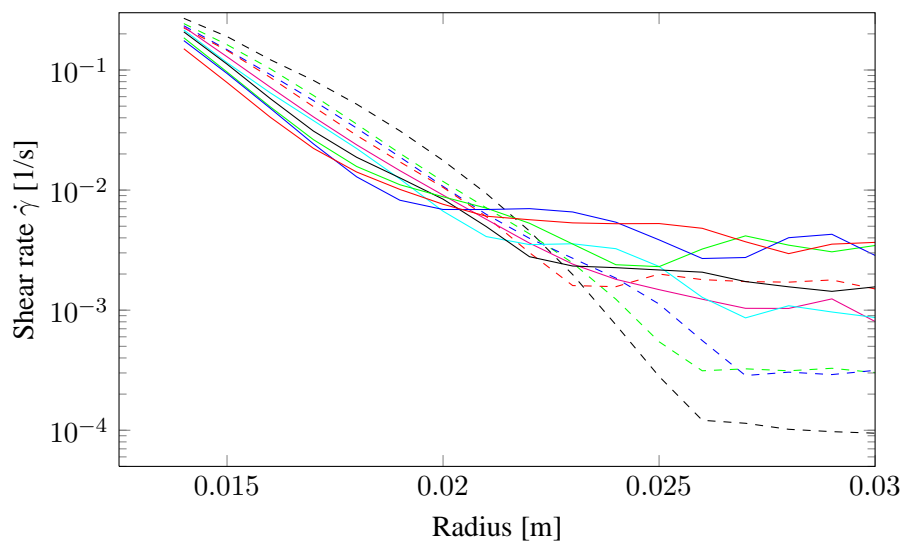
Figure D.8: Shear rate evolution during the particle diffusion process: after 50 inner cylinder revolutions (–), 80 revolutions (–), 120 revolutions (–), 180 revolutions (–), 250 revolutions (–), 360 revolutions (–), 540 revolutions (- -), 780 revolutions (- -), 1100 revolutions (- -), and 3100 revolutions (- -), (inner sand-blasted cylinder $\varnothing = 25$mm, particle volume fraction $\phi = 0.55$).

D.3 Steady velocity Profiles

(a)

(b)
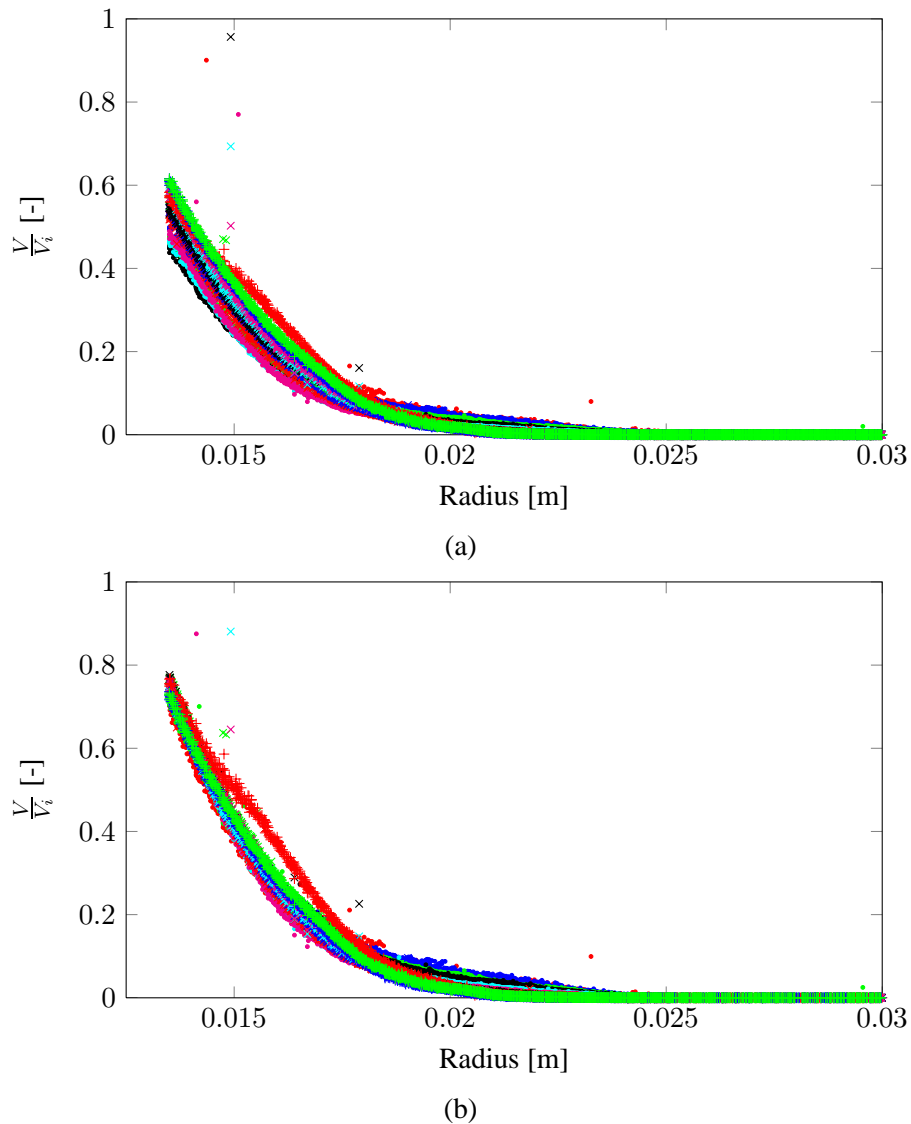
Figure D.9: Linear plot of wall-slip uncorrected (a) and corrected (b) dimensionless azimuthal velocity profile at several inner cylinder velocities: 0.01 rad/s (●), 0.01802 rad/s (●), 0.03246 rad/s (●), 0.05848 rad/s (●), 0.1054 rad/s (●), 0.1898 rad/s (●), 0.342 rad/s (×), 0.6162 rad/s (×), 1.11 rad/s (×), 2 rad/s (×), 2.759 rad/s (×), 3.807 rad/s (×), 5.253 rad/s (+), 7.248 rad/s (+), and 10 rad/s (+). The velocities are adimensionalized with the inner cylinder velocities (inner sand-blasted cylinder $\varnothing = 25$mm, particle volume fraction $\phi = 0.55$).

(a)

(b)
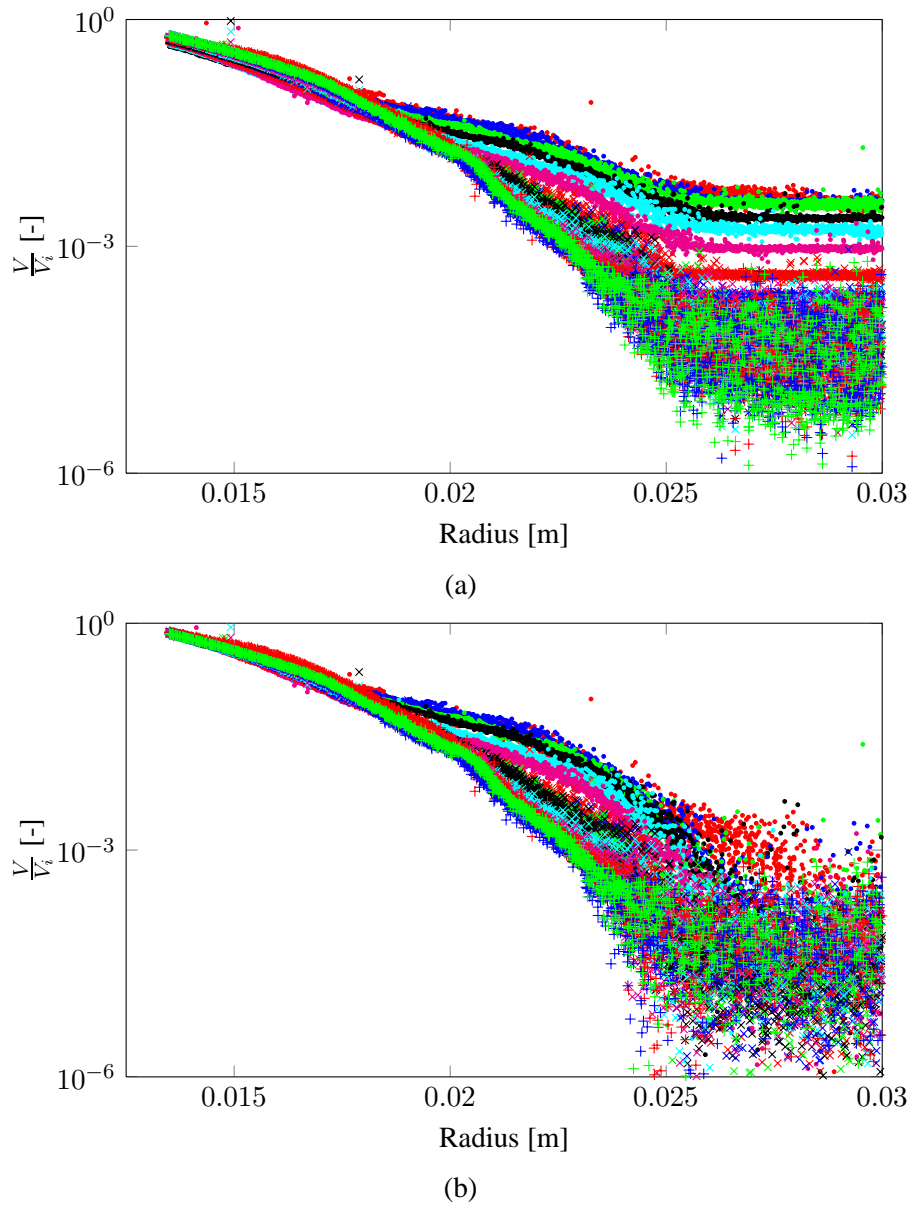
Figure D.10: Logarithmic plot of wall-slip uncorrected (a) and corrected (b) dimensionless azimuthal velocity profile at several inner cylinder velocities: 0.01 rad/s (●), 0.01802 rad/s (●), 0.03246 rad/s (●), 0.05848 rad/s (●), 0.1054 rad/s (●), 0.1898 rad/s (●), 0.342 rad/s (×), 0.6162 rad/s (×), 1.11 rad/s (×), 2 rad/s (×), 2.759 rad/s (×), 3.807 rad/s (×), 5.253 rad/s (+), 7.248 rad/s (+), and 10 rad/s (+). The velocities are adimensionalized with the inner cylinder velocities (inner sand-blasted cylinder $\varnothing = 25$mm, particle volume fraction $\phi = 0.55$).

Bibliography

[1] "Kodak kai-2020/kai-2001 ccd timing specification version 1.1 evaluation board kit 4h0691," Kodak (2005).

[2] Abbas, M. A. and C. T. Crowe, "Experimental study of the flow properties of a homogenous slurry near transitional reynolds numbers," International Journal of Multiphase Flow **13**, 357–364 (1987), 0301-9322 doi: DOI: 10.1016/0301-9322(87)90054-1.

[3] Abbott, J., L. Mondy, A. Graham and H. Brenner, "Techniques for analysing the behaviour of concentrated suspensions," in *Particulate two-Phase flow*, ed. M. Roco, pp. 3–32, Butterworth-Heinemann (1993).

[4] Abbott, J., N. Tetlow, A. Graham, S. Altobelli, E. Fukushima, L. Mondy and T. Sephens, "Experimental observations of particle migration in concentrated suspensions : Couette flow," Journal of Rheology **35**, 773–795 (1991).

[5] Ackermann, N. L. and H. T. Shen, "Rheological characteristics of solid-liquid mixtures," Aiche Journal **25**, 327–332 (1979).

[6] Ackerson, B. J. and P. N. Pusey, "Shear-induced order in suspensions of hard spheres," Physical Review Letters **61**, 1033 (1988), Copyright (C) 2009 The American Physical Society Please report any problems to prola@aps.org PRL.

[7] Adrian, R. J., "Double exposure, multiple-field particle image velocimetry for turbulent probability density," Optics and Lasers in Engineering **9**, 211–228 (1988), 0143-8166 doi: DOI: 10.1016/S0143-8166(98)90004-5.

[8] Adrian, R. J., "Twenty years of particle image velocimetry," Experiments in Fluids **39**, 159 (2005), doi:10.1007/s00348-005-0991-7.

[9] Alahyari, A. and E. K. Longmire, "Particle image velocimetry in a variable-density flow - application to a dynamically evolving microburst," Experiments in Fluids **17**, 434–440 (1994), Times Cited: 17 0723-4864.

[10] Aminabhavi, T. M., "Use of mixing rules in the analysis of data for binary liquid mixtures," Journal of Chemical and Engineering Data **29**, 54–55 (1984).

[11] Ancey, C., "Role of lubricated contacts in concentrated polydisperse suspensions," Journal of Rheology **45**, 1421–1439 (2001).

[12] Ancey, C., "Notebook : Introduction to fluid rheologie," Tech. rep., EPFL (2005).

[13] Ancey, C., "Solving the couette inverse problem by using a wavelet-vaguelette decomposition," Journal of Rheology **49**, 441–460 (2005).

[14] Ancey, C. and P. Coussot, *Rhéophysique des Pâtes et des Suspensions*, EDP Sciences, Paris (1999).

[15] Ancey, C. and P. Coussot, "Transition from frictional to viscous regime for granular suspensions," Comptes Rendus de l'Académie des Sciences de Paris **327**, 515–522 (1999).

[16] Ancey, C., P. Coussot and P. Evesque, "A theoretical framework for very concentrated granular suspensions in a steady simple shear flow." Journal of Rheology **43**, 1673–1699 (1999).

[17] Ancey, C. and H. Jorrot, "Yield stress for particle suspensions within a clay dispersion," Journal of Rheology **45**, 297–319 (2001).

[18] Arago, D. and J. BiotMém. acad. France **7** (1806).

[19] Arrhenius, S.Zeitschrift Für Physikalische Chemie **1**, 286 (1877).

[20] Atsavapranee, P. and M. Gharib, "Structures in stratified plane mixing layers and the effects of cross-shear," Journal of Fluid Mechanics **342**, 53–86 (1997), null.

[21] Augier, F., J. Morchain, P. Guiraud and O. Masbernat, "Volume fraction gradient-induced flow patterns in a two-liquid phase mixing layer," Chemical Engineering Science **58**, 3985–3993 (2003), 0009-2509 doi: DOI: 10.1016/S0009-2509(03)00267-7.

[22] Averbakh, A., A. Shauly, A. Nir and R. Semiat, "Slow viscous flows of highly concentrated suspensions–part i: Laser-doppler velocimetry in rectangular ducts," International Journal of Multiphase Flow **23**, 409–424 (1997), 0301-9322 doi: DOI: 10.1016/S0301-9322(96)00078-X.

[23] Bagnold, R. a., "Experiments on a gravity-free dispersion of large solid spheres in a newtonian fluid under shear," Proceedings of the Royal Society of London Series a-Mathematical and Physical Sciences **225**, 49–63 (1954).

[24] Barnes, H., "A review of the slip (wall depletion) of polymer solutions, emulsions and particle suspensions in viscosimeters: its cause, character, and cure," Journal of Non-Newtonian Fluid Mechanics **56**, 221–251 (1995).

[25] Barnes, H. and Q. Nguyen, "Rotating vane rheometry - a review," Journal of Non-Newtonian Fluid Mechanics **98**, 1–14 (2001).

[26] Barnes, H. A., "Shear-thickening ("dilatancy") in suspensions of nonaggregating solid particles dispersed in newtonian liquids," Journal of Rheology **33**, 329 (1989).

[27] Barnes, H. A. and J. O. Carnali, "The vane-in-cup as a novel rheometer geometry for shear thinning and thixotropic materials," Journal of Rheology **34**, 841–866 (1990).

[28] Batchelo.Gk, "Stress system in a suspension of force-free particles," Journal of Fluid Mechanics **41**, 545 (1970), Times Cited: 597 0022-1120.

[29] Batchelo.Gk and J. T. Green, "Determination of bulk stress in a suspension of spherical-particles to order c-2," Journal of Fluid Mechanics **56**, 401–427 (1972), Times Cited: 399 0022-1120.

[30] Batchelo.Gk and J. T. Green, "Hydrodynamic interaction of 2 small freely-moving spheres in a linear flow field," Journal of Fluid Mechanics **56**, 375 (1972), Times Cited: 326 0022-1120.

[31] Batchelor, G. K., "Transport properties of two-phase materials with random structure," Annual Review of Fluid Mechanics **6**, 227–255 (1974).

[32] Batchelor, G. K., "Effect of brownian-motion on bulk stress in a suspension of spherical-particles," Journal of Fluid Mechanics **83**, 97–117 (1977), Times Cited: 416 0022-1120.

[33] Bedeaux, D. and P. Mazur, "A generalization of faxÈn's theorem to nonsteady motion of a sphere through a compressible fluid in arbitrary flow," Physica **78**, 505–515 (1974).

[34] Bonn, D., S. Rodts, M. Groenink, S. Rafai, N. Shahidzadeh-Bonn and P. Coussot, "Some applications of magnetic resonance imaging in fluid mechanics: Complex flows and complex fluids," Annual Review of Fluid Mechanics **40**, 209–233 (2008), 0066-4189.

[35] Borgia, A. and F. J. Spera, "Error analysis for reducing noisy wide-gap concentric cylinder rheometric data for nonlinear fluids: Theory and applications," Journal of Rheology **34**, 117–136 (1990).

[36] Bovendeerd, P. H. M., A. A. V. Steenhoven, F. N. V. D. Vosse and G. Vossers, "Steady entry flow in a curved pipe," Journal of Fluid Mechanics Digital Archive **177**, 233–246 (1987), 10.1017/S0022112087000934.

[37] Brady, J. F. and J. F. Morris, "Microstructure of strongly sheared suspensions and its impact on rheology and diffusion," Journal of Fluid Mechanics **348**, 103–139 (1997), null.

[38] Braun, M. J., V. A. Canacci and R. C. Hendricks, "Flow visualization and quantitative velocity and pressure measurements in simulated single and double brush seals," Tribology Transactions **34**, 70 – 80 (1991).

[39] Breedveld, V., D. van den Ende, M. Bosscher, R. J. J. Jongschaap and J. Mellema, "Measuring shear-induced self-diffusion in a counterrotating geometry," Physical Review E **63**, 021403 (2001), Copyright (C) 2009 The American Physical Society Please report any problems to prola@aps.org PRE.

[40] Breedveld, V., D. van den Ende, M. Bosscher, R. J. J. Jongschaap and J. Mellema, "Measurement of the full shear-induced self-diffusion tensor of noncolloidal suspensions," The Journal of Chemical Physics **116**, 10529–10535 (2002).

[41] Breedveld, V., D. van den Ende, R. Jongschaap and J. Mellema, "Shear-induced diffusion and rheology of noncolloidal suspensions: Time scales and particle displacements," The Journal of Chemical Physics **114**, 5923–5936 (2001).

[42] Breedveld, V., D. Van Den Ende, A. Tripathi and A. Acrivos, "The measurement of the shear-induced particle and fluid tracer diffusivities in concentrated suspensions by a novel method," Journal of Fluid Mechanics **375**, 297–318 (1998), null.

[43] Brinkman, H. C., "The viscosity of concentrated suspensions and solutions," The Journal of Chemical Physics **20**, 571–571 (1952).

[44] Brown, J. M., B. M. Kadlubowski, L. J. Forney and J. T. Sommerfeld, "Density gradient columns: Dynamic modeling for linear profiles," Review of Scientific Instruments **67**, 3973–3980 (1996).

[45] Budwig, R., "Refractive index matching methods for liquid flow investigations," Experiments in Fluids **17**, 350–355 (1994).

[46] Budwig, R., D. Elger, H. Hooper and J. Slippy, "Steady flow in abdominal aortic-aneurysm models," Journal of Biomechanical Engineering-Transactions of the Asme **115**, 418–423 (1993), Times Cited: 30 A 0148-0731.

[47] Budwig, R., J. Martinez and T. Carlson, "Hydrodynamic and mass transfer characteristics of acoustically levitated and oscillated droplets," Bull Amer Phys Soc **33** (1993).

[48] Burdett, I. D., D. R. Webb and G. A. Davies, "A new technique for studying dispersion flow, holdup and axial mixing in packed extraction columns," Chemical Engineering Science **36**, 1915–1919 (1981), 0009-2509 doi: DOI: 10.1016/0009-2509(81)80030-9.

[49] Buyevich, Y. A., "Particle distribution in suspension shear flow," Chemical Engineering Science **51**, 635–647 (1996).

[50] Callaghan, P. T., "Rheo-nmr: nuclear magnetic resonance and the rheology of complex fluids," Reports on Progress in Physics **62**, 599–670 (1999), 0034-4885.

[51] Cariou, J. M., J. Dugas, L. Martin and P. Michel, "Refractive-index variations with temperature of pmma and polycarbonate," Appl. Opt. **25**, 334–336 (1986).

[52] Castillo, C. and M. C. Williams, "Rheology of very concentrated coal suspensions," Chemical Engineering Communications **3**, 529 – 545 (1979).

[53] Cenedese, A. and P. Viotti, "Lagrangian analysis of nonreactive pollutant dispersion in porous media by means of the particle image velocimetry technique," Water Resour. Res. **32** (1996), 10.1029/96WR00605.

[54] Chang, C. and R. Powell, "Effect of particle size distributions on the rheology of concentrated bimodal suspensions," Journal of Rheology **38**, 85–98 (1994).

[55] Chang, C. and R. L. Powell, "Hydrodynamic transport properties of concentrated suspensions," AIChE Journal **48**, 2475–2480 (2002), 1547-5905 10.1002/aic.690481106.

[56] Chateau, X., G. Ovarlez and K. L. Trung, "Homogenization approach to the behavior of suspensions of noncolloidal particles in yield stress fluids," Journal of Rheology **52**, 489–506 (2008).

[57] Chaudhuri, P., Y. Gao, L. Berthier, M. Kilfoil and W. Kob, "A random walk description of the heterogeneous glassy dynamics of attracting colloids," Journal of Physics: Condensed Matter **20**, 244126 (2008), 0953-8984.

[58] Chen, B., F. Mikami and N. Nishikawa, "Experimental studies on transient features of natural convection in particles suspensions," International Journal of Heat and Mass Transfer **48**, 2933–2942 (2005), Times Cited: 1 0017-9310.

[59] Chen, R. C., *Experimental and Numerical Studies of Solid-Liquid Multiphase Flow in Pipes*, Ph.D. thesis, Case Western Reserve Univ (1991).

[60] Chen, R. C. and L. S. Fan, "Particle image velocimetry for characterizing the flow structure in three-dimensional gas-liquid-solid fluidized beds," Chemical Engineering Science **47**, 3615–3622 (1992), 0009-2509 doi: DOI: 10.1016/0009-2509(92)85077-O.

[61] Chen, R. C., J.-W. Tzeng, J. Reese and L. S. Fan, "Bed flow structure of a three-dimensional three-phase fluidized bed," in *AIChE Annual Meeting*, Miami Beach, FL (1992).

[62] Chong, J., E. Christiansen and A. Baer, "Rheology of concentrated suspensions," Journal of Applied Polymer Science **15**, 2007–2021 (1971).

[63] Chow, A. W., S. W. Sinton, J. H. Iwamiya and T. S. Stephens, "Shear-induced particle migration in couette and parallel-plate viscometers: Nmr imaging and stress measurements," Physics of Fluids **6**, 2561–2576 (1994).

[64] Christiansen, C., "Untersuchungen über die optischen eigenschaften von fein verteilten körpern," Ann. Phys. Chem. **23**, 298–306 (1884).

[65] Christiansen, C., "Untersuchungen über die optischen eigenschaften von fein verteilten körpern," Ann. Phys. Chem. **24**, 439–446 (1885).

[66] Code, R. K. and J. D. Raal, "Rates of shear in coaxial cylinder viscometers," Rheologica Acta **12**, 578 (1973).

[67] Coimbra, C. F. M. and R. H. Rangel, "General solution of the particle momentum equation in unsteady stokes flows," Journal of Fluid Mechanics **370**, 53–72 (1998).

[68] Coleman, B. D., H. Markovitz and W. Noll, "Viscosimetric flows of non-newtonian fluids," Springer tracts in natural philosophy **5** (1966).

[69] Conaghan, B. and S. Rosen, "The optical properties of two -phase polymer systems : Single scattering in monodispese, non-absorbing systems," Polymer Engineering and Science **12**, 134–139 (1972).

[70] Coombs, S. H., "A density-gradient column for determining the specific gravity of fish eggs, with particular reference to eggs of the mackerel scomber scombrus," Marine Biology **63**, 101–106 (1981).

[71] Coussot, P., *Rheometry of Pastes, Suspensions and Granular Materials*, John Wiley and Sons, New York (2005).

[72] Coussot, P. and C. Ancey, "Rheophysical classification of concentrated suspensions and granular pastes," Physical Review E **59**, 4445–4457 (1999).

[73] Coussot, P., J. Raynaud and C. Ancey, "Combined mri-rheometry determination of the behavior of mud suspensions," in *Debris flow Mechanics and Mitigation Conference*, eds. C. Chen and D. Rickenmann, pp. 291–301, Davos (2003), Mills Press.

[74] Coussot, P., J. S. Raynaud, F. Bertrand, P. Moucheront, J. P. Guilbaud, H. T. Huynh, S. Jarny and D. Lesueur, "Coexistence of liquid and solid phases in flowing soft-glassy materials," Physical Review Letters **88**, 218301 (2002).

[75] Cox, R. G., "The motion of suspended particles almost in contact," International Journal of Multiphase Flow **1**, 343–371 (1974).

[76] Crowe, C., M. Sommerfeld and Y. Tsuji, *Multiphase Flows with Droplets and Particles*, CRC, Boca Raton (1998).

[77] Cui, M. and R. Adrian, "Refractive index matching and marking methods for highly concentrated solid-liquid flows," Experiment in Fluids **22**, 261–264 (1997).

[78] Da Cruz, F., F. Chevoir, D. Bonn and P. Coussot, "Viscosity bifurcation in granular materials, foams, and emulsions," Physical Review E **66**, 051305 (2002).

[79] Dale, D. and F. GladstonePhil. Trans. **148**, 887 (1858).

[80] Dale, D. and F. GladstonePhil. Trans. **153**, 317 (1864).

[81] Dames, B., B. R. Morrison and N. Willenbacher, "An empirical model predicting the viscosity of highly concentrated, bimodal dispersions with colloidal interactions," Rheologica Acta **40**, 434–440 (2001), 10.1007/s003970100171.

[82] Dandy, D. S. and H. A. Dwyer, "A sphere in shear-flow at finite reynolds-number - effect of shear on particle lift, drag, and heat-transfer," Journal of Fluid Mechanics **216**, 381–410 (1990).

[83] Daviero, G. J., P. J. W. Roberts and K. Maile, "Refractive index matching in large-scale stratified experiments," Experiments in Fluids **31**, 119–126 (2001).

[84] De Hoog, F. R. and R. S. Anderssen, "Approximate solutions for the couette viscometry equation," Bulletin of the Australian Mathematical Society **72**, 461 (2005), 0004-9727.

[85] De Hoog, F. R. and R. S. Anderssen, "Regularization of first kind integral equations with application to couette viscosimetry," Journal of Integral equations and applications **18**, 249 (2006).

[86] De Hoog, F. R. and R. S. Anderssen, "Simple and accurate formulas for flow-curve recovery from couette rheometer data," Applied Rheology **16**, 321–328 (2006).

[87] Decré, M. and J. M. Buchlin, "An extra-thin light sheet technique used to investigate meniscus shapes by laser induced fluorescence," Experiments in Fluids **16**, 339 (1994).

[88] Dibble, C. J., M. Kogan and M. J. Solomon, "Structure and dynamics of colloidal depletion gels: Coincidence of transitions and heterogeneity," Physical Review E (Statistical, Nonlinear, and Soft Matter Physics) **74**, 041403–11 (2006).

[89] Diemunsch, G. and J. P. Prenel, "A compact light sheet generator for flow visualizations," Optics and Laser Technology **19**, 141 (1987).

[90] Donoho, D. L., "Nonlinear solution of linear inverse problems by wavelet-vaguelette decomposition," Applied and Computational Harmonic Analysis **2**, 101–126 (1995).

[91] Durst, F., K. T. and K. R., "Turbulence quantities and reynolds stress in pipe flow of polymer solutions measured by two-channel laser-doppler anemometry," in *Proc., 6th Symp. on Turbulence*, Rolla (1979).

[92] Dybbs, A. and R. V. Edwards, "An index-matched flow system for measurements of flow in complex geometries," in *Proc. 2nd Int. Symp. on Application of LDA to Fluid Mechanics*, pp. 171–184, Lisbon (1984).

[93] Eilers, H., "Die viskosität von emulsionen hochviskoser stoffe als funktion der konzentration," Colloid and Polymer Science **97**, 313–321 (1941).

[94] Eilers, H., "Die viskositäts-konzentrationsabhängigkeit kolloider systeme in organischen lösungsmitteln," Colloid and Polymer Science **102**, 154–169 (1943).

[95] Einstein, A., "Eine neue bestimmung der molekiildimensionen," Ann. Phys. **19**, 289 (1906).

[96] Einstein, A., "Berichigung zu meiner arbeit: "eine neue bestimmung der moleküldimensionen"," Ann. Phys. **34**, 591–592 (1911).

[97] Eirich, F., M. Bunzl and H. Margaretha, "Untersuchungen über die viskosität von suspensionen und lösungen. 4. Über die viskosität von kugelsuspensionen," Colloid and Polymer Science **74**, 276–285 (1936).

[98] Eirich, F. and O. Goldschmid, "Untersuchungen über die viskosität von suspensionen und lösungen 8. Über trägheitseffekte suspendierter kugeln," Colloid and Polymer Science **81**, 7–18 (1937).

[99] Eirich, F., H. Margaretha and M. Bunzl, "Untersuchungen über die viskosität von suspensionen und lösungen 6. Über die viskosität von stäbchensuspensionen," Colloid and Polymer Science **75**, 20–37 (1936).

[100] Elphick, R. V., W. W. Martin and I. G. Currie, "Application of lda to high reynolds number cross flow," in *Proc. 2nd Int. Symp. on Application of LDA to Fluid Mechanics*, Lisbon (1984).

[101] Estellé, P., C. Lanos and A. Perrot, "Processing the couette viscometry data using a bingham approximation in shear rate calculation," Journal of Non-Newtonian Fluid Mechanics **154**, 31–38 (2008).

[102] Eveson, G.Journal of the Oil and Colour Chemists' Association **40**, 150 (1958).

[103] Farris, R., "Prediction of the viscosity of multimodal suspensions from unimodal viscosity data," Transactions of the Society of Rheology **12**, 281–301 (1968).

[104] Frankel, N. and A. Acrivos, "On the viscosity of a concentrated suspension of solid spheres," Chemical Engineering Science **22**, 847–853 (1967).

[105] Fukushima, E., "Nuclear magnetic resonance as a tool to study flow," Annual Review of Fluid Mechanics **31**, 95–123 (1999).

[106] Gadala-Maria, F. and A. Acrivos, "Shear-induced structure in a concentrated suspension of solid spheres," Journal of Rheology **24**, 799–814 (1980).

[107] Gao, Y. and M. L. Kilfoil, "Direct imaging of dynamical heterogeneities near the colloid-gel transition," Physical Review Letters **99**, 078301–4 (2007).

[108] Gijsen, F. J. H., D. E. M. Palmen, M. H. E. van der Beek, F. N. van de Vosse, M. E. H. van Dongen and J. D. Janssen, "Analysis of the axial flow field in stenosed carotid artery bifurcation models–lda experiments," Journal of Biomechanics **29**, 1483–1489 (1996), 0021-9290 doi: DOI: 10.1016/0021-9290(96)84544-1.

[109] Graham, A., S. Altobelli, E. Fukushima, L. Mondy and T. Stephens, "Note : Nmr imaging of shear induced diffusion and structure in concentrated suspensions udergoing couette flow," Journal of Rheology **35**, 191–201 (1991).

[110] Graham, A. and R. Bird, "Particle clusters in concentrated suspensions. 1. experimental observations of particle clusters," Industrial and Engineering Chemistry : Fundamentals **23**, 406–410 (1984).

[111] Grant, I., "Particle image velocimetry: a review," Proceedings of the Institution of Mechanical Engineers, Part C: Journal of Mechanical Engineering Science **211**, 55–76 (1997), 10.1243/0954406971521665.

[112] Guth, E., "Untersuchungen über die viskosität von suspensionen und lösungen. 1. Über die viskosität von suspensionen," Colloid and Polymer Science **74**, 147–172 (1936).

[113] Guth, E., "Untersuchungen über die viskosität von suspensionen und lösungen 5. Über den einfluß der brown'schen bewegung auf die viskosität von ellipsoidsuspensionen," Colloid and Polymer Science **75**, 15–20 (1936).

[114] Guth, E. and R. Simha, "Untersuchungen über die viskosität von suspensionen und lösungen. 3. Über die viskosität von kugelsuspensionen," Colloid and Polymer Science **74**, 266–275 (1936).

[115] Haam, S. J., *Multiphase research on solid-liquid dispersion*, Ph.D. thesis, The Ohio State University (1996).

[116] Haam, S. J., R. S. Brodkey, I. Fort, L. Klaboch, M. Placnik and V. Vanecek, "Laser doppler anemometry measurements in an index of refraction matched column in the presence of dispersed beads," (1998).

[117] Haam, S. J., R. S. Brodkey, I. Fort, L. Klaboch, M. Placnik and V. Vanecek, "Laser doppler anemometry measurements in an index of refraction matched column in the presence of dispersed beads: Part i," International Journal of Multiphase Flow **26**, 1401–1418 (2000), 0301-9322 doi: DOI: 10.1016/S0301-9322(99)00094-4.

[118] Ham, J. M. and G. M. Homsy, "Hindered settling and hydrodynamic dispersion in quiescent sedimenting suspensions," International Journal of Multiphase Flow **14**, 533–546 (1988), 0301-9322 doi: DOI: 10.1016/0301-9322(88)90056-0.

[119] Hannoun, I. A., H. I. S. Fernando and E. l. List, "Matching the refractive index in density stratified flows." Tech. rep., California Institute of Technology (1985).

[120] Hannoun, I. A., H. J. S. Fernando and E. J. List, "Turbulence structure near a sharp density interface," Journal of Fluid Mechanics Digital Archive **189**, 189–209 (1988), 10.1017/S0022112088000965.

[121] Happel, J. and H. Brenner, "Low reynolds's number hydrodynamics," p. 389, Noordhoff International, The Netherlands, 2nd editiion edn. (1973).

[122] Hassan, Y. A. and E. E. Dominguez-Ontiveros, "Flow visualization in a pebble bed reactor experiment using piv and refractive index matching techniques," Nuclear Engineering and Design **238**, 3080–3085 (2008), Times Cited: 0 0029-5493.

[123] Heckenbach, M. and E. Muschelknautz, "Zum einfluß der exzentrizität bei viskositätsmessungen mit rotationsviskosimetern," Rheologica Acta **17**, 69–76 (1978).

[124] Heirman, G., L. Vandewalle, D. Van Gemert and . Wallevik, "Integration approach of the couette inverse problem of powder type self-compacting concrete in a wide-gap concentric cylinder rheometer," Journal of Non-Newtonian Fluid Mechanics **150**, 93–103 (2008).

[125] Heller, W., "The determination of refractive indices of colloidal particles by means of a new mixture rule or from measurements of light scattering," Physical Review **68**, 5–10 (1945).

[126] Heller, W., "Remarks on refractive index mixture rules," The Journal of Physical Chemistry **69**, 1123–1129 (1965).

[127] Hendriks, F. and A. Aviram, "Use of zinc iodide solutions in flow research," Review of Scientific Instruments **53** (1982).

[128] Hersey, M. D., "Future problems of theoretical rheology," Journal of Rheology **3**, 196 (1932).

[129] Hoffman, R. L., "Discontinuous and dilatant viscosity behavior in concentrated suspensions. i. observation of a flow instability," Journal of Rheology **16**, 155–173 (1972).

[130] Hoffman, R. L., "Discontinuous and dilatant viscosity behavior in concentrated suspensions. ii. theory and experimental tests," Journal of Colloid and Interface Science **46**, 491–506 (1974).

[131] Horvay, M. and W. Leuckel, "Lda measurement of liquid swirl flow in converging swirl chamber with tangential inlets," in *Proc. 2nd Int. Symp. on Application of LDA to Fluid Mechanics*, Lisbon (1984).

[132] Huang, N., G. Ovarlez, F. Bertrand, S. Rodts, P. Coussot and D. Bonn, "Flow of wet granular materials," Physical Review Letters **94**, 028301 (2005).

[133] Hunt, M. L., R. Zenit, C. S. Campbell and C. E. Brennen, "Revisiting the 1954 suspension experiments of r. a. bagnold," Journal of Fluid Mechanics **452**, 1–24 (2002).

[134] Hurlburt, C., "The jewler's refractometer as a mineralogical tool," American Mineralogist **69**, 391–398 (1984).

[135] Inglis, D. R., "Viscous force between almost-coaxial cylinders," Physical Review **56**, 1041 (1939).

[136] Jacobs, D. A., C. W. Jacobs and C. D. Andereck, "Biological scattering particles for laser doppler velocimetry," Physics of Fluids **31**, 3457–3461 (1988).

[137] Jacobsen, R. T., "The determination of the flow curve of a plastic medium in a wide gap rotational viscometer," Journal of Colloid and Interface Science **48**, 437–441 (1974).

[138] Jana, S. C., B. Kapoor and A. Acrivos, "Apparent wall slip velocity coefficients in concentrated suspensions of noncolloidal particles," Journal of Rheology **39**, 1123–1132 (1995).

[139] Jarny, S., N. Roussel, S. Rodts, F. Bertrand, R. Le Roy and P. Coussot, "Rheological behavior of cement pastes from mri velocimetry," Cement and Concrete Research **35**, 1873–1881 (2005).

[140] Jenkins, J. T. and D. McTigue, "Transport processes in concentrated suspensions: the role of particle fluctuations," in *Two phase flows and waves*, pp. 70–79, Springer-Verlag (1990).

[141] Jeon, D., F. Pereira and M. Gharib, "Application of defocusing dpiv to bubbly flow measurement," Particle and Particle Systems Characterization **20**, 193–198 (2003).

[142] Johnston, W., A. Dybbs and R. Edwards, "Measurement of fluid velocity inside porous media with a laser anemometer," Physics of Fluids **18**, 913–914 (1975).

[143] Jomha, A. I., A. Merrington, L. V. Woodcock, H. A. Barnes and A. Lips, "Recent developments in dense suspension rheology," Powder Technology **65**, 343–370 (1991).

[144] Kadambi, J. R., R. C. Chen, S. Bhunia, A. Z. Dybbs, R. V. Edwards and A. Rutstein, "Measurement of solid-liquid multiphase flow using refractive-index matching technique," Laser Anemometry / - Advances and Applications pp. 477–487 (1990).

[145] Kannemans, H., "Principles of lda measurements in a fully transparent pump," in *Fluid Mechanics Silver Jubilee Conf.*, Glasgow (1979).

[146] Kapoor, B. and A. Acrivos, "Sedimentation and sediment flow in settling tanks with inclined walls," Journal of Fluid Mechanics Digital Archive **290**, 39–66 (1995), 10.1017/S0022112095002412.

[147] Karnis, A., H. L. Goldsmith and S. G. Mason, "The kinetics of flowing dispersions: I. concentrated suspensions of rigid particles," Journal of Colloid and Interface Science **22**, 531–553 (1966).

[148] Kaufman, L. J. and D. A. Weitz, "Direct imaging of repulsive and attractive colloidal glasses," The Journal of Chemical Physics **125**, 074716–11 (2006).

[149] Keane, R. D. and R. J. Adrian, "Optimization of particle image velocimeters. i. double pulsed systems," Measurement Science and Technology p. 1202 (1990).

[150] Kegel, W. K. and A. van Blaaderen, "Direct observation of dynamical heterogeneities in colloidal hard-sphere suspensions," Science **287**, 290–293 (2000).

[151] Kilja?ski, T., "A method for correction of the wall-slip effect in a couette rheometer," Rheologica Acta **28**, 61–64 (1989), 10.1007/BF01354770.

[152] Kitano, T., T. Kataoka and T. Shirota, "An empirical equation of the relative viscosity of polymer melts filled with various inorganic fillers," Rheologica Acta **20**, 207–209 (1981).

[153] Koga, D. J., S. D. Abrahamson and J. K. Eaton, "Development of a portable laser sheet," Experiments in Fluids **5**, 215 (1987).

[154] Koh, C., *Experimental and theoretical studies on two-phase ⁻ows*, Ph.D. thesis, California Institute of Technology (1991).

[155] Koh, C., P. Hookham and L. Leal, "An experimental investigation of concentrated suspension flows in a rectangular channel," Journal of Fluid Mechanics **266**, 1–32 (1994).

[156] Kohnen, C. and M. Bohnet, "Measurement and simulation of fluid flow in agitated solid/liquid suspensions," Chemical Engineering and Technology **24**, 639–643 (2001), Times Cited: 3 0930-7516.

[157] Krasny-Ergen, W., "Untersuchungen über die viskosität von suspensionen und lösungen. 2. zur theorie der elektroviskosität," Colloid and Polymer Science **74**, 172–178 (1936).

[158] Krieger, I. and H. Elrod, "Direct determination of the flow curves of non-newtonian fluids. ii shearing rate in the concentric cylinder viscometer," Journal of Applied Physics **24**, 134–136 (1953).

[159] Krieger, I. and S. Maron, "Direct determination of the flow curves of non-newtonian fluids," Journal of Applied Physics **23**, 147–149 (1952).

[160] Krieger, I. and S. Maron, "Direct determination of the flow curves of non-newtonian fluids. iii. standardized treatment of viscosimetric data," Journal of Applied Physics **25**, 72–75 (1954).

[161] Krieger, I. M., "A dimensional approach to colloid rheology," Transactions of the Society of Rheology **7**, 101–109 (1963), 0038-0032.

[162] Krieger, I. M., "Computation of shear rate in the couette viscometer," in *Proceedings of the fifth international congress on rheology*, ed. S. Onogi, vol. 1, pp. 511–516, Tokyo (1968), Tokyo : University of Tokyo Press, 1970.

[163] Krieger, I. M., "Shear rate in the couette viscometer," Journal of Rheology **12**, 5 (1968).

[164] Krieger, I. M., "Rheology of monodisperse latices," Advances in Colloid and Interface Science **3**, 111–136 (1972).

[165] Krieger, I. M. and T. J. Dougherty, "A mechanism for non-newtonian flow in suspensions of rigid spheres," Transactions of the Society of Rheology **3**, 137–152 (1959), Times Cited: 594 0038-0032.

[166] Krishnan, G. P., S. Beimfohr and D. T. Leighton, "Shear-induced radial segregation in bidisperse suspensions," Journal of Fluid Mechanics Digital Archive **321**, 371–393 (1996).

[167] Kynch, G. J., "The effective viscosity of suspensions of spherical particles," Proceedings of the Royal Society of London. Series A, Mathematical and Physical Sciences **237**, 90–116 (1956).

[168] Landreth, C. C. and R. J. Adrian, "Measurement and refinement of velocity data using high image density analysis in particle image velocimetry," in *Applicaions of Laser Anemometry to Fluid Mechanics*, ed. R. Adrian, p. 484, Springer, Berlin (1989).

[169] Leighton, D. and A. Acrivos, "Measurement of shear-induced self-diffusion in concentrated suspensions of spheres," Journal of Fluid Mechanics **177**, 109–131 (1987), Times Cited: 199 0022-1120.

[170] Leighton, D. and A. Acrivos, "The shear-induced migration of particles in a concentrated suspensions," Journal of Fluid Mechanics **181**, 415–439 (1987).

[171] Leighton, D. and I. Rampall, "Measurement of the shear-induced microstructure of concentrated suspensions of non-colloidal spheres," in *Particle Two-Phase Flow*, ed. M. Roco, pp. 190–208, Butterworth-Heinemann, Boston (1993).

[172] Lenoble, M., P. Snabre and B. Pouligny, "The flow of very concentrated slurry in a parallel-plate device: influence of gravity," Physics of Fluids **17**, 073303 (2005).

[173] Lenoble, M., P. Snabre and B. Pouligny, "Shearing a granular pate in a couette device : flow and size segraegation," Powders and Grains pp. 621–624 (2005).

[174] Leong, Y. K. and Y. L. Yeow, "Obtaining the shear stress shear rate relationship and yield stress of liquid foods from couette viscometry data," Rheologica Acta **42**, 365–371 (2003), 10.1007/s00397-002-0283-6.

[175] Lhuillier, D., "On the equation of motion of a rigid sphere in a non uniform and accelerated inviscid fluid. incidence on two-phase flow equations," Mechanics Research Communications **9**, 295–299 (1982).

[176] Lhuillier, D., "Contribution des particules à la contrainte globale d'une suspension," Comptes Rendus de l'Académie des Sciences série II b **323**, 3–8 (1996).

[177] Liu, A. J. and S. R. Nagel, "Nonlinear dynamics: Jamming is not just cool any more," Nature **396**, 21–22 (1998), 0028-0836 10.1038/23819 10.1038/23819.

[178] Liu, C. H., J. M. Nouri, J. H. Whitelaw and D. G. N. Tse, "Particle velocities in a swirling, confined flow," Combustion Science and Technology **68**, 131–145 (1989).

[179] Liu, C. H., C. Vafidis, J. H. Whitelaw and R. Margary, "Flow in the coolant passages of an internal combustion engine cylinder head," Experiments in Fluids **10**, 50–54 (1990), 10.1007/BF00187872.

[180] Lorentz, H. A., *Theory of electrons*, Leipzig (1096).

[181] Lyon, M. and L. Leal, "An experimental study of the motion of concentrated suspensions in two-dimensional channel flow. part 1. monodisperse systems," Journal of Fluid Mechanics **363**, 25–56 (1998).

[182] Lyon, M. and L. Leal, "An experimental study of the motion of concentrated suspensions in two-dimensional channel flow. part 2. bidisperse systems," Journal of Fluid Mechanics **363**, 57–77 (1998).

[183] Macosko, C. W., *Rheology principles, measurements, and applications*, Advances in interfacial engineering series, VCH (1994), XVIII, 550 S.

[184] Macsporran, W., "Direct numerical evaluation of shear rates in concentric cylinder viscometry using least-squares cubic splines," Journal of Rheology **33**, 745–755 (1989).

[185] MacSporran, W. C., "Direct numerical evaluation of shear rates in concentric cylinder viscometry," Journal of Rheology **30**, 125–132 (1986).

[186] Mahaut, F., X. Chateau, P. Coussot and G. Ovarlez, "Yield stress and elastic modulus of suspensions of noncolloidal particles in yield stress fluids," Journal of Rheology **52**, 287–313 (2008).

[187] Maron, S. H. and P. E. Pierce, "Application of ree-eyring generalized flow theory to suspensions of spherical particles," Journal of Colloid Science **11**, 80–95 (1956).

[188] Marrucci, G. and M. M. Denn, "On the viscosity of a concentrated suspension of solid spheres," Rheologica Acta **24**, 317–320 (1985).

[189] Maxey, M. R. and J. J. Riley, "Equation of motion for a small rigid sphere in a nonuniform flow," Physics of Fluids **26**, 883–889 (1983), Times Cited: 780 1070-6631.

[190] Mazur, P. and D. Bedeaux, "A generalization of faxen's theorem to nonsteady motion of a sphere through an incompressible fluid in arbitrary flow," Physica **76**, 235–246 (1974).

[191] McDougall, T. J., "On the elimination of refractive-index variations in turbulent density-stratified liquid flows," Journal of Fluid Mechanics Digital Archive **93**, 83–96 (1979), 10.1017/S0022112079001798.

[192] McLaughlin, J. B., "Inertial migration of a small sphere in linear shear flows," Journal of Fluid Mechanics **224**, 261–274 (1991), Times Cited: 138 0022-1120.

[193] McTigue, D. and J. T. Jenkins, "Channel flow of a concentrated suspension," in *Advances in micromechanics of granular materials*, ed. S. H.H., pp. 381–390, Elsevier Science Publishers B.V. (1992).

[194] Meerlender, G., "Beiträge zur meßtechnik der rotationsviskosimeter," Rheologica Acta **6**, 83–92 (1967).

[195] Mehta, M., J. R. Kadambi, S. Sastry, J. M. Sankovic, M. P. Wernet, G. Addie and R. Visintainer, "Particle velocities in the rotating impeller of a slurry pump," Fedsm 2007: Proceedings of the 5th Joint Amse/Jsme Fluids Engineering Summer Conference Vol 1, Pts a and B pp. 369–378 (2007).

[196] Melling, A., "Tracer particles and seeding for particle image velocimetry," Measurement Science and Technology **8**, 1406 (1997), 0957-0233.

[197] Metzner, A. B., "Rheology of suspensions in polymeric liquids," Journal of Rheology **29**, 739–775 (1985).

[198] Mewis, J. and N. J. Wagner, "Current trends in suspension rheology," Journal of Non-Newtonian Fluid Mechanics **157**, 147–150 (2009), 0377-0257 doi: DOI: 10.1016/j.jnnfm.2008.11.004.

[199] Mikami, F., B. Chen and N. Nishikawa, "Visualization of the flow features of natural convection in particle suspensions," Theoretical and Applied Mechanics pp. 341–348 (1997).

[200] Mikami, F., B. Chen and N. Nishikawa, "Visualization and ptv study of natural convection in particle suspensions (simultaneous measurements of velocity, temperature and interface between particle-free fluid and suspension," Jsme International Journal Series B-Fluids and Thermal Engineering **44**, 30–37 (2001).

[201] Milliken, W. J., M. Gottlieb, A. L. Graham, L. A. Mondy and R. L. Powell, "The viscosity-volume fraction relation for suspensions of rod-like particles by falling-ball rheometry," Journal of Fluid Mechanics Digital Archive **202**, 217–232 (1989).

[202] Mills, P. and P. Snabre, "Rheology and structure of concentrated suspensions of hard-spheres - shear-induced particle migration," Journal De Physique Ii **5**, 1597–1608 (1995).

[203] Mondy, L. A., A. L. Graham, A. Majumdar and L. E. Bryant, "Techniques of measuring particle motions in concentrated suspensions," International Journal of Multiphase Flow **12**, 497–502 (1986), Times Cited: 10 0301-9322.

[204] Mooney, M., "Explicit formulas for slip and fluidity," Journal of Rheology **2**, 210–222 (1931).

[205] Mooney, M., "The viscosity of a concentrated suspension of spherical particles," Journal of Colloid Science **6**, 162–170 (1951), Times Cited: 734.

[206] Moore, F. and L. Davies, "The consistency of ceramics slip," Transactions and journal of the British Ceramic Society **55**, 313–338 (1956).

[207] Moroni, M. and J. H. Cushman, "Three-dimensional particle tracking velocimetry studies of the transition from pore dispersion to fickian dispersion for homogeneous porous media," Water Resour. Res. **37** (2001), 10.1029/2000WR900364.

[208] Morris, J. F. and F. Boulay, "Curvilinear flows of noncolloidal suspensions: The role of normal stresses," Journal of Rheology **43**, 1213–1237 (1999).

[209] Morris, J. F. and J. F. Brady, "Self-diffusion in sheared suspensions," Journal of Fluid Mechanics **312**, 223–252 (1996).

[210] Morris, J. F. and J. F. Brady, "Pressure-driven flow of a suspension: Buoyancy effects," International Journal of Multiphase Flow **24**, 105–130 (1998).

[211] Narrow, T. L., M. Yoda and S. I. Abdel-Khalik, "A simple model for the refractive index of sodium iodide aqueous solutions," Experiments in Fluids **28**, 282–283 (2000).

[212] Nguyen, Q. and D. Boger, "Direct yield stress measurement with the vane method," Journal of Rheology **29**, 335–347 (1985).

[213] Nguyen, Q. and D. Boger, "Characterization of yield stress fluids using the concentric viscometry," Rheologica Acta **26**, 508–515 (1987).

[214] Nguyen, Q. D. and D. V. Boger, "Measuring the flow properties of yield stress fluids," Annual Review of Fluid Mechanics **24**, 47–88 (1992).

[215] Nicolai, H. and E. Guazzelli, "Effect of the vessel size on the hydrodynamic diffusion of sedimenting spheres," Physics of Fluids **7**, 3–5 (1995).

[216] Nicolai, H., B. Herzhaft, E. J. Hinch, L. Oger and E. Guazzelli, "Particle velocity fluctuations and hydrodynamic self-diffusion of sedimenting non-brownian spheres," Physics of Fluids **7**, 12–23 (1995).

[217] Nicolai, H., Y. Peysson and E. Guazzelli, "Velocity fluctuations of a heavy sphere falling through a sedimenting suspension," Physics of Fluids **8**, 855–862 (1996).

[218] Ninomiya, N. and K. Yasuda, "Visualization and piv measurement of the flow around and inside of a falling droplet," Journal of Visualization **9**, 257–264 (2006).

[219] Northrup, M. A., T. J. Kulp and S. M. Angel, "Application of fluorescent particle imaging to measuring flow in complex media," Analytica Chimica Acta **255**, 275–282 (1991).

[220] Northrup, M. A., T. J. Kulp and S. M. Angel, "Fluorescent particle image velocimetry - application to flow measurement in refractive index-matched porous-media," Applied Optics **30**, 3034–3040 (1991).

[221] Northrup, M. A., T. J. Kulp, S. M. Angel and G. F. Pinder, "Direct measurement of interstitial velocity-field variations in a porous-medium using fluorescent-particle image velocimetry," Chemical Engineering Science **48**, 13–21 (1993).

[222] Nott, P. R. and J. F. Brady, "Pressure-driven flow of suspensions: simulation and theory," Journal of Fluid Mechanics **275**, 157–199 (1994).

[223] Nouri, J., J. Whitelaw and M. Yianneskis, "An investigation of refractive-index matching of continuous and discontinuous phases," in *Third international symposium on applications of laser anemometry to fluid mechanics* (1986).

[224] Nouri, J., J. Whitelaw and M. Yianneskis, "A refractive-index matching technique for solid/liquid flows," in *Laser anemometry in fluid mechanics, III Selected Papers from the Third Intl. Symp. On Appl. Of Laser-doppler Anemometry to Fluid Mechanics*, p. chapter 4 (1988).

[225] Nouri, J. M., J. H. Whitelaw and M. Yianneskis, "Particle motion and turbulence in dense two-phase flows," International Journal of Multiphase Flow **13**, 729–739 (1987).

[226] Oki, Y., T. Yoshiura, Y. Chisaki and M. Maeda, "Fabrication of a distributed-feedback dye laser with a grating structure in its plastic waveguide," Appl. Opt. **41**, 5030–5035 (2002).

[227] Okumura, M., K. Yuki, H. Hashizume and A. Sagara, "Evaluation of flow structure in packed-bed tube by visualization experiment," Fusion Science and Technology **47**, 1089–1093 (2005).

[228] Oster, G. and M. Yamamoto, "Density gradient techniques," Chemical Reviews **63**, 257 (1963).

[229] Ovarlez, G., F. Bertrand and S. Rodts, "Local determination of the constitutive law of a dense suspension of noncolloidal particles through magnetic resonance imaging," Journal Of Rheology **50**, 259–292 (2006).

[230] Papir, Y. S. and I. M. Krieger, "Rheological studies on dispersions of uniform colloidal spheres .2. dispersions in nonaqueous media," Journal of Colloid and Interface Science **34**, 126 (1970).

[231] Park, J. T., R. J. Mannheimer, T. A. Grimley and T. B. Morrow, "Pipe flow measurements of a transparent non-newtonian slurry," Journal of Fluids Engineering, Transactions of the ASME **111**, 331–336 (1989).

[232] Park, N. A. and T. F. Irvine, "The falling needle viscometer a new technique for viscosity measurements," Heat and Mass Transfer **18**, 201–206 (1984), 10.1007/BF01007130.

[233] Parker, J. and P. Merati, "An investigation of turbulent taylor-couette flow using laser doppler velocimetry in a refractive index matched facility," Journal of Fluids Engineering-Transactions of the Asme **118**, 810–818 (1996).

[234] Pawlowski, J., "Bestimmung des reibungsgesetzes der nicht-newtonschen flüssigkeiten aus den viskositätsmessungen mit hilfe eines rotationsviskosimeters," Colloid and Polymer Science **130**, 129 (1953), 10.1007/BF01532759.

[235] Pereira, F. and M. Gharib, "Defocusing digital particle image velocimetry and the three-dimensional characterisation of two-phase flows," Measurment Science and Technology **13**, 683–694 (2002).

[236] Pereira, F. and M. Gharib, "Defocusing digital particle image velocimetry and the three-dimensional characterisation of two-phase flows," Measurment Science and Technology **15**, 2029–2038 (2004).

[237] Pereira, F., M. Gharib, D. Dabiri and D. Modarress, "Defocusing digital particle image velocimetry: a 3-component 3-dimensional dpiv measurement technique. application to bubbly flows," Experiment in Fluids **Suppl.**, S78–S84 (2000).

[238] Peters, F., A. Grassmann, H. Schimmel and B. Kley, "Improving small laser light sheets by means of a diffractive optical element," Experiments in Fluids **35**, 4 (2003).

[239] Peurrung, L. M., M. Rashidi and T. J. Kulp, "Measurement of porous medium velocity fields and their volumetric averaging characteristics using particle tracking velocimetry," Chemical Engineering Science **50**, 2243–2253 (1995).

[240] Phan-Thien, N., "Constitutive equation for concentrated suspensions in newtonian liquids," Journal of Rheology **39**, 679–695 (1995).

[241] Phan-Thien, N., X.-J. Fan and B. Khoo, "A new constitutive model for monodispersed suspensions of spheres at high concentrations," Rheologica Acta **38**, 297–304 (1999).

[242] Phan-Thien, N., X.-J. Fan and R. Zheng, "A numerical simulation of suspension flow using a constitutive model based on anisotropic interparticle interactions," Rheologica Acta **39**, 122–130 (2000).

[243] Phillips, R., R. Armstrong and R. Brown, "A constitutive equation for concentrated suspensions that accounts for shear-induced particle migration," Physics of Fluids **4**, 30–40 (1992).

[244] Poslinski, A. J., M. E. Ryan, R. K. Gupta, S. G. Seshadri and F. J. Frechette, "Rheological behavior of filled polymeric systems i. yield stress and shear-thinning effects," Journal of Rheology **32**, 703–735 (1988).

[245] Poslinski, A. J., M. E. Ryan, R. K. Gupta, S. G. Seshadri and F. J. Frechette, "Rheological behavior of filled polymeric systems ii. the effect of a bimodal size distribution of particulates," Journal of Rheology **32**, 751–771 (1988).

[246] Prasad, D. and H. Kytömaa, "Particle stress and viscous compaction during shear of dense suspensions," International Journal of Multiphase Flow **21**, 775–785 (1995).

[247] Prenel, J. P. and M. Jeudy, "A new versatile laser sheet generator for flow visualization," Optics and Laser Technology **30**, 533 (1998).

[248] Probstein, R. F., M. Z. Sengun and T. C. Tseng, "Bimodal model of concentrated suspension viscosity for distributed particle sizes," Journal of Rheology **38**, 811–829 (1994).

[249] Prosperetti, A., "Average stress in a stokes suspension of disks," International Journal of Multiphase Flow **30**, 1–26 (2004).

[250] Pätzold, R., "Die abhängigkeit des fließverhaltens konzentrierter kugelsuspensionen von der strömungsform: Ein vergleich der viskosität in scher- und dehnströmungen," Rheologica Acta **19**, 322–344 (1980).

[251] Quemada, D., "Rheological modelling of complex fluids. i. the concept of effective volume fraction revisited," Eur. Phys. J. AP **1**, 119–127 (1998), 10.1051/epjap:1998125.

[252] Raffel, M., C. Willert, S. T. Wereley and J. Kompenhans, *Particle Image Velocimetry*, Experimental Fluid Mechanics, Springer Berlin Heidelberg, second edition edn. (2007).

[253] Ragouilliaux, A., B. Herzhaft, F. Bertrand and P. Coussot, "Flow instability and shear localization in a drilling mud," Rheologica Acta **46**, 261–271 (2006).

[254] Rashidi, M., L. Peurrung, A. F. B. Tompson and T. J. Kulp, "Experimental analysis of pore-scale flow and transport in porous media," Advances in Water Resources **19**, 163–180 (1996).

[255] Reeks, M. W. and S. McKee, "The dispersive effects of basset history forces on particle motion in a turbulent-flow," Physics of Fluids **27**, 1573–1582 (1984).

[256] Roscoe, R., "The viscosity of suspensions of rigid spheres," British Journal of Applied Physics **3**, 267–269 (1952), Times Cited: 393 0022-3727.

[257] Russel, J., "Studies of thixotropic gelation. part ii. the coagulation of clay suspensions," Proc. R. Soc. London Ser. A **154**, 550–560 (1936).

[258] Rutgers, I. R., "Relative viscosity and concentration," Rheologica Acta **2**, 305–348 (1962).

[259] Rutgers, I. R., "Relative viscosity of suspensions of rigid spheres in newtonian liquids," Rheologica Acta **2**, 202–210 (1962), 10.1007/BF01983952.

[260] Saffman, P. G., "Lift on a small sphere in a slow shear flow," Journal of Fluid Mechanics **22**, 385 (1965).

[261] Saleh, S., J. Thovert and P. Adler, "Flow along porous media by partical image velocimetry," AIChE Journal **39**, 1765–1776 (1993).

[262] Saleh, S., J. F. Thovert and P. M. Adler, "Measurement of two-dimensional velocity fields in porous media by particle image displacement velocimetry," Experiments in Fluids **12**, 210–212 (1992).

[263] Savins, J. G., G. C. Wallick and W. R. Foster, "The differentiation method in rheology .3. couette flow," Society Of Petroleum Engineers Journal **3**, 14–18 (1963).

[264] Schatzmann, M., G. Bezzola, H. E. Minor, E. Windhab and P. Fischer, "Rheometry for large-particulated fluids: analysis of the ball measuring system and comparison to debris flow rheometry," Rheologica Acta **48**, 715–733 (2009), 10.1007/s00397-009-0364-x.

[265] Schlegel, D., "Bestimmung der schubspannungsfunktion des blutes mit dem couette-rheometer unter berücksichtigung des wandverhaltens," Rheologica Acta **19**, 375–380 (1980), 10.1007/BF01543150.

[266] Sengun, M. Z. and R. F. Probstein, "High-shear-limit viscosity and the maximum packing fraction in concentrated monomodal suspensions," Physicochemical Hydrodynamics **11**, 229–241 (1989).

[267] Shapiro, A. and R. Probstein, "Random packings of spheres and fluidity limits of monodisperse and bidisperse suspensions," Physical Review Letters **68**, 1422–1425 (1992).

[268] Shapley, N., *Laser Doppler Velocimetry measurements of particle velocity fluctuations in a concentrated suspension*, Ph.D. thesis, MIT (2000).

[269] Shapley, N., R. Brown and R. Armstrong, "Laser doppler velocimetry measurements of particle velocity fluctuations in a concentrated suspension," Journal of Rheology **46**, 241–272 (2002).

[270] Shapley, N., R. Brown and R. Armstrong, "Evaluation of particle migration models based on laser doppler velocimetry measurements in concentrated suspensions," Journal of Rheology **48**, 255–279 (2004).

[271] Shauly, A., A. Averbakh, A. Nir and R. Semiat, "Slow viscous flows of highly concentrated suspensions–part ii: Particle migration, velocity and concentration profiles in rectangular ducts," International Journal of Multiphase Flow **23**, 613–629 (1997).

[272] Shindo, Y. and K. Kusano, "Densities and refractive indices of aqueous mixtures of alkoxy alcohols," Journal of Chemical and Engineering Data **24**, 106–110 (1979).

[273] Shlien, D. J., "Inexpensive method of generation of a good quality laser light sheet for flow visualization," Experiments in Fluids **5**, 356 (1987).

[274] Simha, R., "Untersuchungen über die viskosität von suspensionen und lösungen 7. Über die viskosität von kugelsuspensionen (suspensionen in poiseuille'scher grundströmung)," Colloid and Polymer Science **76**, 16–19 (1936).

[275] Simha, R., "A treatment of the viscosity of concentrated suspensions," Journal of Applied Physics **23**, 1020–1024 (1952).

[276] Singh, A. and P. Nott, "Experimental measurements of the normal stresses in sheared stokesian suspensions," Journal of Fluid Mechanics **490**, 293–320 (2003).

[277] Sinkankas, J., "Mineralogy," pp. 226–233, D Van Nostrand Company, Princeton (1966).

[278] Sosio, R. and G. B. Crosta, "Rheology of concentrated granular suspensions and possible implications for debris flow modeling," Water Resour. Res. **45** (2009), 10.1029/2008WR006920.

[279] Stephenson, J. L. and W. E. Stewart, "Optical measurements of porosity and fluid motion in packed beds," Chemical Engineering Science **41**, 2161–2170 (1986).

[280] Stickel, J. J. and R. L. Powell, "Fluid mechanics and rheology of dense suspensions," Annual Review of Fluid Mechanics **37**, 129–149 (2005).

[281] Strivens, T. A., "The shear thickening effect in concentrated dispersion systems," Journal of Colloid and Interface Science **57**, 476–487 (1976), 0021-9797 doi: DOI: 10.1016/0021-9797(76)90226-5.

[282] Stöhr, M., K. Roth and B. Jähne, "Measurement of 3d pore-scale flow in index-matched porous media," Experiments in Fluids **35**, 159–166 (2003).

[283] Sveen, J., "An introduction to matpiv," (2004).

[284] Tanaka, M., "Visualization of flow in a cubic packing of spheres," in *Ninth International Topical Meeting on Nuclear Reactor Thermal Hydraulics*, San Fransisco (1999).

[285] Tanner, R. and G. Williams, "Iterative numerical methods for some integral equations arising in rheology," Transactions of the Society of Rheology **14**, 19–38 (1970).

[286] Tasic, A. Z., B. D. Djordjevic, D. K. Grozdanic and N. Radojkovic, "Use of mixing rules in predicting refractive indexes and specific refractivities for some binary liquid mixtures," Journal of Chemical and Engineering Data **37**, 310–313 (1992).

[287] Thomas, D. G., "Transport characteristics of suspension: Viii. a note on the viscosity of newtonian suspensions of uniform spherical particles," Journal of Colloid Science **20**, 267–277 (1965).

[288] Thompson, B. E., "Refractive index matching techniques in complex rocket-engine flow configurations," Tech. rep. (1990).

[289] Thornton, S., "The measurement of the absolute viscosity of anomalous fluids: I: The measurement of the time-dependence of viscosity of thixotropic materials," Proceedings of the Physical Society. Section B **66**, 115–119 (1953).

[290] Timberlake, B. and J. Morris, "Concentration band dynamics in free-surface couette flow of a suspension," Physics of Fluids **14**, 1580–1589 (2002).

[291] Torquato, S., T. M. Truskett and P. G. Debenedetti, "Is random close packing of spheres well defined?" Physical Review Letters **84**, 2064 (2000), Copyright (C) 2008 The American Physical Society Please report any problems to prola@aps.org PRL.

[292] Tropea, C., A. Yarin and J. Foss, *Springer Handbook of Experimental Fluid Mechanics*, Springer (2007).

[293] Tsai, S. C., D. Botts and J. Plouff, "Effects of particle properties on the rheology of concentrated noncolloidal suspensions," Journal of Rheology **36**, 1291–1305 (1992).

[294] Tsai, S. C. and B. Viers, "Effects of liquid polarity on rheology of noncolloidal suspensions," Journal of Rheology **31**, 483–494 (1987).

[295] Tsai, S. C. and K. Zammouri, "Role of interparticular van der waals force in rheology of concentrated suspensions," Journal of Rheology **32**, 737–750 (1988).

[296] Tung, L. H., "Correction," Journal of Polymer Science **19**, 598–598 (1956).

[297] Tung, L. H. and W. C. Taylor, "A rapid method of constructing density gradient tubes," Journal of Polymer Science **17**, 441–442 (1955).

[298] Tung, L. H. and W. C. Taylor, "An improved method of preparing density gradient tubes," Journal of Polymer Science **21**, 144–147 (1956).

[299] Uzol, O. Uzol, Chow, Y. C. Chow, Katz, J. Katz, Meneveau and C. Meneveau, "Unobstructed particle image velocimetry measurements within an axial turbo-pump using liquid and blades with matched refractive indices," Experiments in Fluids **33**, 909–919 (2002).

[300] Van De Hulst, H. C., *Light scattering by small particles*, Wiley, New York (1957).

[301] Vand, V., "Viscosity of solutions and suspensions. i. theory," Journal of Physical Chemistry **52**, 277–299 (1948), 0022-3654.

[302] Varty, R. L., "A new system for index-matched laser-anemometer measurements," Journal of Physics E-Scientific Instruments **17**, 1124–1126 (1984).

[303] Voltz, C., M. Nitschke, L. Heymann and I. Rehberg, "Thixotropy in macroscopic suspensions of spheres," Physical Review E **65** (2002), Times Cited: 7 1 1063-651X.

[304] Wang, D. C. and A. Khalili, "Flow visualization and quantitative measurements inside porous media by particle image velocimetry," Optical Technology and Image Processing for Fluids and Solids Diagnostics 2002 **5058**, 232–239 (2002).

[305] Wang, P., C. Song, C. Briscoe and H. A. Makse, "Particle dynamics and effective temperature of jammed granular matter in a slowly sheared three-dimensional couette cell," Physical Review E (Statistical, Nonlinear, and Soft Matter Physics) **77**, 061309–15 (2008).

[306] Waxler, R., D. Horowitz and A. Feldman, "Optical and physical parameters of plexiglay 55 and lexan," Applied Optics **18**, 101 (1979).

[307] Weeks, E. R., J. C. Crocker, A. C. Levitt, A. Schofield and D. A. Weitz, "Three-dimensional direct imaging of structural relaxation near the colloidal glass transition," Science **287**, 627–631 (2000).

[308] Wiener, O.Leipzig. Ber. **62**, 256 (1910).

[309] Wildman, D. J., J. M. Ekmann, J. R. Kadambi and R. C. Chen, "Study of the flow properties of slurries using the refractive index matching technique ldv," Powder Technology **73**, 211–218 (1992).

[310] Woods, M. E. and I. M. Krieger, "Rheological studies on dispersions of uniform colloidal spheres .1. aqueous dispersions in steady shear flow," Journal of Colloid and Interface Science **34**, 91 (1970).

[311] Yarlagadda, A. and A. Yoganathan, "Experimental studies of model porous media fluid dynamics," Experiments in Fluids **8**, 59–71 (1989).

[312] Yeow, Y., W. Ko and P. Tang, "Solving the inverse problem of couette viscometry by tikhonov regularization," Journal of Rheology **44**, 1335–1351 (2000).

[313] Yianneskis, M. and J. Whitelaw, "Velocity characteristics of pipe and jet flow witch high particle concentrations," Tech. Rep. FS/83/22, Imperial College (1983).

[314] Yuki, K., M. Okurnura, H. Hashizume, S. Toda, N. B. Morley and A. Sagara, "Flow visualization and heat transfer characteristics for sphere-packed pipes," Journal of Thermophysics and Heat Transfer **22**, 632–648 (2008).

[315] Zachos, A., M. Kaiser and W. Merzkirch, "Piv measurements in multiphase flow with nominally high concentration of the solid phase," Experiments in Fluids **20**, 229–231 (1996).

[316] Zarraga, I., D. Hill and D. Leighton, "The characterization of the total stress of concentrated suspensions of noncolloidal spheres in newtonian fluids," Journal of Rheology **44**, 185–221 (2000).

[317] Zerai, B., B. Z. Saylor, J. R. Kadambi, M. J. Oliver, A. R. Mazaheri, G. Ahmadi, G. S. Bromhal and D. H. Smith, "Flow characterization through a network cell using particle image velocimetry," Transport in Porous Media **60**, 159–181 (2005).

[318] Zhang, D. and A. Prosperetti, "Averaged equations for inviscid disperse two-phase flow," Journal of Fluid Mechanics **267**, 185–219 (1994).

[319] Zhang, D. and A. Prosperetti, "Momentum and energy equations for disperse two-phase flows and their closure for dilute suspensions," International Journal of Multiphase Flow **23**, 425–453 (1997).

[320] Zisselmar, R. and O. Molerus, "Investigation of solid-liquid pipe flow with regard to turbulence modification," The Chemical Engineering Journal **18**, 233–239 (1979).

[321] Zou, R. P., J. Q. Xu, C. L. Feng, A. B. Yu, S. Johnston and N. Standish, "Packing of multi-sized mixtures of wet coarse spheres," Powder Technology **130**, 77–83 (2003).

Curriculum Vitae

Sébastien Wiederseiner
Prabé 2
3963 Crans-Montana
Email: sebastien.wiederseiner@a3.epfl.ch

Birthday: 28/03/1981

Education

04/2005–01/2010   PhD thesis
Experimental rheophysics of concentrated particle suspensions in a Couette cell
Environnemental Hydraulics laboratory
Ecole Polytechnique Fédérale de Lausanne

10/2004–03/2005   Master of Science in Mechanical Engineering
Master thesis:
Modeling of the interstitial fluid in a granular flow (DEM-CFD coupling)
Ecole Polytechnique Fédérale de Lausanne

10/2000–09/2004   EPF engineer studies in mechanical engineering
Ecole Polytechnique Fédérale de Lausanne

08/1996–07/2000   High school degree type C (scientific)
Lycée-Collège des Creusets, Sion

miscellaneous

10/2008   Member of the stearing board of the *Swiss Group of Rheology*

04/2005   Rhyming price of the Ecole Polytechnique Fédérale de Lausanne
Award a work providing an original contribution to get better understanding
in fluid mechanics